DEVELOPMENT OF AN INJECTOR TEST RIG FOR SHEAR THINNING GEL PROPELLANTS

Thabang Mdhluli

Submitted in fulfilment of the academic requirements for the degree of Master of Science in Mechanical Engineering, College of Agriculture, Engineering and Science, University of KwaZulu-Natal.

Durban, South Africa

30 May 2024

Supervisor: Prof. Michael J. Brooks

Co-Supervisor: Mr. Timothy Velthuysen

DECLARATION 1- PLAGIARISM

I, Thabang Mdhluli, declare that:

1. The research reported in this dissertation/thesis, except where otherwise indicated, is my original work.
2. This dissertation has not been submitted for any degree or examination at any other university.
3. This dissertation does not contain other persons' data, pictures, graphs or other information, unless specifically acknowledged as being sourced from other persons.
4. This dissertation does not contain other persons" writing, unless specifically acknowledged as being sourced from other researchers. Where other written sources have been quoted, then:
    a. Their words have been re-written but the general information attributed to them has been referenced;
    b. Where their exact words have been used, their writing has been placed inside quotation marks, and referenced.
5. This dissertation does not contain text, graphics or tables copied and pasted from the Internet, unless specifically acknowledged, and the source being detailed in the dissertation/thesis and in the References sections.

Signed: ……  …… Date: 30 MAY 2024

Mr Thabang Mdhluli

As the candidate's supervisor, I agree to the submission of this thesis.

Signed: …… Date: ……

Prof Michael J. Brooks

As the candidate's co-supervisor I agree to the submission of this thesis.

Signed: …… Date: ……

Mr Timothy Velthuysen

ACKNOWLEDGEMENTS

First and foremost, I would like to thank my supervisors, Prof. Michael Brooks, and Mr. Timothy Velthuysen, for their mentorship, guidance, and support. Their knowledge and insightful feedback have played an important role in producing this research. I would like to acknowledge members of the Aerospace Systems Research Institute (ASRI), whose advice and insightful discussions broadened my perspective during various stages of this research.

I would like to express my deepest and most heartfelt appreciation to my family for their love, encouragement, and support throughout this journey. Their constant check-ups and patience has been my motivation during times when the end seemed too far.

I would like to thank the Department of Higher Education and Training (NESP) for their sponsorship.

In conclusion, the completion of this dissertation would not have been possible without the support and contribution from the Department of Science and Innovation (DSI), the National Research Foundation (NRF), the South African National Space Agency (SANSA), the Aerospace Systems Research Institute (ASRI), and the individuals mentioned above, and for that, I am truly grateful.

ABSTRACT

This work describes the development of an injector test rig to characterise the behavior of shear-thinning gelled rocket propellants. The work falls under a broader program of research into gel propellants conducted by the Aerospace Systems Research Institute (ASRI).

Gels represent a new class of propellant for rocket propulsion applications. They offer potential advantages over conventional liquid and solid propellants but their behaviour through injector orifices is poorly understood. Consequently, there is no standardised design procedure for gelled propellant injectors, although computational fluid dynamic (CFD) methods have shown potential. The aim of this research was to design, build and commission an injector test rig utilising single-element impinging injectors to generate experimental data on gel sprays such as breakup length, and droplet size. The rig is intended to inform gel injector design methodologies by providing experimental data against which CFD-generated simulations can be compared and refined. MATLAB® image processing tools were used to analyse spray sheet images and quantify the resulting fluid structures generated by the test rig.

The study included the design and manufacture of the propellant/simulant feed system, injector insert, injector manifold, frame and propellant/simulant supply tank. Two adjustable converging injection orifices were used to form spray sheets at 45°, 60° and 90° impinging angles. For testing purposes, two water-based simulants were formulated using hydrocolloid xanthan and guar gum gelling agents at 0.5, 1.0 and 1.5 wt%. Rheological characterisation of the gels was performed to verify their shear-thinning behavior using a rotational rheometer. Spray sheets were then generated at injector pressure drops in the range of 140 kPa to 1400 kPa. A MATLAB® model of the system was developed to establish control parameters for the desired outputs and the rig was controlled via a LabVIEW™ application. The rig provides a platform for further research into the behavior of gelled rocket propellants, with an intended focus on hydroxylamine nitrate (HAN) and ammonium dinitramide (ADN).

TABLE OF CONTENTS

LIST OF FIGURES

LIST OF TABLES

NOMENCLATURE

Symbols

Symbol	Description	Unit
A	Area	m^2
C	Factor	-
d	Diameter	m
E	Joint efficiency	-
e	Roughness	mm
F	Force	N
f	Friction factor	-
g	Grip length	m
$gx.x$	Guar gum simulant concentration	-
h	Minor head losses	m
k	Stiffness	N/m
K	Consistency	-
L	Length	m
$\dot{m}$	Mass flow rate	kg/s
n	Power index	-
Oh	Ohnesorge number	-
P	Pressure	Pa
r	Radius	m
r	Length to orifice ratio	-
Re	Reynolds number	-
S	Maximum allowable stress	Pa
t	Thickness	m
T	Torque	Nm
U	Fluid velocity	m/s
v	Velocity	m/s
we	Weber number	-
x	Input	-
$xx.x$	Xanthan gum simulant concentration	-
y	Output	-

Greek

Symbol	Description	Unit
$\dot{\gamma}$	Shear rate	1/s

Δ	Difference	-
ε	Roughness	mm
η	Apparent viscosity	Pa·s
η_∞	High shear rate viscosity	Pa·s
η_0	Zero shear rate viscosity	Pa·s
θ	Impinging angle	^{o}
μ	Dynamic viscosity	Pa·s
ρ	Density	kg/m^3
σ	Hoop stress	Pa
τ_0	Zero shear stress	Pa
τ	Shear stress	Pa

Subscripts

Symbol	**Description**
b	Bolt
c	Clamp
d	Diameter
e	External
f	Flexible hose
gen	Generalized
h	Hardline
i	Initial
inj	Injector
lig	Ligament
o	Orifice
P	Proof
PL	Power law
t	Threaded

Abbreviations

Acronym	**Description**
ADN	Ammonium Dinitramide
ASME	American Society of Mechanical Engineers
ASRI	Aerospace Systems Research Institute
BPVC	Boiler Pressure Vessel Code
CFD	Computational Fluid Dynamics

DAQ	Data Acquisition
DCV	Directional Control Valve
DSI	Department of Science and Innovation
EDM	Electric Discharge Machining
GP	Gel Propellants
HAN	Hydroxylammonium Nitrate
HB	Herschel Bulkley
HBE	Herschel Bulkley Extended
IM	Insensitive Munition
MAWP	Maximum Allowable Working Pressure
MS	Microsoft
NI	National Instruments
NRF	National Research Foundation
PCD	Pitch Circle Diameter
RAM	Random Access Memory
SANSA	South African National Space Agency
SPI	Single Phase Incompressible
UKZN	University of KwaZulu Natal
VI	Virtual Instrument

1. INTRODUCTION

1.1 Aerospace Systems Research Institute

The Aerospace Systems Research Institute (ASRI) of the University of KwaZulu Natal (UKZN) embarked on research of gelled and high-viscosity propellants in 2020. Part of this research involves investigating gel propellants' rheological properties and atomisation. It is intended that the research activities will lead to a Computational Fluid Dynamics (CFD) based design approach for rocket injectors utilising gel propellants (GP).

1.2 Gel Propellants

There has been increasing interest in recent decades on the application of GP in rocket and ramjet propulsion systems. GP are fuels, oxidisers, or monopropellants that are rheologically altered with the addition of gelling agents. They are typically non-Newtonian fluids with shear-thinning properties that are characterised by the power law. The gel behaves like a solid at rest but can be atomised and combusted like conventional liquid fuels once flowing under significant shear stress, with resulting advantages in aerospace propulsion systems, as described in Chapter 2.

1.3 Research Aims

The design of rocket injectors is of particular consideration for propulsion systems utilising GP. Injector design is a crucial factor in the overall performance of the propulsion systems based on gel propellants; in particular, the droplet size created from the injection process is directly correlated to the combustion efficiency. The application of computational methods to injector design for liquid propellant rocket engines is an emerging field of research with many potential advantages, including droplet identification and distribution. Historically, empirical design methods were employed, which over the years have provided expansive experimental data for use in CFD software making computational injector design for liquid propellant engines a common approach. The experimental database and tools for GP injectors are limited, however. The rise in CFD-based design shows potential as a tool for GP injectors, but these computational methods require more comprehensive experimental validation before they can be successfully adopted in GP injector design.

This research addresses the requirement for more rigorous validation of computational results through the application of experimental data as part of basing design decisions on CFD tools. In an effort to meet this requirement, ASRI identified a need for a test rig to study injection and impingement characteristics of GP through a single element injector allowing for droplet characterisation and qualitative analysis. This research is intended to provide useful quantitative (droplet size) and qualitative (web dispersion, ligament thickness, breakup patterns) data to facilitate injector design using CFD tools. The investigations will provide experimental data and form part of the broader research on gel propellants being conducted at ASRI.

1.4 Research Objectives

The primary objective is to develop a test rig to visualise the spray generated by the injector element for image processing to obtain useful data to facilitate optimum injector design utilising GPs. The secondary objective of this research is to study the injection and impingement characteristics of gelled simulants through a single element injector that allows for droplet characterisation and qualitative analysis.

1.5 Dissertation Outline

This dissertation describes the design, construction, and testing of an injector test rig for shear-thinning gel propellants. The test rig is configured to enable the visualisation of the spray sheet generated by two like-on-like injection elements. Chapter 2 describes the literature on gelled propellants and the existing literature that has been conducted to characterise their behaviour and the spray sheets they generate using impinging atomisers.

Chapter 3 focuses on outlining the design of the test rig. Specifically, the single-element atomiser, gel simulant pressurisation chamber, injector frame, and storage tank designs are discussed. In addition, Chapter 3 contains concept designs of the atomiser and storage tank.

Chapter 4 describes the mathematical and MATLAB® Simulink® models developed to simulate the test rig system. The system head losses and driving force of the piston in the pressurisation chamber can be predicted to quantify the injection pressure range for specific settings.

The pressure relief valve setting output obtained from system modelling in Chapter 4 provided a starting point to conduct tests. The test setup and instruments used to collect data are described in Chapter 5 along with test operations and procedures. The control system and LabVIEW™ application are described. An explanation of the application's state machine code is also given.

Chapter 6 gives gel simulant formulations using two gelling agents, followed by rheological characterisation on a rotational rheometer. The simulants formulated and characterised are essential for testing the test rig operations using a gel.

In Chapter 7, the spray sheets of simulants are described including the features and spray structures observed using high-speed image acquisition.

Chapter 8 summarises the research objectives, recaps key findings from Chapter 7, and offers recommendations for future improvements to the test rig.

2. LITERATURE REVIEW

This section introduces gel propellants and provides a summary of previous research conducted on the topic.

2.1 Background of Gelled Propellants

A gel is a soft substance that holds both solid and liquid characteristics. This behaviour is facilitated by a gelling agent combined with a base propellant (Rahimi and Natan, 2000). Gelled propellants are fluids whose rheological properties have been altered by a gellant so that at rest they behave like solids, and flow like conventional liquids when under shear stress (Padwal, et al., 2021). Although gels can be defined variously, their most significant feature is the shear dependent non-Newtonian flow behaviour (Ciezki, et al., 2002). The research and development on different aspects of gelled propellants have been continuously expanding worldwide. GP have a considerable study history, namely in formulation, flow, atomisation, and combustion (Arnold, et al., 2011). Many specialisation areas under these broad categories have emerged as shown in Figure 2-1. The first research conducted on gelled propellants dates from the 1930s and different gel fuels were patented after that (Calabro, 2011). In 1933 the Russian GRID program recorded the first vehicle flight using this invention. They used gelled gasoline on a metal mesh support combusted with liquid oxygen to produce 500 N of thrust (Calabro, 2011) . Another example is a patent by Claude Long (1962) about gelled propellants reinforced with structural material to be used in a rocket in a manner analogous to solid fuels. Rapial and Daney (1969) reported early experimental studies of gelled liquid hydrogen. Which was developed to improve storage capability and reduce vaporisation rate.

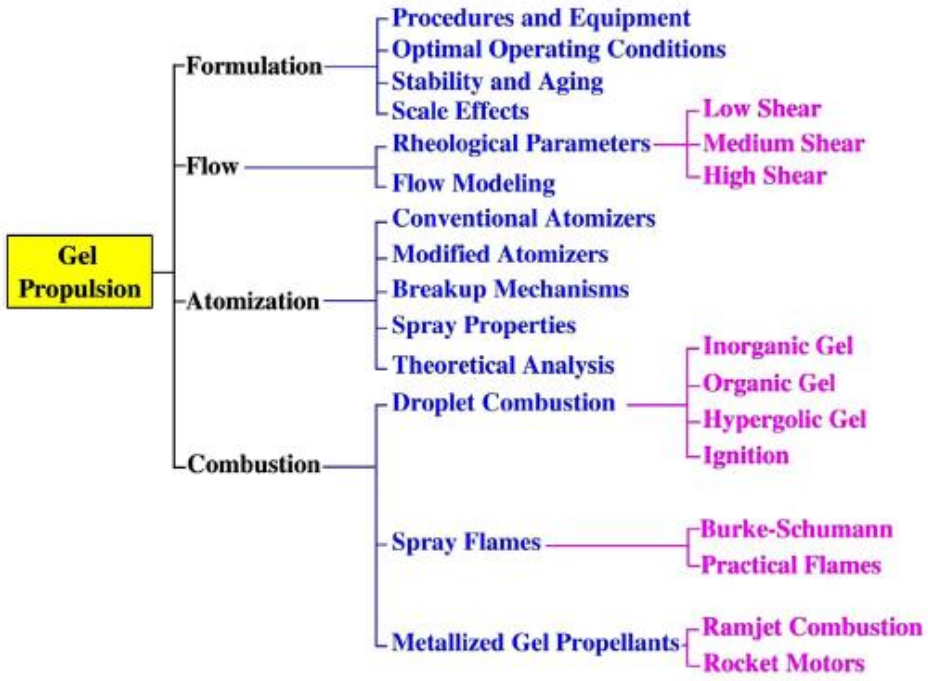

Figure 2-1:An Overview of research and development areas in the field of gel propulsion (Padwal, et al., 2021).

In the mid 1980s, attempts were made to gel hypergolic fuels, but there were scale-up issues and the scale-up process increased the gelation time. In the late 1980s research on gelled propellants was conducted at NASA Lewis Research Center. At this point, gelled propellant research was still in its infancy and without the requisite literature that was to be produced in the years to come, research focus tapered off into other, higher-priority areas. However, GP were already identified as alternative fuels that met safety requirements and possessed performance advantages (Douglas and Robert, 1988). Thompson Ramo Wooldridge Inc (TRW) demonstrated this when conducting the first test firing of a missile using gelled propellants (Hodge, et al., 1999). In the late 1990s and early 2000s the primary focus was on flow, atomisation, and combustion (Rahimi and Natan, 1998). Varghese et al. (1995) examined gelled kerosene fuels with metal additives under shear stresses and different temperatures. They characterised these fuels as thermally stable and pseudoplastic with flow characteristics described by the power law. Chojnacki and Feikema (1994) investigated the atomisation of water-based gels using a like-on-like impinging injector transformed from a capillary viscometer to measure the viscosity of the injected gel. All three areas provided the first insight into issues associated with GPs, such as high feed pressures to liquidise the gel before the injector. The rheology of gel propellant was identified to play a significant role in flow through pipes and injectors and atomisation. Shai and Nathan (1998) reported that the atomisation of GP is affected by the gellant content. They stated that the droplet size during the atomisation increases with increasing gellant content due to increased shear viscosity.

In 2000 the German Aerospace Center (DLR) and Technion-Israel worked together to explore and research further the atomisation (formation of breakup sheets, ligaments, threads, and droplet size) of

GP. From their collaboration, they understood the breakup regimes based on the gel's rheology, the impingement jet velocity, Reynolds, and Weber numbers (Ciezki, et al., 2002). The Reynolds number and Weber number are important parameters that describe the fluid dynamics and atomisation processes. These parameters are commonly used with liquids, but they can be applied to gels that have liquid components. The Reynolds number is used to predict transitions between laminar flow and turbulent flow. Being able to identify the different flow regimes is important for understanding how the gel will break up into smaller droplets. The Weber number is used to predict the dominant break up mechanisms namely surface tension forces or inertial forces.

Technion-Israel proposed the idea of hypergolic ignition of gelled kerosene containing reactive metal particles with hydrogen peroxide. These propellants are environmentally friendly and hypergolic ignition is achieved because the gelation of kerosene allows for the suspension of metal particles (Natan, et al., 2010). Germany's efforts in gel propellant development have appeared in several overviews and summaries mainly focused on gel fuelled ramjet engines and throttleable missiles (Ciezki, et al., 2017). Their investigations showed that a gelled fuel engine using gelled kerosene with boron metal particles dramatically exceeds that of a solid rocket motor with aluminium particles (Haddad, et al., 2012). In 2008, studies on gels of hypergolic fuels and oxidisers have been reported by multiple universities in the United States (Dennis, et al., 2011). In recent years the German Aerospace Center started conducting research on novel fuels and propellants for hydrazine replacements (Ciezki, et al., 2019). These activities stimulated investigations of the formulation of GP, atomisation of impinging jets utilising GP, and characterisation and combustion of GP.

2.2 Gel Propellants

Gels are derived from a base fluid and a gelling agent, the addition of which alters the properties of the base such that it behaves as a shear-dependent non-Newtonian, viscoelastic fluid. In rocket propulsion, gelling agents are added to fuels and oxidisers, and the conduction of a gelation process changes the structural representation to a solid skeleton entrapping the liquid phase. Figure 2-2 shows an example of this structure for Thixatrol ST and Jet A-1 (Padwal, et al., 2021). The base liquid (Jet A-1) is trapped between the molecules of the gelling agent (Thixatrol ST). The physical form of a gelled propellant is a soft amorphous solid with some degree of elasticity (Glushkov, et al., 2022). The gelling agent holds the solid together, forming a three-dimensional matrix of their long polymeric chains to create a network structure entrapping the liquid within the network. Metal additives can be added and remain suspended in the liquid phase.

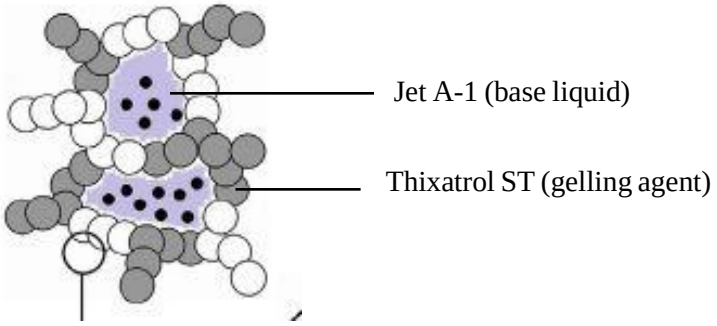

Figure 2-2: Structural representation of gelled Jet A-1 with Thixatrol ST (Arnold, et al., 2009).

In general, a gelled propellant consists of at least the original propellant (fuel or oxidiser) and the added gelling agent. Nanoparticles of metals can also be added to increase the energy density (Arnold, et al., 2011). The addition of gelling agents controls the rheological characteristics of the gel depending on concentrations of the liquid/gelling agent combination. The most significant feature of gelling agents is a fast viscous thickening and elastic build-up to the base liquid, making the formulated propellant difficult to atomise. After gelation, gelled propellants are non-Newtonian fluids which behave like solids at rest with no shear stress applied (Arnold, et al., 2009). When a shear stress is applied to the fluid, the viscosity is lowered and the gel liquifies. This rheological phenomenon is referred to as shear thinning, and the fluid is classified as shear thinning or pseudoplastic (Arnold, et al., 2009). Figure 2-3 shows the behaviour evolution in terms of shear stress (τ) and viscosity as a function of shear rate ($\dot{\gamma}$).

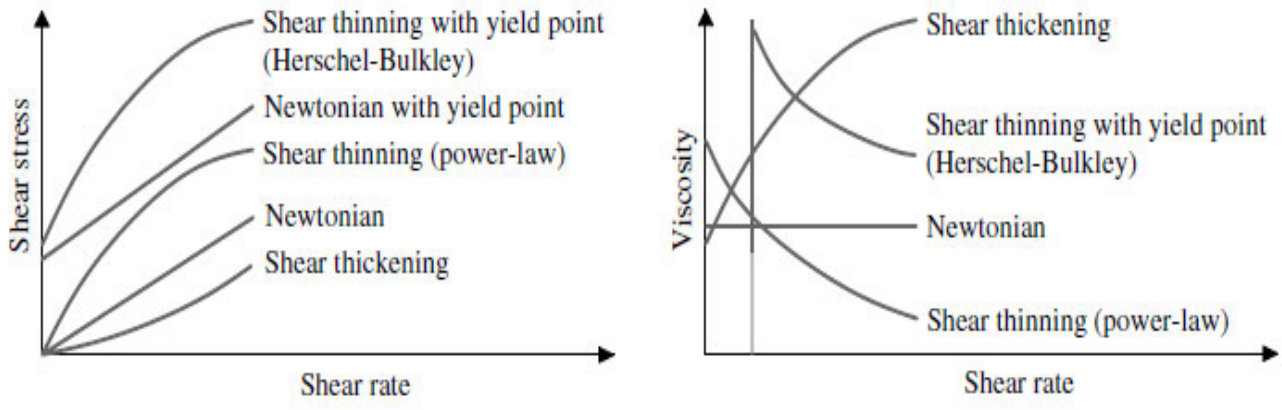

Figure 2-3: Shear stress and Viscosity behaviour of Newtonian and non-Newtonian fluids (Arnold, et al., 2011).

The mathematical expression of shear rate is given by Equation (2-1) where $\dot{\gamma}$ is the shear rate, Δv is the velocity difference between two parallel layers of fluid and Δx is the separation distance between the layers. The relationship between shear rate and shear stress is often described by the power law.

Equation (2-2) demonstrates how shear stress relates to shear rate. In the equation τ is the shear stress, K is the consistency coefficient, and n is the flow behaviour index.

$$\dot{\gamma} = \frac{\Delta v}{\Delta x} \tag{2-1}$$

$$\tau = K(\dot{\gamma})^n \tag{2-2}$$

2.3 The Advantages and Challenges of Gelled Propellants

Gel propellants are advantageous over conventional liquid and solid propellants because of safety and performance benefits (Arnold, et al., 2011). Figure 2-4 shows the benefits of using gel propellants in aerospace propulsion. Many gel propellants have performance characteristics and operational capabilities like liquids, with higher specific and density impulses. Gels also provide solid storage behaviour and safety. Due to increased viscosity, they dampen sloshing in propellant tanks because of the increased frequency at which sloshing occurs (Arnold, et al., 2011). GPs also allow adding metallic particles and permit particle suspension with little sedimentation. Due to the viscoelastic nature of GPs, they are immune to leakages and spillage in storage, loading, and transportation. In addition, some gelled propellants have been shown to meet new propulsion requirements, such as thrust control, re-ignitability, and insensitive munition (IM) (Rahimi and Natan, 2000). The desirable characteristics of gel propellants make them attractive in aerospace applications, especially in volume-limited propulsion systems or environments where sloshing is a concern.

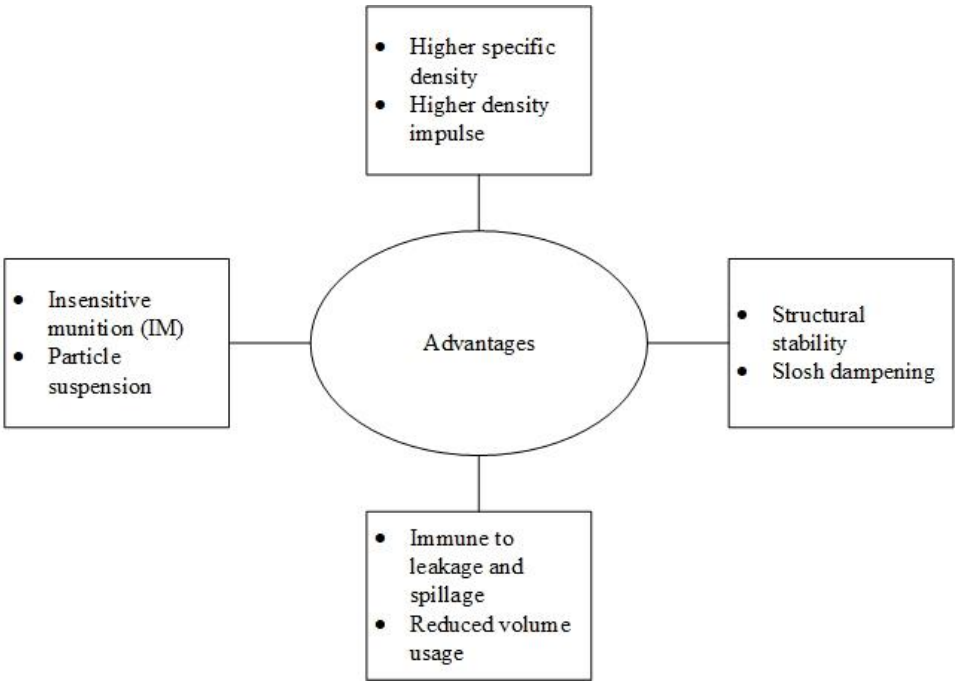

Figure 2-4: Advantages of using gel propellants in aerospace propulsion.

Even though gels offer advantages compared to neat-liquid and solid propellants, the non-Newtonian behaviour requires special treatment and skilful usage. Their increase in viscosity strongly influences the flow, injection, and atomisation, which introduces challenges (Rahimi, et al., 2001). Figure 2-5 shows the difficulties encountered when using gel propellants. Gels possess exceptional stability, giving them good storage and handling attributes, but too much stability also poses a challenge for atomisation (Padwal, et al., 2021). Such gels are too viscous, and the pressure drops required in the feed system are high compared to neat liquids for similar mass flow rates. Another challenge is the atomisation quality. Because of viscous resistance, there is a delayed breakup during the formation of droplets from ligaments. This issue is complicated and influenced by multiple rheological properties and the type of gelling agent used (organic or inorganic). Consequently, larger droplet sizes result and injector clogging can become a challenge. The rheological character of gels imposes possible stagnation regions in the injector that change the mass flow rate of propellant through the injector, causing atomisation issues (Rahimi, et al., 2001).

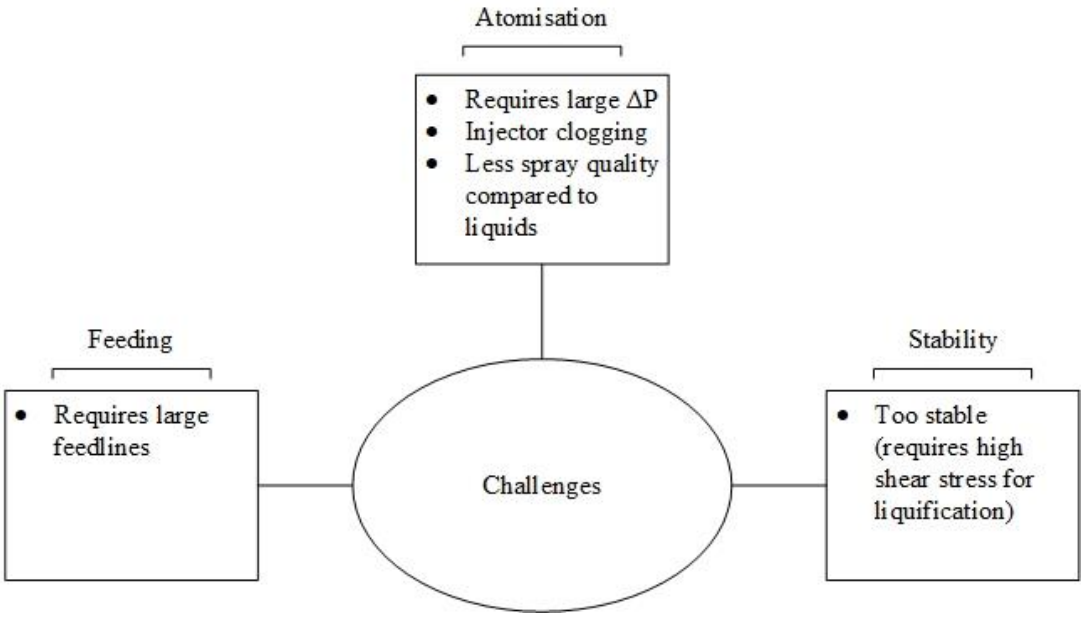

Figure 2-5: Challenges of using gel propellants in aerospace propulsion.

2.4 Gelling Agents

Gelling agents are gel-forming compounds. When dissolved in a liquid, a homogenous mixture forms consisting of microscopically dispersed insoluble particles that are suspended throughout the liquid (Kar, et al., 2019). Most gelling agents are commercial off-the-shelf products and can be classified as organic (polymeric) or inorganic. Synthetically manufactured polymers of acrylic acid are also commonly used. A gel propellant or water-based simulant is formulated by mixing the heterogenous

phase of the gelling agent and the liquid phase at room or elevated temperatures. In semi-solid form, the formulated mixture can contain a gelling agent at concentrations of 0.5% to 10% by mass (Padwal, et al., 2021). Mixing the two components (gelling agent and liquid) to form a homogenous mixture is accomplished with a mechanical mixer or other devices (for example, acoustic mixing). During mixing, the gelling agent forms a stable solid structure (3D intermolecular network) with the molecules of the gelling agent enclosing the liquid phase. The gelling agent and liquid phase molecular interactions impart non-Newtonian flow behaviour to the product (Padwal and Mishra, 2016). The gelling agent also influences the liquid's diffusion characteristics. The diffusion rate depends on the viscosity, which subsequently depends on the gelling agent concentration. Specific gelling agents are reversible and can go from liquid to gel state, a property that adds to their desirability in aerospace applications.

Inorganic gelling agents are hydrophilic substances that use precipitates of inorganic salts to promote solidification. They form semi-solid materials in an organic solvent, making them good candidates for gelling hydrocarbon fuels. Silica (SiO_2) is commonly used to gel hydrocarbon fuels but is inert and does not burn during combustion (Arnold, et al., 2011). The use of silica arises from the relatively low concentration of gelling agent required to form the 3D network entrapping the liquid phase. Hydrophilic groups in the particle surface of silica promote hydrogen bonding between themselves. Due to its hydrophilic behaviour, gels with hydrophobic (non-hydrogen bonding) solvents form at low concentrations (by weight) because the interaction between silica particles and the solvent is weak. With hydrophilic solvents such as acids (potential oxidisers), alcohols (potential fuels), and water (potential simulant), higher concentrations of silica are required because there is an interaction between the particles themselves and the solvent.

Organic gelling agents are hydrocolloid substances, many of which are polymeric (Rahimi, et al., 2001). Agents such as Carbopol, cellulose compounds, and xanthan are dry powders that hydrate when mixed in water. These polymers are primarily used to prepare water-based gels that can replace hazardous propellants for laboratory testing in propulsion applications (Natan and Rahimi, 2002). Polymer gelling agents form cross-linked hydrogen bonds when dispersed in hydrophilic solvents (Baek and Kim, 2011). The formulated mixtures exhibit shear thinning behaviour (Padwal, et al., 2021) but the molecular bonding with water resists liquid breakup, resulting in poor atomisation (Mallory, et al., 2010). Although these gels present challenges with atomisation, agar as a gelling agent can be used in place of polymeric gelling agents, because agar absorbs water and forms a network around the hydrophilic solvent rather than bonding with it. Mallory and Sojka (2010) reported that a gelling agent-liquid interaction is essential for properly selecting a gelling agent type. They also reported that a gelling agent must be selected against a criterion and have desirable characteristics such as effective gelation with low concentrations, and it should be safe, non-corrosive, and economical.

Organogels are another type of gelling agent. These are non-polymeric, consisting of low molecular weight, and only gel with organic liquids (Terech and Weiss, 1997). Organogels have the same gelling agent-solvent molecular network as polymeric gelling agents. They also impart non-Newtonian and shear-thinning behaviour to the base liquid. Organogels are much easier to atomise than gels formulated using polymeric gelling agents, but the gel propellants formulated with non-polymeric organic gelling agents require warming in the organic solvent to initiate molecular interaction (Terech and Weiss, 1997). Ciezki et al. (2002) used a castor oil derivative Thixatrol ST as a non-polymeric organic gelling agent to formulate Jet A-1 gels. Other castor oil derivatives have been used, such as MPA 60, Thixcin R, and Thixatrol R (Padwal, et al., 2021).

2.5 Gel Simulants

A water-based gel simulant is used whenever the actual gelled propellant is not necessary (e.g. in research and development). Water is used as a comparison fluid and can be used to simulate many liquid propellants. Water and water-gel simulants are expected to simulate the time-independent rheological properties of the actual propellant accurately (Dennis, et al., 2011). Water is used as a constant viscosity comparison fluid because it is easy to handle, safe, and economical.

The process of ensuring similarity of the water-gel simulant and the actual gelled propellant is essential to study the fundamental characteristics of gelled propellant atomisation and is termed rheological matching. Rahmi and Natan (1998) used water with specific gelling agents rheologically matched with hydrocarbon fuels to investigate how gelling agent concentrations and injector geometry affect atomisation. Green et al. (1991) presented a paper on flow visualization through a triplet coaxial injector using a water-gel simulant composed of water, sodium hydroxide, and an acrylic acid polymer resin as gelling agents. Chojnacji and Feikma (1994) used water gels to investigate the atomisation and non-Newtonian liquid sheets formed by like-doublet injectors. Rahimi et al. (2000) studied the shear rheology of gel propellants using water-based simulants rheologically matched to gelled hydrocarbon fuels using various gelling agents such as HPC, HEC, silica, and Carbopol.

2.6 Gel Formulation

The procedures followed to make gel propellants from a base liquid by adding a gelling agent can be straight forward. For example, Tarpley (1969) formulated gels of volatile hydrazine by filling a vessel with hydrazine and slowly adding 3% colloidal silica with agitation. Agitation of the gelling agent and base liquid is always required to achieve a homogenous mixture (Padwal, et al., 2021). Mechanical or ultrasonic mixing techniques are used to ensure the mixture is homogenous. Padwal and Mishra (2013) prepared Jet A-1 gel fuel samples in a vessel equipped with three-blade impellers. They reported that the mixing was done at 1900-2000 rpm for 15-20 minutes. Santos et al. (2010) described the rheological behaviour of gelled JP-8 and RP-1 fuels and the optimum mixing process when gelled with fumed silica. They used an acoustic mixing technique instead of a conventional approach after they found problems

with blade or impeller mixing due to the gel's stiffness. Acoustic mixing is a technique that uses oscillating acoustic waves in the mixture to create micro-scale turbulence in the medium, which gives consistent mixing for viscous or even solid materials (Santos, et al., 2010).

2.7 Rheology

Rheology is the study of a fluid's deformation and flow properties under static and dynamic forces. Gels are non-Newtonian fluids that behave like solids under zero shear force and flow like liquids under a shear force. The flow characteristics are dependent on the rheological properties. These flow characteristics also affect the atomisation characteristics of gels. A gel must show shear-thinning behaviour and have significant yield stress to provide atomisation characteristics. Such gels are categorized as shear-thinning fluids with a yield point (pseudo plastic). For a Newtonian fluid, the shear viscosity (η) is independent of the shear rate ($\dot{\gamma}$) and is represented by a constant. It is defined by the ratio of the shear stress to shear rate expressed in equation (2-3). In this equation, η is the shear viscosity, τ is the shear stress, and $\dot{\gamma}$ is the shear rate.

$$\eta = \frac{\tau}{\dot{\gamma}} \tag{2-3}$$

Conversely, for a non-Newtonian fluid, the shear viscosity depends on the shear rate. The power law (Ostwald-de-Waele model) can describe the two fluid types (Newtonian and non-Newtonian) given by Equation (2-4). Equation (2-6) describes a Newtonian fluid for an n value equal to one ($n = 1$). For non-Newtonian fluids, the power law index is between zero and one ($0 < n < 1$)

$$\eta = K\dot{\gamma}^{n-1} \tag{2-4}$$

Gels envisaged for application in rocket propulsion systems must show significant yield stress (Padwal, et al., 2021). This is why they must be rheologically characterised for developing gelled propellant propulsion systems. Rahimi et al. (2001) reported that the generalized Herchel-Bulkely (HB) model described by equation (2-5) is the most adequate for gel studies and characterisation. This model expresses the shear stress as a function of the shear rate with a parameter for the yield stress. The expression describes the viscous behaviour of non-linear gels with a yield point.

$$\tau = \tau_{yield} + K\dot{\gamma}^{n} \tag{2-5}$$

The HB model applies to gel fluids with low and medium shear rates. In the model, n defines the degree of non-Newtonian behaviour, and K defines consistency. Fluids with a higher K value are thicker and more viscous. The flow index (n) is useful in that it can be used to determine how the fluid behaves. A flow index between zero and one indicates that the fluid shows pseudoplastic or shear-thinning behaviour. If n =1, the fluid is Newtonian and a value of n greater than 1 shows shear-thickening behaviour. For high shear rates an extended version of the HB model exists that considers the minimal viscosity given by Equation(2-6).

$$\eta = \eta_0 + K\dot{\gamma}^n + \eta_\infty \quad (2\text{-}6)$$

Rahimi et al. (2001) reported that the extended HB model predicts the viscosities more accurately than the HB model because typical rocket injection shear rates are above 10^5 s^{-1}. Baran et al. (2022) reported that to accurately determine the flow behaviour, a new Reynolds number should be defined as non-Newtonian fluids behave differently under different shear conditions. They suggested that the Reynolds number be modified to include the fluid's rheological properties *K* and *n*. The generalised power law Reynolds number is therefore derived from the conventional Reynolds number and calculated as:

$$Re_{gen,PL} = \frac{\rho u^{2-n} d^n}{K((0.75 + 1/4n)^n \times 8^{n-1}} \quad (2\text{-}7)$$

Where $Re_{gen,PL}$ does not account for the yield stress and is only valid for fluids described by the power law.

2.8 Rheological Characterisation

Rheological characterisation is important for developing gelled propellants and identifying a fluid's limitations and behaviours.

2.8.1 Thixotropy

Thixotropy is a time-dependent rheological phenomenon. It is characterised by a substance's ability to decrease in apparent viscosity under a constant applied shear stress, followed by its ability to recover when the applied stress is removed. When a gel is pumped through pipelines, thixotropy provides the possibility to liquefy the gel. In aerospace applications, this rheological property allows gelled fuels and oxidisers to be controllable during injection and atomisation. The thixotropic property of a gel depends on concentration, type of gelling agent, and the addition of particles. Rahimi et al. (2007) identified two main aspects of thixotropy in gels: (1) the thixotropic effect in comparison to the shear thinning effect and (2) the reversibility of the material (its effect to its viscosity when the shear stress is removed). They also showed that the thixotropic effect in inorganic gelling agents is insignificant. Figure 2-6 shows a quantitative evaluation by Nathan and Rahimi (2000). The graph shows thixotropy loops of gel propellant simulants, and as they predicted in their study, shear stress increases with shear rates and increasing gelling agent concentration. The apparent viscosity, also a ratio between shear stress and shear rate, decreases with increasing shear rate and time.

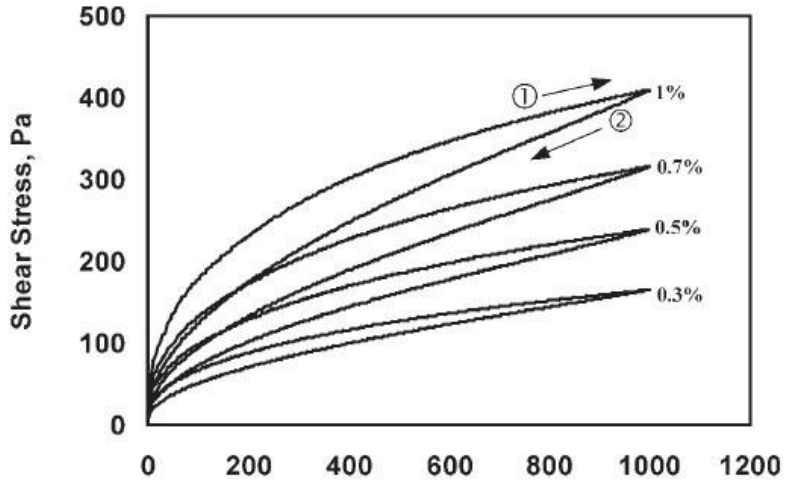

Figure 2-6: Thixotropic loops of water-based simulants at various gelling agent content (Natan and Rahimi, 2000)

2.8.2 Yield stress

The yield stress parameter provides an estimation of the stability of gelled propellants. In aerospace applications, a stable phase is required to store gelled propellants and to enable slosh damping. Another characteristic derived from the yield stress parameter is whether any leakage occurs in storage or feed line systems. In the context of gelled propellants, the yield stress is an indicator of the initial pressure gradient required to initiate flow. Nathan et al. (2007) stated that the yield stress affects the spray characteristics, and that measurement and control of this rheological parameter is necessary for propulsion systems utilising gelled propellants. According to Boger (2000) the yield stress can be determined by two methods. The first method is indirect and involves extrapolation by polynomial approximation of the shear stress versus shear rate curve. The second method is by practically measuring the yield stress using rheometric equipment.

Barnes and Walters (1985) argued that the second method of measurement of the yield stress is a detection limit of the equipment used. They also claimed that a non-Newtonian shear thinning fluid's viscosity is finite. The material flows faster under high shear stress and slower under low shear stress. Nathan et al. (2007) performed rheological tests of water-based gel simulants at 20 °C and they found the results to be consistent with the HB model. They also observed that the apparent viscosity decreases monotonically as the shear stress increases outside the sub-yield stress range.

2.8.3 Viscosity

GP encounter different levels of shear during various processes on a test rig. Padwal et al. (2021) surveyed experimental work done by other researchers. They presented the different levels of shear in various processes involving a gel propellant flowing at 30 g/s with a density of 1000 kg/m^{3,} as given in Table 2-1. Figure 2-7 shows the co-variations of shear rate from Table 2-1. The process/locations on the test stand are numbered 1 to 6 in Figure 2-7. The graph shows the characteristic time (t*) versus

shear rate for the different locations. The characteristic time is a measure of the time it takes for the gel to respond to an applied stress. The storage shows the longest phase during which the gel is subjected to the lowest shear stresses. Expulsion from the storage tank follows at a shear rate of the required mass flow rate. Processes 3-6 are much faster, and the shear rates vary from 10^{1}-10^{6} s^{-1}. The graph also shows that viscosity is the primary variable that controls the behaviour of the gel through the processes shown on the test stand on the coordinate plot because if this was not the case, the graph would be a horizontal line indicating the material's viscosity remains unchanged. The graph also indicates that for the gel they used exhibits a crossover behaviour, from the atomiser to droplet vaporisation the characteristic time initially decreases and then increasing. This indicates that the viscosity of the gel increases, and this behaviour can resist atomisation, making it more challenging to break the liquid into fine droplets.

Table 2-1: Characteristics and shear scale of various processes of gel propellants (Padwal, et al., 2021)

	Process	**t***	$\dot{\gamma}$
1	Storage	$>10^{6}$	$<10^{-4}$
2	Expulsion	53	2.4
3	Tube Flow	0.84	4.8×10^{3}
4	Atomizer flow	0.84	4.8×10^{3}
4a	Atomizer tube	0.22	141
4b	Orifice	2.6×10^{-4}	3×10^{5}
5	Droplet transformation	10^{-3}	3×10^{5}
6	Droplet vaporisation and combustion	1	3×10^{5}

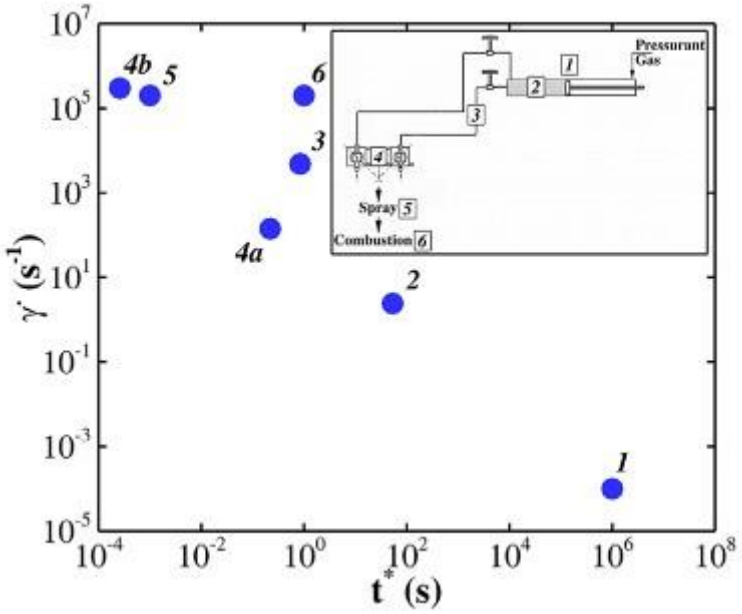

Figure 2-7: Shear rate vs characteristic time of the process in which a gel propellant is involved (Padwal, et al., 2021).

2.9 Injection and Atomisation of Propellant

An injector is one of the main parts of a rocket engine. It is located at the forward end of a combustor and injects propellants into the combustion chamber in the correct ratios and conditions, yielding complete and stable combustion. Generally, the injector is a plate with a pattern of small holes through which fuel and oxidiser travel before making their way into the chamber. The injector also converts fluid streams from the small holes to droplets in the combustion chamber space (Nikvash and Nekoufar, 2015).

The injector has the most significant impact on engine performance. In most applications, it is designed to perform closest to its ideal state (Huzel and Huang, 1992). According to Huzel and Huang (1992) injection systems have efficiencies close to 100%, achievable through uniform distribution and fine atomisation of propellants. Atomisation is another function of the injector which must accelerate vaporisation by breaking up liquid jets into droplets (Ghafourian, et al., 1991). Breaking up liquid jets for fine atomisation is achieved differently for each different injector element type (e.g., non-impinging, unlike impinging, and like-impinging). Liquid sheet breakup (atomisation) occurs when jet streams from element pairs collide at a position called the impingement point not far from the injector plate resulting in small droplet formation. When two identical jet streams of high Reynolds number collide with one another, a fluid sheet forms. Within the fluid sheet, some fluid is directed radially outwards away from the impact point (Bush and Hasha, 2004). The radially directed fluid accumulates at the edges of the fluid sheet to form rims that bound the sheet.

Impinging injectors atomise liquid mass using the impinging momentum of the two jets (Jung, et al., 2006). Dombroski and Hooper (1963) experimentally investigated the breakup mechanism of liquid sheets formed by impinging jets. They found that waves are formed on the liquid sheet by the impact force from the two jet streams and that the growth of these waves determines the atomisation characteristics. They also observed another breakup regime at high injection velocities where the sheet is broken up into periodic strips of liquid. The liquid strips then further disintegrate into droplets. The formation of this regime occurs within a certain range of Reynolds and Weber numbers (Bremond and Villermaux, 2006)

2.9.1 Injection Elements

The injector incorporates a pattern of injection elements on a plate, as shown in Figure 2-8 . The injection elements can be either non-impinging, unlike-impinging, or like-impinging.

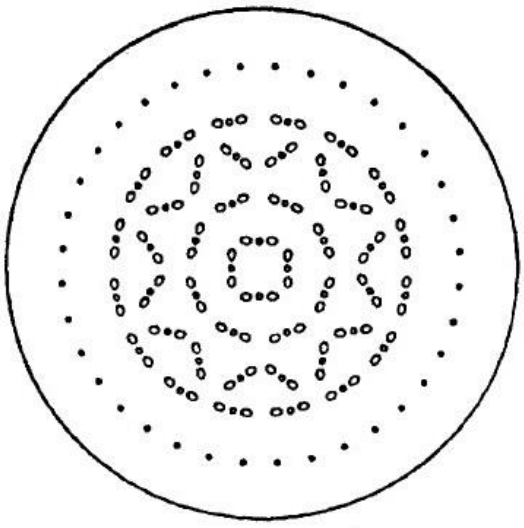

Figure 2-8: Injector element pattern (Huzel and Huang, 1992).

In non-impinging injection elements mixing and atomisation are achieved by the shearing action of a gas. The coaxial injector shown in Figure 2-9 is the most common configuration for this type of element. A coaxial injection element has a slow-moving liquid stream in the center, surrounded by a high-velocity concentric gas. The coaxial injection element is less well-suited for liquids and dense fuels (e.g., gels) (Huzel and Huang, 1992). Song et al. (2021) investigated non-impinging injection elements and argued that coaxial injection elements are unsuited for gels. Another non-impinging injection element is a showerhead, shown in Figure 2-10. This injection type has direct axial non-impinging streams of either liquid or gas flowing through the elements. According to Huzel and Huang (1992) this type of injection element provides little atomisation or mixing. They are commonly used in hybrid propulsion systems to introduce the oxidiser into the combustion chamber.

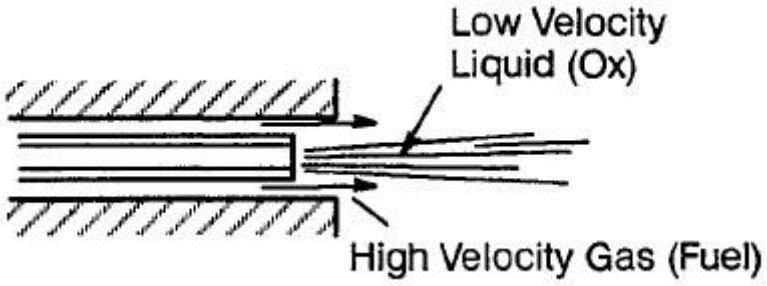

Figure 2-9: Coaxial Injection Element Type (Huzel and Huang, 1992).

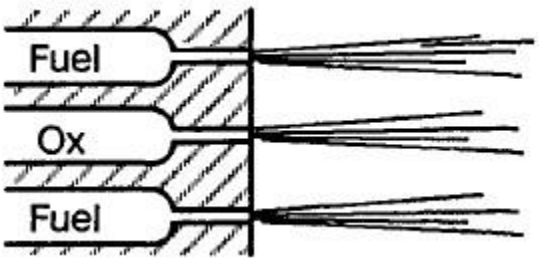

Figure 2-10: Showerhead Injection Element Type (Huzel and Huang, 1992).

Unlike-impinging injection elements are the simplest way of achieving mixing of two different liquids (Fu, et al., 2014). The impact of the two cylindrical coplanar jets produces a thin expanding spray of a mixture of the two impinging fluids, as shown in Figure 2-11 . Atomisation and mixing in this type of injection element is not perfectly distributed, being significantly affected by any momentum or stream diameter mismatch.

Figure 2-11: Unlike-impinging Injection Element Type (Huzel and Huang, 1992).

For like-impinging elements, the impingement is of equal cylindrical coplanar jets. This type of injection element has two like-fluid streams angled towards one another to an impact point. This configuration does not allow mixing since only one fluid exists in each injection element pair. The non-uniform distribution of atomisation with this configuration is only affected by a jet stream diameter mismatch. Like-impinging injection elements are frequently used for liquid/liquid propellant systems.

2.9.2 Injector Orifice Geometry

Plain circular orifice atomisers are used most in impinging injectors and radial jets for pintle injectors (Yoon, et al., 2010). Extensive studies have been performed on the flow of liquid through plain orifices. Earlier studies focused on mean discharge coefficients, and more recent work focused on transient behaviour (Teoman, et al., 2022). These studies showed a strong influence of the surface geometry of the orifice inlet lip to the liquid jet in the orifice bore (Yoon, et al., 2010). Liquid jet unsteadiness has been reported for high Reynolds numbers due to flow separation formed at the inlet of the orifice. Qing-fei et al. (2014) also performed simulations and predicted a few magnitudes of flow pulsations from the orifice because of inlet conditions at the orifice inlet. This suggests that abrupt changes or sharp edges may promote turbulence and pulsations.

Different orifice geometries have been studied by Qing-fei et al. (2014). They conducted experiments to determine the effects of orifice geometry on the flow and breakup of liquid sheets formed by elliptical, circular, and rectangular jets. They noted that the discharge coefficient of elliptical orifices is higher than those of circular and rectangular orifices. However, as the aspect ratio of the orifice rises, the discharge coefficient decreases. Leask and MacDonell (2017) also studied the effects of orifice geometry on spray generated by a like-doublet elements and they found that better mixing was achieved with rectangular orifices, but large droplet sizes were present. They also noted that rectangular orifices were susceptible to mis-impingement. For gel propellant applications, the geometry of the orifice plays an important role in the injector's internal flow because of the non-Newtonian fluid properties of gels (Yoon, et al., 2010). Unlike Newtonian fluids, the viscosity changes when a shear stress is applied to the fluid. Non-Newtonian fluids may slow down the discharge process because of shear-dependent viscosity, yield stress, and other rheological properties (Teoman, et al., 2022). The discharge coefficient of an injector can be defined as a function of the process driving force and the orifice geometry as given in equation (2-8), where C_d is the discharge coefficient, $\dot{m}$ is the mass flow rate, A is the orifice cross sectional area, ρ is the fluid density, and Δp is the pressure differential. Baran et al. (2022) also characterized the discharge of complex fluids through an orifice. They also noted that the discharge is strongly affected by the orifice geometry and fluid properties.

$$C_d = \frac{\dot{m}}{A\left(\sqrt{2\rho\Delta p}\right)} \tag{2-8}$$

Previous research shows that the geometry (diameter and aspect ratios) affects the discharge and pressure loss coefficients. Khahledi et al. (2020) argued otherwise, in their study they showed that the orifice geometry does not have any effect on the discharge coefficient since the effects of geometry are negligible compared to the highly viscous nature of non-Newtonian fluids. High fluid viscosity reduces the discharge rate due to high mechanical energy loss in the laminar regime. Researchers have found that solutions with higher viscosities yielded lower discharge when other geometric constraints were

kept similar. Chowdhury and Fester (2012) observed a similar phenomenon indicating that high viscosity slows down the discharge process. Orifice geometry and fluid properties are both important factors affecting the discharge process. The aspect ratio appears to be the most important parameter among the geometric factors.

2.9.3 Injector Losses

Injector atomisation has been studied extensively in the past decade. Taylor (1999) analytically modelled the shape and liquid sheet produced by impinging jets and compared the results with experimental data. A lack of agreement between the model and experimental data attributed to differences in the various jet orifices related to material, quality of orifice hole, and surface roughness. Because the breakup and atomisation of a liquid sheet largely depend on the laminar or turbulence characteristics of a liquid jet, the internal flow in the orifice is important in determining the spray characteristics of impinging injectors.

Cavitation is an important phenomenon that affects the internal flow in injector orifices (Jung, et al., 2006). A sudden change in flow direction at the entrance of an orifice reduces the static pressure up to the saturation pressure of the working fluid resulting in bubbles forming at this point (orifice entrance). The bubbles at the entrance cause the liquid to separate from the walls of the flow domain and, thus, make the jet characteristics dependent on the flow time. The collapse of cavitation causes energy losses which can result in longer travel time for the fluid. The flow separation causes the mass flow rate to change, which may cause mis-impingement. Jung et al. (2006) investigated internal flows of sharp and round-edge orifices and their effects on sheet breakup lengths. They found that a round-edge orifice entrance has a smooth flow with no disturbances, as shown in Figure 2-12, and a sharp-edge orifice causes the flow to change its direction, so a cavity is formed, as shown in Figure 2-13.

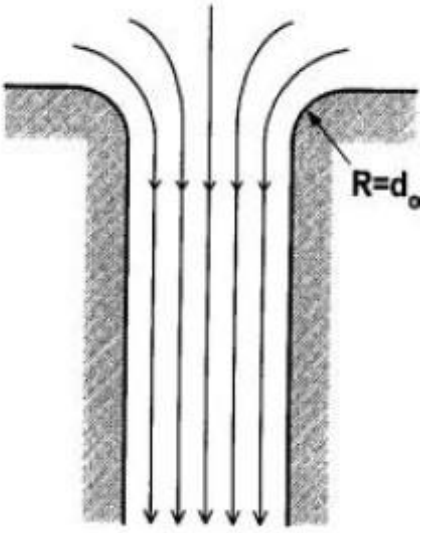

Figure 2-12: Round edge orifice entrance (Jung, et al., 2006)

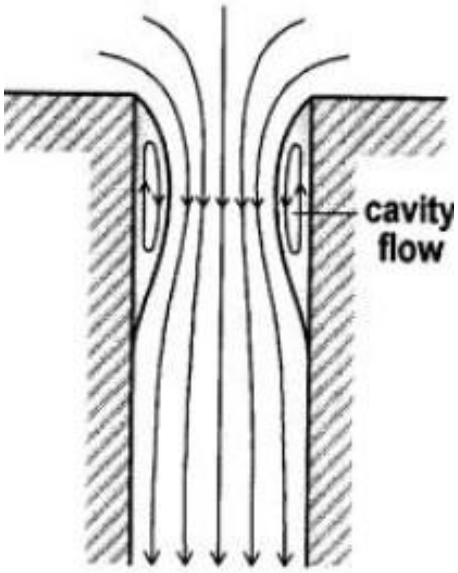

Figure 2-13: Sharp edge orifice entrance (Jung, et al., 2006)

2.10 Gel Propellant Injection

An impinging jet injection configuration is mostly found on liquid propellant systems. Besides being used more frequently in liquid systems, the impinging injection elements can be used to atomise gelled propellants. Multiple researchers have presented studies on the atomisation mechanisms of gel propellants using impinging injection elements. Jens von Kampen et al. (2006) investigated the influence of metal particle addition on the spray characteristics and rheological properties of gelled Jet A-1 using a doublet-like-on-like impinging jet injector. Qing-fei Fu et al. (2014) investigated the effects of injection element orifice geometry on atomisation for gels using impinging jet injectors. They found that square and elliptical orifice geometries under the same injection pressure formed liquid sheets with greater instability than sheets formed by circular jets. However, the discharge coefficients of square and elliptical orifice geometries are smaller and decrease as the aspect ratio increases. Li-Jun Yang et al. (2014) investigated the atomisation of gelled propellants. They performed impinging injector experiments with high-speed camera visualisation to show the liquid sheet breakup process. Gel propellants use impinging jet injectors because they are easy to manufacture and show good atomisation characteristics (Yang, et al., 2012). Non-impinging injection elements can also be used. Hao-Sen Guan (2018) conducted an experimental study of the spray process of gelled ammonium dinitramide (ADN) using a swirl atomizer. According to Hao-Sen Guan (2014), swirl injectors provide effective liquid atomisation methods. Wooseok Song et al. (2021) used a pintle injector to spray gelled propellant and characterise breakup and atomisation performance. They used a multi-slit and multi-hole type pintle injector and argued that the breakup and atomisation performance decreased due to the low injection velocities of pintle injectors. They concluded that pintle injectors are not well suited for gelled propellant atomisation.

2.11 Gel Propellant Atomisation

When a high shear stress is applied to a gel, the shear rate increases and the gel converts to liquid (Rahimi and Natan, 2000). The liquified gel can flow faster. A high-velocity fluid flowing through a small cross-sectional area increases in shear rate (Wooseok, et al., 2021). When this principle is incorporated into injection elements, the gel can be converted into its liquid state by feedlines and the injector. From a fluid mechanics viewpoint, the rheological properties of gels cause them to increase in viscosity, but gels behave as time-dependent non-Newtonian power-law fluids whose viscosity decreases with increasing shear rate. Therefore, the mentioned principle can be applied to gel propellant atomisers.

Like-doublet impinging injection elements are the most popular type used to achieve atomisation for gels (Fu, et al., 2014). In this configuration, a jet stream with circular cross-section issues from the injector. For atomisation, the liquid jet streams expand radially from the point of impact, forming a thin sheet of liquid that breaks into ligaments and tiny droplets. A schematic diagram of a spray sheet generated from like-doublet impinging injection elements is shown in Figure 2-14. In a like doublet injector, two equal size orifices inject two streams of liquid jets that impinge on each other (Notaro, et al., 2019). On impact, a liquid sheet forms bounded by a rim.

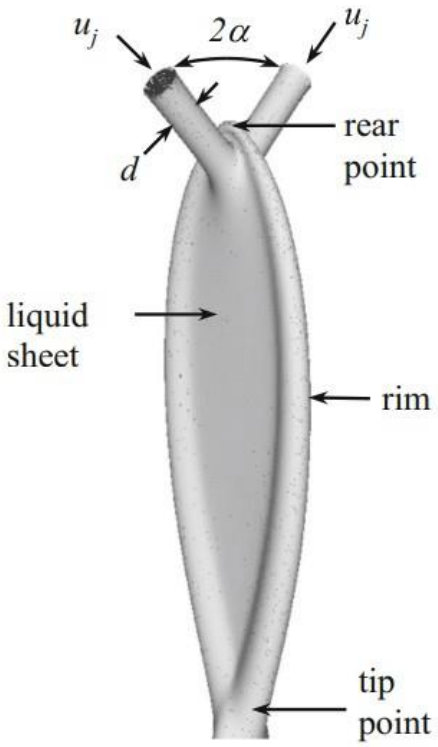

Figure 2-14: Like-doublet liquid sheet (Notaro, et al., 2019).

When like-doublet injection jet streams impinge on one another, an attenuating spray sheet is formed perpendicular to the coplane containing the jet axis from the injection elements, as shown in Figure 2-15. Figure 2-16 shows the typical atomisation patterns for non-Newtonian fluids. Three patterns are shown. Figure 2-16a shows a closed rim pattern which is usually observed at low Reynolds numbers. As the Reynolds number increases, the rim opens as shown in Figure 2-16b. As it increases further, the rim opens, and the sheet increases in width and breaks into ligaments, as shown in Figure 2-16c. These ligaments go on to disintegrate into smaller ligaments and droplets downstream. As the jet velocity increases, the aerodynamic wave from the impact dominates the breakup process. The aerodynamic wave breaks the rim. This breakup results in bow-shaped ligaments forming periodically and further disintegrating into droplets as shown in Figure 2-17.

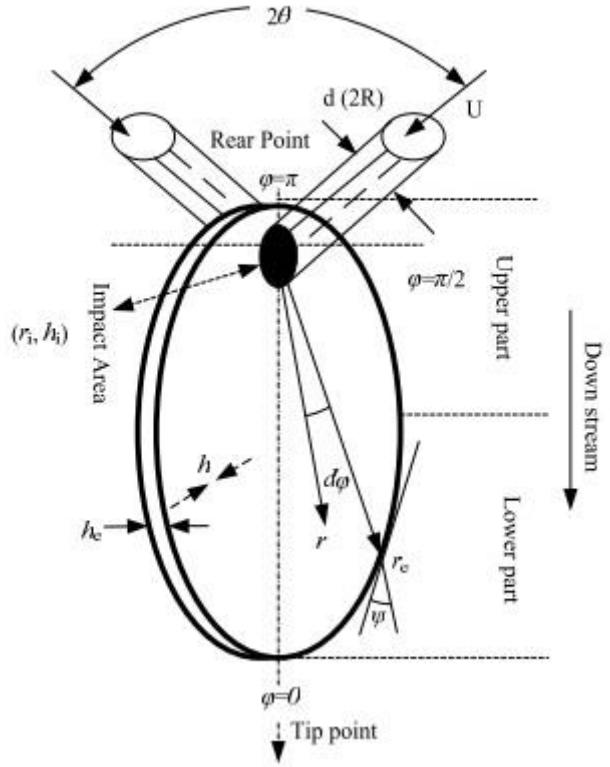

Figure 2-15: Spray sheet from doublet impinging injector (Bremond and Villermaux, 2006)

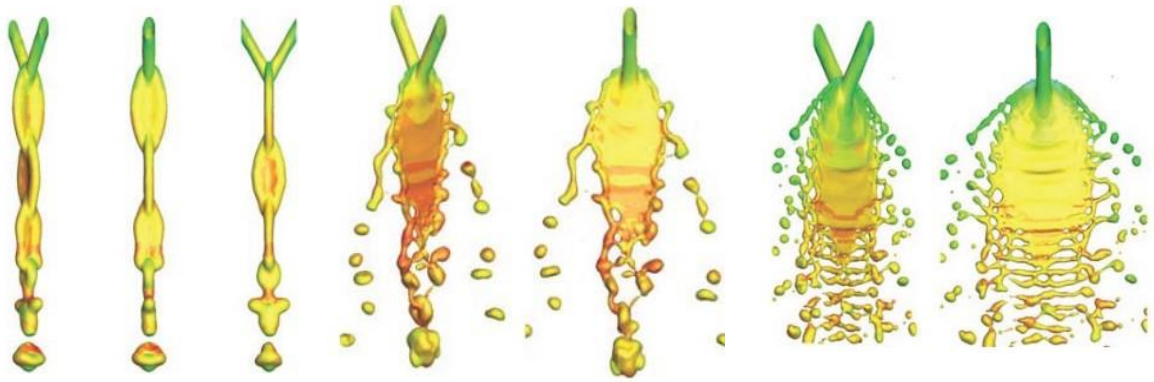

(a) (b) (c)

Figure 2-16:Atomisation patterns for non-Newtonian fluids (Bremond and Villermaux, 2006)

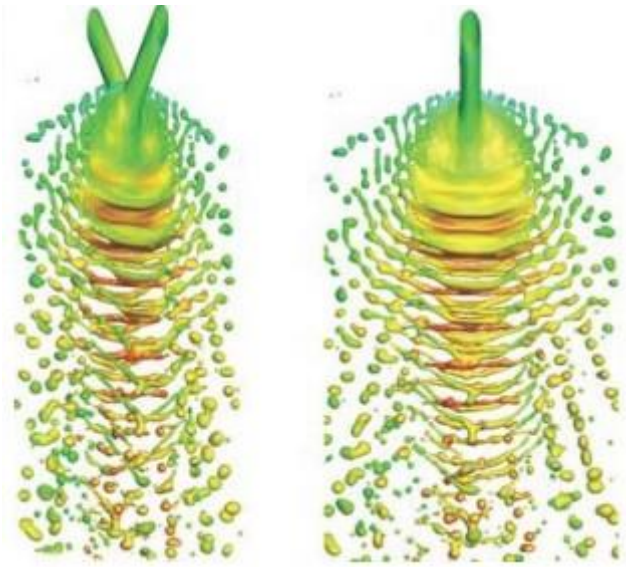

Figure 2-17: Aerodynamic wave effect on sheet breakup (Bremond and Villermaux, 2006)

Rahimi and Natan (1998) experimentally investigated the atomisation of gelled propellant using an air-blast triplet atomiser. They found that viscoelastic water gels exhibit the same spray patterns as Newtonian liquids. They also concluded that increasing gelling agent concentration increases the Sauter mean diameter (SMD). Ma et al. (2011) investigated the breakup characteristics of non-Newtonian liquids using numerical simulation to simulate the primary atomisation from impinging jets. They alluded that viscous and surface tension effects dominate the breakup.

2.12 Sheet Breakup

Many experiments have been conducted on liquid sheet breakup to improve understanding of the breakup phenomena. The quality of atomisation is dictated by the breakup of liquid sheets and is

indicated by the size and distribution of droplets (Priyesh and Tiegang, 2014). The general finding of liquid sheet breakup into droplets is that the drop size increases with an increase in the working fluid's viscosity and surface tension. The breakup of liquid sheets can be broken down into regimes, which Reitz and Bracco (1982) studied by considering fluid-dynamic instabilities. They reviewed work done by other researchers and reported that the unbroken length of a jet issuing from an injector is a function of its velocity. A jet's breakup length initially increases as the jet's velocity increases, but then reaches a maximum point and decreases. In the low jet velocity range, the droplets that break up from the jet are comparable to the jet orifice size. This feature occurs in the first two regimes, namely the Rayleigh and first wind-induced regimes. At higher velocities, the breakup length decreases or remains constant (Rietz and Bracco, 1982) and the jet surface is disrupted before the breakup of the liquid core. The disruption starts at the jet surface and eventually moves to the core. This type of disruption occurs in the second wind-induced and atomisation regimes. In the second wind-induced regime, the surface liquid break-up length is not necessarily zero but occurs at a finite length when the surface liquid and core liquid break into droplets smaller than the orifice size. In the atomisation regime, the surface liquid length is zero, and the jet surface breaks up immediately at the orifice exit. Figure 2-18 shows the demarcation of the breakup regimes. The regimes are defined by dimensionless numbers Reynolds (Re), Weber (We), and Ohnesorge (Oh).

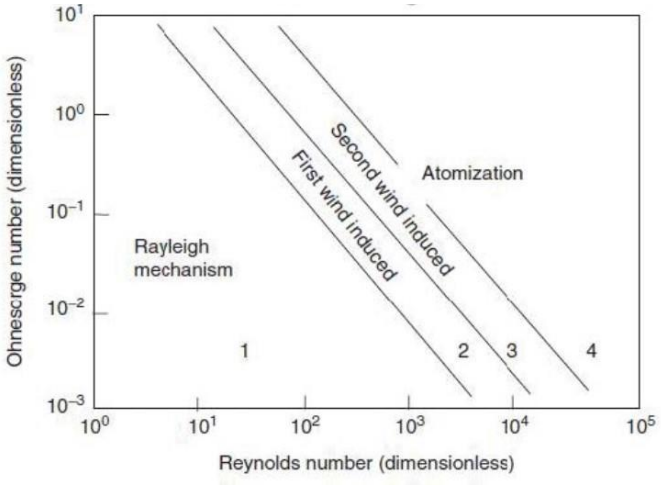

Figure 2-18: Breakup Regime Boundaries (Rietz and Bracco, 1982)

The regimes are shown by straight lines plotted on a natural log scale of Oh versus Re. Oh is a function of nozzle diameter and fluid physical properties.

$$Re = \frac{\rho U d}{\mu} \tag{2-9}$$

$$We = \frac{\rho U^2 d}{\sigma} \tag{2-10}$$

$$Oh = \frac{\sqrt{We}}{Re} = \frac{\mu}{\sqrt{\rho \sigma d}} \tag{2-11}$$

Here, ρ is the density, U is the fluid velocity, d is the diameter, and μ is the dynamic viscosity. For impinging injectors, sheet destabilization leads to droplet formation caused by instabilities. The sheet obtained from the impinging jets is bounded by a cylindrical rim that suffers from a capillary instability of the Rayleigh type (Kull, 1991). This causes the boundary to disintegrate, and the sheet breaks up into strips of the liquid called ligaments and further into droplets, as shown in Figure 2-19. How the liquid sheet disintegrates depends on the operating conditions, but the cause of the disintegration is instability between the sheet and its surroundings, whereby growing impact waves are imposed on the sheet (Dombroski and Johns, 1963).

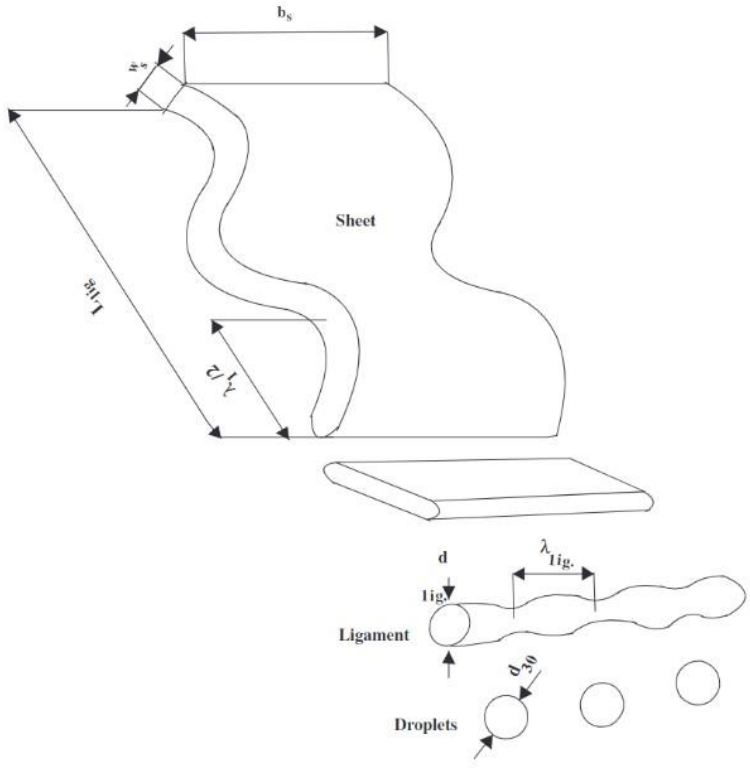

Figure 2-19:Schematic of liquid sheet breakup (Negeed, et al., 2011).

Figure 2-19 also shows the successive stages of the liquid sheet breaking up into droplets. The wavy liquid sheet obtained from two impinging jets is considered uniform in thickness w_s. The growing surface impact wave detaches liquid strips at the leading edge of the sheet with each strip subsequently contracting into a ligament of diameter, d_{lig}. The ligament then goes through another instability called capillary pinching, where it disintegrates into droplets of diameter d_{30} (Negeed, et al., 2011).

2.13 High-Speed Visualization and Image Processing

The most utilised investigative technique to observe the liquid sheet break up from impinging injectors as described above, is with short time interval image acquisition (Wahono, et al., 2007). High-speed instantaneous images provide information on quantities such as breakup length, spray angle, droplet size, and drop distribution. For example, Qing-Fei et al. (2015) investigated the spray formed by swirl injectors at elevated pressures, and the sprays were recorded using a high-speed camera. They could extract parameters of the spray characteristic such as spray cone angle, length of the liquid sheet, and breakup length. Park et al. (2004) studied the liquid sheet breakup and used photographic images to quantify the spatial growth rate of surface instabilities on a liquid sheet.

Several parameters can be measured from photographic images by image processing. Suslov et al. (2019) performed studies on the injection and combustion of injectors using high-speed optical diagnostics to visualise the spray and flame. They also presented a shadowgraph image analysis for characterising the liquid jet from the injector. Lozano et al. (2001) performed experiments on liquid sheet breakup of planar liquids and used image processing to get binary images to determine the spatial growth rate of the liquid sheet instability.

The spray sheet breakup of gel propellants is a critical aspect on engine performance. Precision in spray sheet breakup promotes effective atomisation and mixing. Achieving fine atomisation leads to the formation of small droplets increasing the surface area of propellant available for combustion and this enhances combustion efficiency. Well mixed propellants lead to uniform combustion, thus reducing the likelihood of incomplete combustion and combustion instability. Capturing the breakup involves using visualisation techniques to record and analyse the processes. This requires the use of a high-speed camera to capture the primary and secondary breakup mechanisms of a liquid sheet as it emerges from the impinging point and disintegrating into ligaments and droplets. By visualising the breakup, intricate details can be captured, gaining valuable insights into the atomisation process and optimizing injector performance. The information gathered in this literature review was used to inform the approach taken for capturing various spray sheet breakup events of impinging injectors so that important features and data could be captured to support the design process of injectors through the application of CFD tools.

3. TEST RIG DESIGN

This Chapter describes the design of the injector test rig and its components, including the gel simulant delivery chamber, injection element, and injection element manifold.

3.1 Introduction

The shear-thinning gel propellant injector test stand is a laboratory-scale modular stand for studying the liquid sheet breakup of non-Newtonian fluids. The stand was designed for single-element injection of gelled monopropellants. The stand is modular, comprising several subsystems that can be replaced or configured differently.

To study the range of spray sheet breakup characteristic described in the previous chapter, the test stand had to offer the ability to change parameters such as impinging angle, the distance between the orifices, and impingement length. Importantly, the test stand was required to deliver the propellant/simulant to the injector elements using a system that allowed different injection pressures. In addition, high fidelity image acquisition of the liquid spray sheet was a necessity.

A render of the test stand assembly shown in Figure 3-1 and includes a table frame, tank frame, tank, propellant/simulant pressurisation chamber, a hydraulic actuator, and an injector assembly frame. The table frame houses all other subsystems of the stand. The injector frame that is bolted to the front side of the table frame and houses the injector manifold bracket, injector manifold, and rotation guide backplate, allowing for different impingement angle and orifice distance settings. A storage tank feeds propellant/simulant into the pressurisation chamber prior to testing.

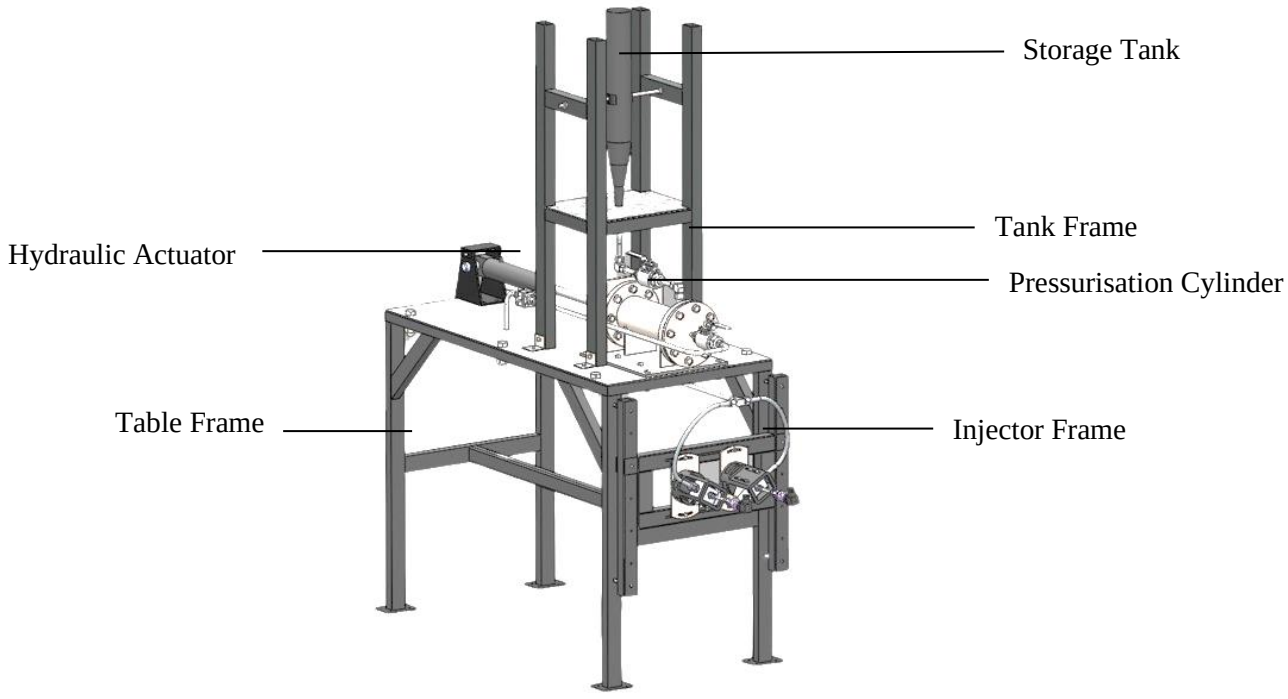

Figure 3-1: Test stand assembly.

3.2 Single-element Atomiser Jet Design

The purpose of the injector elements is to introduce the liquid stream of simulants to the impinging point, to meter the flow of simulants at a predetermined rate, and to allow for different parameters of the injector to be investigated. The injector element was designed without considering a rocket engine's performance and stability, which are determined to a large degree by the design of the injector. The design is typical for injectors having a length-to-orifice diameter ratio of ten and a circular orifice geometry.

3.2.1 Inject Element Manifold

The manifold makes use of rectangular aluminium stock with an injector element insert port machined on the tapering end. The taper was incorporated so that the impinging point could still be in field of view of the camera at high impinging angles. It also has a simulant inlet, and pressure transmitter port machined to independently record injection pressure of each orifice during testing. It was decided to use a brass bolt as an injector insert. These inserts can be machined with different orifice sizes and geometries in order to test the effects of these parameters on propellant atomisation and spray characteristics. Figure 3-2 shows a cross-sectional view of the manifold.

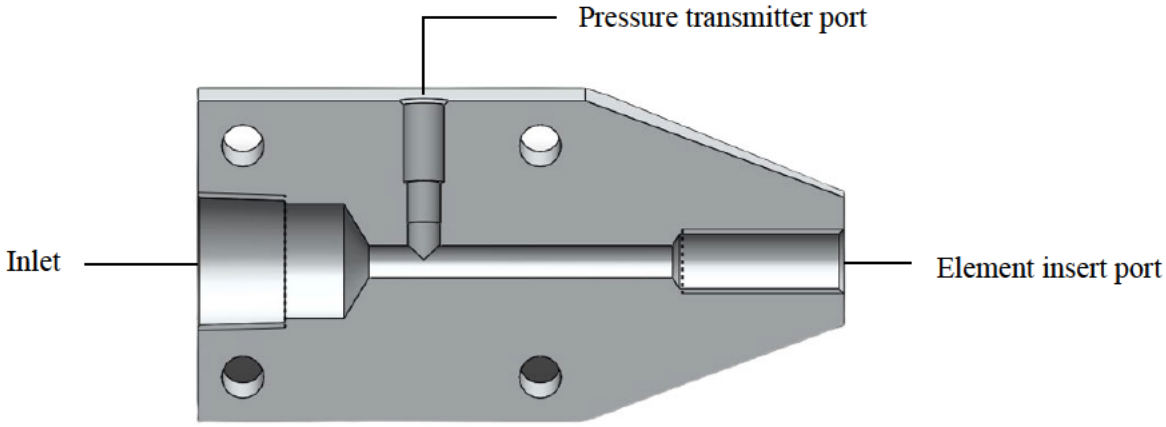

Figure 3-2: Concept 2 cross-sectional view.

3.2.2 Injector Element Insert

The injector element insert was manufactured from a standard M10 x 1.5 brass bolt. The bolt material was selected because of the soft aluminium material of the manifold. Wire electrical discharge machining (EDM) was used to machine the orifice geometry into the bolt so that the bore is free of burrs and other surface imperfections caused by drilling. An injector bore length of 10 mm and an orifice diameter of 1 mm was selected for this injector element resulting in an L/D (aspect ratio) of 10. It is recommended that injector element L/D ratios be equal to or greater than five for the fluid flow to

reattach to the flow domain after the orifice inlet and to avoid clogging the flow domain from propellant impurities (Fu, et al., 2014). The ratio recommendation also helps alleviate the effects of jet distortion caused by the vena contracta phenomenon. Figure 3-3 shows the injector element insert cross-sectional view with the orifice machined into the bolt. The bolt has a 5 mm bore before contracting to the orifice inlet. A rounded inlet produces a higher C_d value and subsequently lowers the pressure drop.

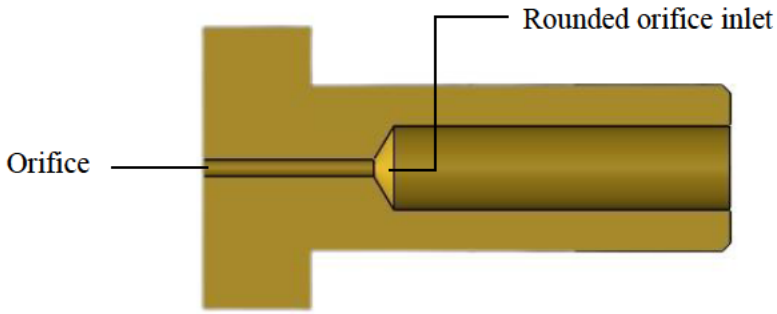

Figure 3-3: Injector element insert cross-sectional view.

3.3 Gel Simulant Delivery Chamber

The simulant delivery chamber was designed to operate like a piston pump. A reciprocating rod from a hydraulic actuator moves back and forth inside the cylinder. The piston is attached to the rod and has O-rings on its circumference for sealing between itself and the chamber walls. The chamber was constructed from a cast iron cylinder, along with two slip-on flanges welded on each end of the cylinder. The fore slip-on flange on the cylinder was used to attach a blind flange with a half-inch tube at the centre to feed the simulant from the chamber into the manifold. The aft slip-on flange was used to bolt the chamber assembly onto a saddle back plate bolted onto the top plate on the test stand frame. Figure 3-4 shows the cross-sectional view of the chamber, and Figure 3-5 shows an isometric view of the assembly.

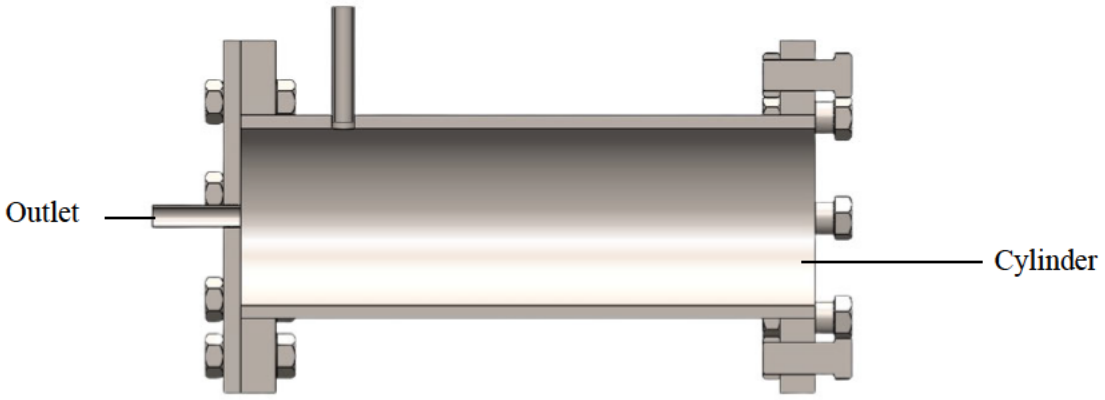

Figure 3-4: Gel delivery chamber cross-sectional view.

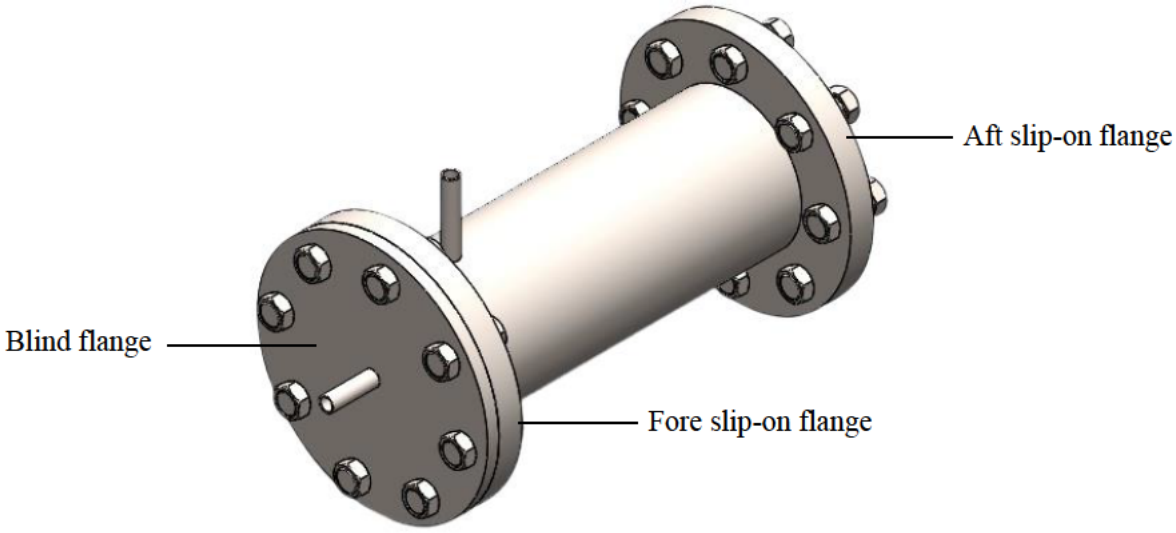

Figure 3-5: Gel delivery chamber isometric view.

3.4 Injector Frame

The purpose of the frame is to attach the injector element manifolds and backplate assembly. The frame is then bolted onto the test stand frame using brackets on the element frame. The element frame allows for changes in parameters such as impinging angle, the distance between orifices, and the impinging point. The frame's top and bottom steel tubes have slot cut-outs that allow the backplates to traverse left and right. Two 3D-printed manifold brackets are bolted on the backplates. Figure 3-6 shows a rendering of the injector element frame subsystem.

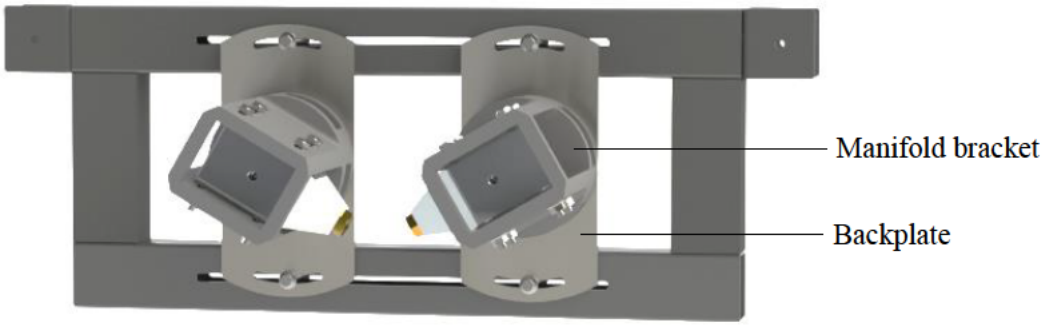

Figure 3-6: Rendering of the injector frame subsystem.

The frame has brackets on each side, which were used to bolt the frame onto the front of the test stand table frame. The test stand table frame has equally positioned holes drilled into the front vertical legs, and these holes were used to move the entire injector frame up and down. The up and down adjustments of the element frame were used to position the spray sheet generated by the injector elements in the camera's field of view.

3.4.1 Backplate

The backplate was designed to set the impinging angle (2θ). The backplate has holes drilled into the plate around the centre hole at angles of $0°$, $30°$, $60°$ and $90°$. There are radial slot cut-outs on the plate for other angle settings if required in which case the holes can be used as a reference. Figure 3-7 shows a frontal view of the backplate.

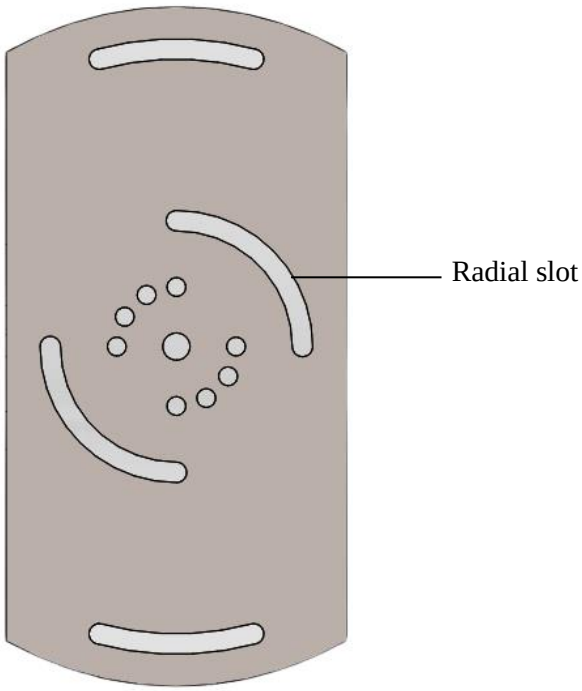

Figure 3-7: Backplate.

The backplate has an 8 mm diameter centre hole used to mount the manifold bracket to the backplate. It is also the point of rotation for the manifold bracket to set the impinging angle. The backplate was fabricated from 5 mm thick mild steel.

3.4.2 Manifold Bracket

The function of the manifold bracket is to adjust the manifold position on the slot cut-outs so that the two jets from the injection elements are in the same plane. Two concepts for this bracket were generated.

Concept 1-Manifold Bracket

This concept used 5 mm thick mild steel plates that were laser cut and bent to form the bracket for the injector element manifold. Figure 3-8 shows an isometric view of this design concept. The bottom plate of this design has a series of four 90-degree bends that form a “u” shape with extensions. The extended surfaces have straight slot features 6 mm in width. These slots are used to attach the bracket onto the backplate radial slots. The attachment allows for the bracket to rotate on the backplate to set the impinging angle. Additional 5 mm width straight slots features were added on the vertical sides of the “u” shape. These slots were used to bolt the side plates of the manifold bracket to create the manifold enclosure. The side plates also have straight slots cut on them. These slots were used to position the manifolds such that they reside in the same plane. A 3D-printed cap was fitted on the two side plates to keep them parallel and allow the injector element manifold to move within the enclosure.

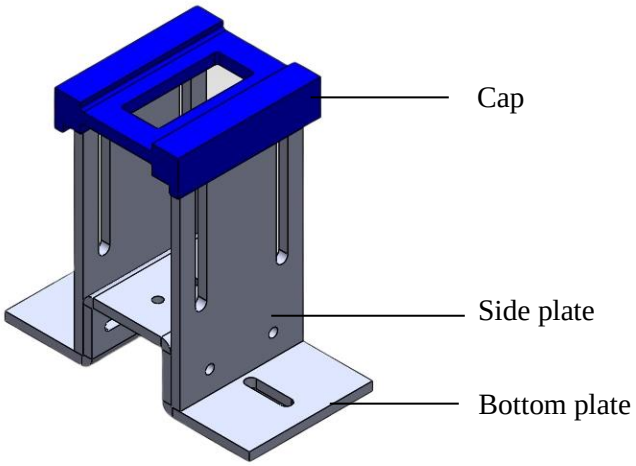

Figure 3-8: Concept 1- manifold bracket.

Concept 2-Manifold Bracket

While sharing the same functionality as concept 1, this version is one 3D-printed component, as illustrated in Figure 3-9. This concept was bulkier than the first concept but did not require assembly Both concepts have an opening at the top for attaching a pressure transmitter on the manifold. This concept has a 100 mm diameter base and an 8.5 mm centre hole. The centre hole was used to bolt the bracket onto the backplate using an M8 bolt. Two 6 mm diameter hole features were added on the base at a PCD of 35 mm. These holes were used to position the holder in the correct angle position with the backplate using parallel pins. The base has another two 6.5 mm in diameter holes at a 74 mm PCD. These holes are through holes on the base used to put M6 bolts that go through the radial slots on the backplate. The bolts are used to tighten the holder onto the backplate at the correct angular position. A 20 mm offset from the base to the manifold enclosure was added to the design to allow room for the M6 bolt heads and tools. The manifold enclosure side walls have straight slots which allow for adjustments to the manifolds to align them in the same plane.

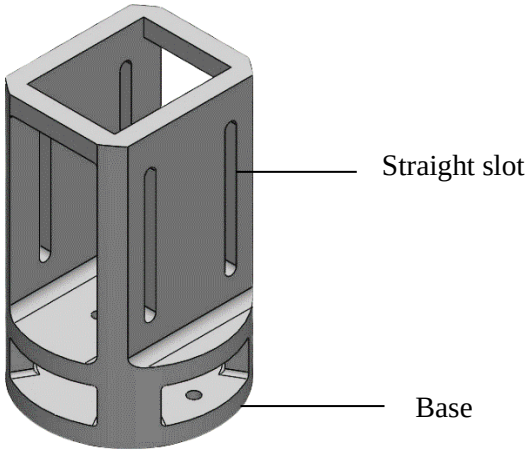

Figure 3-9: Concept 2-manifold bracket.

Concept Evaluation-Manifold Bracket

Both concepts were manufactured and tested on the injector frame to determine which concept was best suited for application on the test stand. Upon test fitting, it was noticed that the first design concept restricted the distance between the orifices of the injector elements. The "u" shaped bottom plate's extended surfaces interfere with each other at small impinging angles. This is illustrated in Figure 3-10.

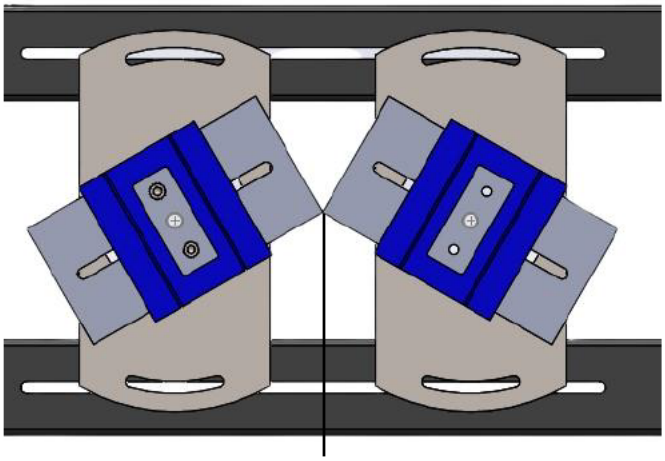

Figure 3-10: Concept 1 front view assembly.

The second concept does not have this problem because the bracket's base is the same as the width of the backplate. A vibrations test was carried out to verify that the brackets do not oscillate, especially at the commencement of a test. This was done because any perturbation of the bracket's set position causes a misalignment of the two jet streams. During testing, the first concept was found to be susceptible to misalignment of the jet streams. The second concept was not prone to such problems as it is bulkier and stiffer than the thin laser-cut plates of concept one.

Adjustments of the manifold's position in the first conceptual design were more challenging than in the second design because of the many slight adjustments to the bolts and nuts of the holder. In the second design, adjustments to get the two jets in the same plane were much easier because the holder is one solid part. Given the importance of alignment of the jet streams and how the first concept is sensitive to vibrations, the second concept was selected and used on the test stand. Figure 3-11 shows an isometric view assembly of the chosen concept assembled on the frame.

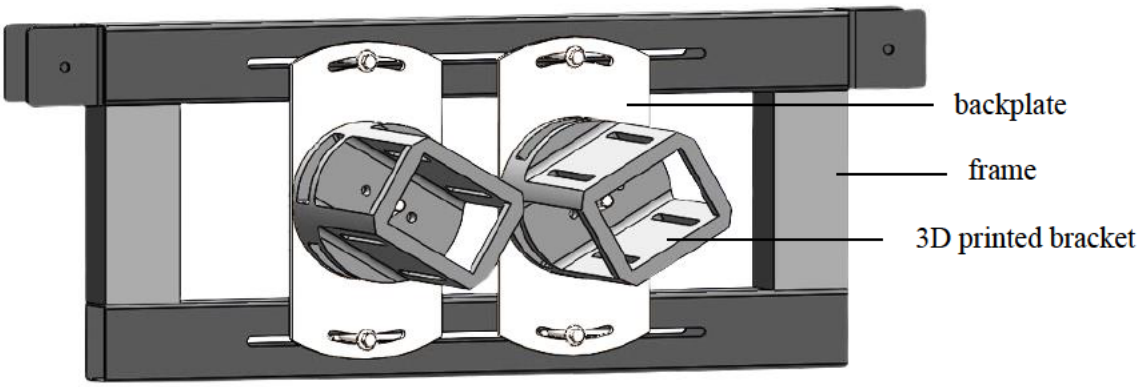

Figure 3-11: Concept 2 isometric view assembly

3.5 Storage Tank

The purpose of the storage tank/pressure vessel is to store and introduce gel propellant simulants into the pressurisation chamber. The tank is supported above the pressurisation chamber by a frame. Due to gels' non-Newtonian behaviour, a driving force was required to introduce the gel into the pressurisation chamber.

3.5.1 Concept 1-Open Tank

In this design, the tank is open to the atmosphere. The tank was constructed from a 76 mm mild steel cylindrical pipe and is presented in Figure 3-12. One end of the pipe was fitted with reducers, reducing the pipe diameter to ½ inch. A ½ inch pipe tube was welded on the reducers as the connecting feedline from the storage tank to the pressurisation chamber. In this concept, the simulant is gravity and vacuum fed from the storage tank to the pressurisation chamber. The storage tank sits above the pressurisation chamber, therefore, the simulant flows into the chamber due to gravity. However, gravity feeding is insufficient due to the non-Newtonian behaviour of the simulant. As a result, it was proposed that the piston be positioned at its fully extended position during filling and then retracted once the storage tank was filled with simulant. The retraction created a lower pressure to fill the pressurisation chamber.

Figure 3-12: Open storage tank

3.5.2 Concept 2-Closed Tank

In this design, the tank is closed to the atmosphere and the required driving force to introduce gel simulants into the pressurisation chamber was achieved by introducing compressed air/nitrogen into the

storage tank ullage to pressure feed the simulants into the pressurisation chamber. The feed pressure depended on the concentration of the gel simulant. The higher the concentration, the more viscous the simulant and as a result, a higher feed pressure was required. The gel simulants are only tested in the 2 to 14 bar injection pressure range in this application. Therefore, only gel concentrations within this injection pressure range were considered. A storage tank/pressure vessel that can feed gel simulants and be pressurised to a maximum pressure of 15 bar was required. Figure 3-13 shows an isometric assembly view of the storage tank/pressure vessel. The vessel consisted of a cylindrical shell, two slip-on flanges, two blind flanges, and pipe fittings.

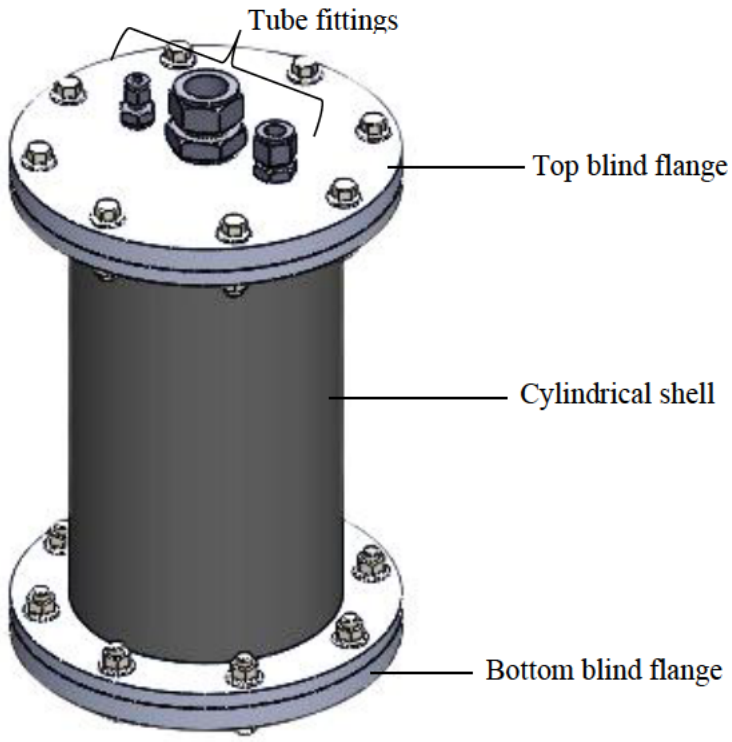

Figure 3-13: Closed storage tank isometric assembly view.

The cylindrical shell of the vessel is made of an Aluminum 6061 T6 tube with an outer diameter of 160.3 mm and a wall thickness of 4.5 mm. The cylindrical shell's maximum allowable working pressure (MAWP) was calculated using the lesser pressure value from the circumferential and longitudinal stresses. The MAWP for the cylindrical shell was calculated to be 138.42 bar. Design calculations for the vessel are given in Appendix A.

For this study, the open tank was selected because the investigated gels were not too viscous for gravity and vacuum feeding them to the chamber from the storage tank.

4. SYSTEM MODELLING

This chapter describes the mathematical and mechanical system modelling implementations to form a simulator of the test stand system. The mathematical model described in this section was used to determine the system-specific flow regimes and losses of system. A MATLAB® computational model was used to simulate the system in the Simulink® environment.

4.1 Single Phase Incompressible Model

The single-phase incompressible model (SPI) served as a method to evaluate the pressure drop (ΔP) across the injector and upstream feedlines at various mass flow rates. It is imperative to determine the pressure drop accurately, because it is used to determine the injection velocity. The system losses upstream of the injector orifice must be known to determine the required range of injection pressures. Therefore, the pressurisation chamber pressure must be determined to overcome system losses so that the injection pressure is at the desired value. Flow measurements using an orifice require a single-phase flow (Gupta and Roy, 2007). The equation used to describe single-phase mass rate, $\dot{m}_{SPI}$, flow is given by Equation (4-1).

$$\dot{m}_{SPI} = C_d A\sqrt{2\rho\Delta P} \tag{4-1}$$

Where C_d is the discharge coefficient, A is the orifice cross sectional area, ρ is the density of the working fluid, and ΔP is the pressure drop.

The test stand setup consisted of a high pressure hydraulic power pack coupled to a rod and piston to pressurise the chamber. The outlet end of the chamber is connected to half-inch tubing with a tee tube fitting that branches off into two half-inch flexible hoses downstream. The flexible hoses are connected to the inlet of the two injector manifolds. The force from the piston transferred the simulant fluid to the injector insert through half-inch connecting tubes.

The injection velocities were calculated using the mass flow rate for each injection pressure from the single-phase incompressible equation. The test rig was developed to test a single injector element. Therefore, there is no large manifold upstream of the orifice as in the case of multi-element orifices. A Microsoft (MS) Excel spreadsheet was created to calculate the system's pressure drop using input parameters given in Table 4-1.

Table 4-1: Input Parameters used to calculate system head losses of the test rig.

	Parameter	**Symbol**	**Value**	**Unit**
1	Orifice diameter	d_o	0.001	m
2	Discharge coefficient	C_d	0.60	-
3	Fluid density	ρ	1000	kg/m^3
4	Dynamic viscosity	μ	0.000893	Pa s
5	Insert roughness (Brass)	e_{inj}	0.0015	mm
6	Injection Pressure	P_{inj}	1.4	bar
7	Lines diameter	d_h /d_p	0.0127	m
8	Line roughness (stainless steel)	e_{line}	0.002	mm
9	Line length (rigid pipe)	len_p	2.4	m
10	Line length (flexible hose)	len_f	0.6	m
11	Length to orifice ratio	r	10	-
12	Number of bends	-	5	-
13	Number of tee connectors	-	1	-
14	Number of ball valves	-	2	-

A lookup table of injection velocities was created using these parameters with the single-phase incompressible model for injection pressures in the range of 1.4 kPa to 1400 kPa. The Reynolds number was calculated from the injection velocity to determine the flow regime in the injector insert. The flow velocity in the orifice allowed for the Darcy friction factor to be computed for the injector insert with a roughness value given in the input parameters table. The flow in the injector inserts must be turbulent to achieve atomisation (Fakhri, et al., 2009). Therefore, to calculate the friction factor, *f*, the Colebrook equation given in Equation (4-2) was used since it can find the friction factor for laminar, turbulent, and transitional flow through rough and smooth ducts.

$$\frac{1}{\sqrt{f}} = -2.0 \log\left(\frac{\frac{\varepsilon}{D}}{3.7} + \frac{2.51}{Re\sqrt{f}}\right) \tag{4-2}$$

In the above, *f* is the Darcy-Weisbach friction factor, ε is the orifice bore roughness, *D* is the hydraulic diameter of the orifice, and *Re* is the Reynolds number. The Colebrook equation was solved numerically due to its implicit nature. An iterative method was employed, using the Haaland equation as a starting point value of f given in Equation (4-3).

$$\frac{1}{\sqrt{f}} \cong -1.8\log\left(\frac{6.9}{Re} + \left(\frac{\left(\frac{\varepsilon}{D}\right)}{3.7}\right)^{1.11}\right) \tag{4-3}$$

The Colebrook iterative solution was implemented using the "goal seek" function in Microsoft Excel. Once the friction factor was determined, the pressure loss due to friction was computed using Equation (4-4)

$$\Delta P = \frac{fL\rho V^2}{2D} \tag{4-4}$$

where L is the length of pipe through which the fluid flows, and V is the fluid velocity. The energy losses due to friction for the connecting lines were also calculated using the equation above. The flow regime in the half-inch (12.7 mm) connecting lines was determined to be laminar thus the friction factor is only dependent on the Reynolds number in this region. The friction factor in the connecting lines was determined using Equation (4-5) .

$$f = \frac{Re}{64} \tag{4-5}$$

The gradual contraction from the flexible hose to the injector manifold downcomers caused a pressure drop, which together with the minor losses in the connecting lines, was calculated using Equation (4-6).

$$h = K\frac{V^2}{2g} \tag{4-6}$$

In the above h is the minor head losses and K is the minor loss coefficient associated with a specific component (e.g. tee). The Microsoft Excel spreadsheet computed all calculations by supplying an injection pressure value. From the spreadsheet, the total system head loss was determined. The information from these calculations together with the Simulink® model, was used to determine the setting of the pressure relief valve on the hydraulic power pack to achieve the desired injection pressure whilst accounting for head losses in the system. Table 4-2 shows the calculated pressure drops for the injection pressure range investigated.

Table 4-2: System pressure drop results using SPI model.

Injection Pressure [bar]	Injector Flow Regime	Lines Flow Regime	Injector Major Losses [m]	Injector Minor Losses [m]	Lines Major Losses [mm]	Lines Minor Losses [mm]	Total System Head Loss [m]
1.5	Turbulent	Laminar	1.76	1.65	3.10	0.05	3.42
2	Turbulent	Laminar	2.28	2.20	3.60	0.72	4.49
2.5	Turbulent	Laminar	2.79	2.75	4.10	0.90	5.55
3.5	Turbulent	Laminar	3.78	3.85	4.80	1.30	7.65
4	Turbulent	Laminar	4.28	4.40	5.10	1.40	8.68
4.5	Turbulent	Laminar	4.81	4.95	5.40	1.60	9.78
5	Turbulent	Laminar	5.25	5.50	5.70	1.80	10.76
5.5	Turbulent	Laminar	5.72	6.06	6.00	2.00	11.79
6	Turbulent	Laminar	6.20	6.61	6.30	2.20	12.81
7	Turbulent	Laminar	7.14	7.71	6.80	2.50	14.86
8	Turbulent	Laminar	8.08	8.80	7.30	2.80	16.90
9	Turbulent	Laminar	9.01	9.91	7.70	3.20	18.93
10	Turbulent	Laminar	9.93	11.01	8.10	3.60	20.95
11	Turbulent	Laminar	10.85	12.11	8.50	4.00	22.97
12	Turbulent	Laminar	11.76	13.21	8.90	4.30	24.99
13	Turbulent	Laminar	12.67	14.31	9.20	4.70	26.99
14	Turbulent	Laminar	13.58	15.41	9.60	5.00	29.00

4.2 Simulink® Computational Model

This section describes the MATLAB® Simulink® modelling implementation of the system. The block modelling approach was employed to simulate the test procedure and verify that the calculated pressure relief valve setting of the hydraulic power pack will yield the desired injection pressure. Simulink® employs a physical network approach, where blocks representing the physical components are connected just as the physical components on the test rig would be assembled. The test rig has multidomain physical systems, therefore, Simulink® add-on products were used (e.g., Simscape fluids). The following physical domains were used to model the test rig:

1. Electrical
2. Hydraulic
3. Isothermal liquid

4. Mechanical rotational and transitional

Connecting blocks in Simulink® is analogous to connecting real components. The connection ports are nondirectional, and connecting elements together results in interactions between the elements by exchanging energy through their ports. The model supports ‘through variables’ and ‘across variables’. Through variables are connected in series to the element, for example the flowmeters on the two flexible hoses in the model are of this type. Across variables are connected in parallel to the element, such as pressure gauges on the injector elements. The Simulink® implementation is shown in Appendix B.

The model has two subsystems, one for the hydraulic power pack and the other for stainless steel tubes. The hydraulic power pack subsystem is illustrated in Figure 4-1. The hydraulic subsystem has a fixed displacement pump driven by an angular velocity source at a nominal speed of 188 rad/s which is derived from the specifications of the induction motor on the power pack. A pressure relief valve was added to the model subsystem to control the load in the system. The system's load is the force the hydraulic actuator applies to the piston in the pressurisation chamber. Therefore, the pressure can be controlled by controlling the load on the hydraulic power pack using the hydraulic pressure relief valve. The “P” line from the pump is also connected to the “P” port of the directional control valve. Hydraulic fluid flows to the valve when the relief valve is closed. The outlet port of the relief valve is connected to the tank to direct flow back into the tank when the valve opens as it would with the physical hydraulic power pack.

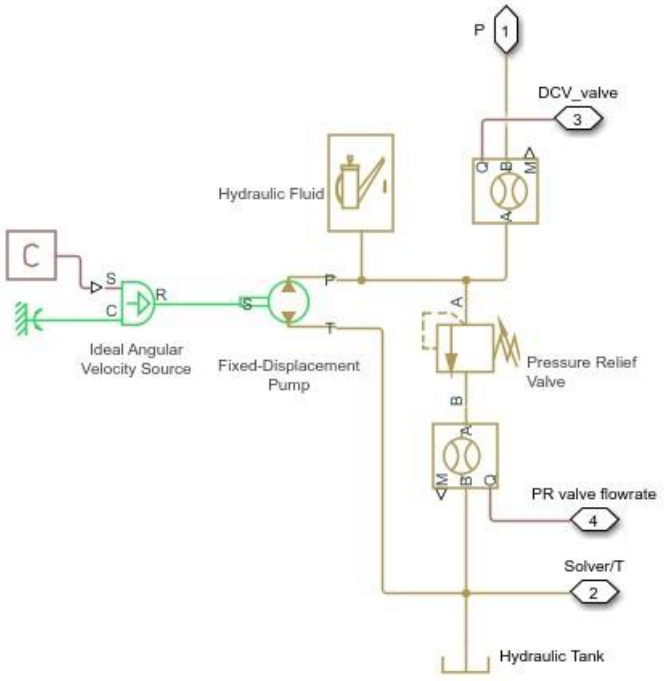

Figure 4-1: Hydraulic power pack physical model.

The pipeline subsystem shown in Figure 4-2 was used to model the stainless-steel tubes and tube bends on the test rig. The inlet connection port of this subsystem was connected to the pressurisation chamber outlet port. A series connection of pipes and bends were used to describe the tubes on the test rig. The tubes and bends modelled flow dynamics due to viscous friction losses, pipe bend losses and the effects of elevation. The outlet of the pipe subsystem was connected to the inlet port of the 'Tee' component that splits the flow equally into the flexible hoses. 'A' and 'B' on the diagram represent the inlet and outlet of the block respectively. The annotations also provide the direction of fluid flow which in this case is from A to B.

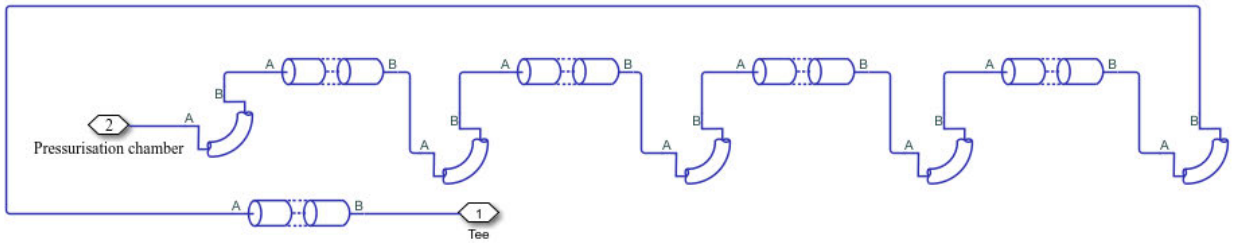

Figure 4-2: Tubes and bends subsystem.

From the hydraulic power pack subsystem described, there are four output ports. Two ports are used as through ports to connect mass flow rate measuring components to measure the flow of hydraulic fluid to the directional control valve (DCV) and the flow through the pressure relief valve. The remaining two ports labelled 'P' and 'T' are the hydraulic ports associated with the directional control valve inlet ports. A double-acting hydraulic cylinder block is used to model the hydraulic actuator. The DCV block controls the actuation of the cylinder. The block model was used as a translational hydro-mechanical converter. The piston inside the pressurisation chamber was modelled with a mass block connected to a translational mechanical converter block.

The converter block models the interface between the simulant and the piston. The liquid outlet port of the converter block is connected to the inlet port of the pipes and bends subsystem. Two across-variable measuring components are connected on the outlet port of the converter block and the outlet port of the pipe and bends subsystem. The measured variable (pressure) is used to predict the chamber pressure and determine the pressure drop across the pipeline and bends subsystem.

A T-junction block is used to model a 'Tee' tube fitting to split the flow to each injector manifold. The two streams flow through flexible hoses modelled by pipe blocks with flexible wall specifications. An area change block is used to model the gradual area change from the flexible hoses to the manifold inlet. An orifice block is used to model the injector element after the area change block. The orifice outlet port is connected to a reservoir set to a constant boundary condition resembling atmospheric conditions.

Pressure gauge blacks are connected between the area change block and the orifice to measure simulated injection pressures.

A MATLAB® script was developed to plot the results generated from the model. The script was also used to input parameters needed by the Simulink® component blocks. The script is given in Appendix C. The Microsoft spreadsheet and Simulink® model were used together in a format where:

1. the system head losses were calculated using the single-phase incompressible model at the desired injection pressure.
2. the calculated head loss was summed with the injection pressure to find the load pressure.
3. the load pressure calculated was set as the relief pressure on the hydraulic subsystem.
4. simulations were run to verify the injection pressure.

The model was validated with experimental data. It was found that the model adequately simulated the injection pressure. Figure 4-3 shows the simulated and experimental results of the injector element for a piston force of 1720 N.

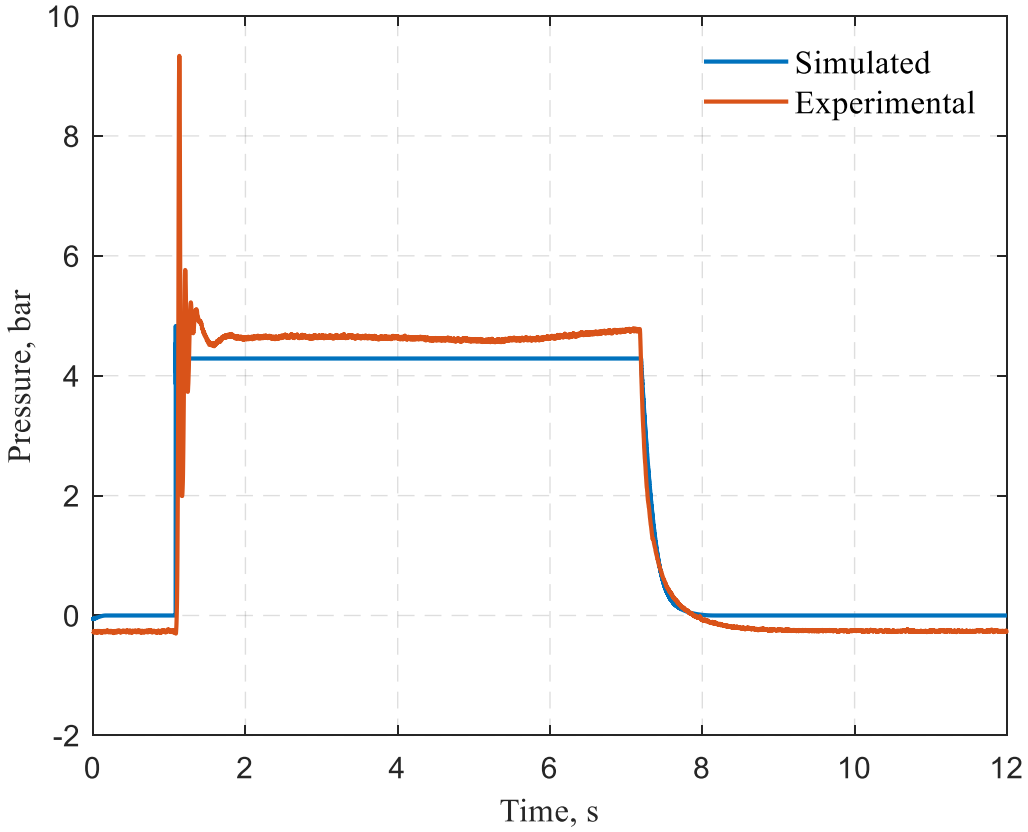

Figure 4-3: Simulated and experimental results of injection pressure

5. EXPERIMENTAL SETUP

This section describes the experimental setup of the test rig and the instruments used to collect data during the capture of image data on spray sheet breakup.

5.1 Test Rig

The spray sheets investigated in this study are formed by the collision of two jet streams with the same fluid at equal momentum impacting one another at an angle 2θ. An image of the injector element configuration is shown in Figure 5-1. The impinging angle can be varied between 0 and 180 degrees.

Figure 5-1: Injector element configuration.

A schematic drawing of the layout of the experimental test rig is presented in Figure 5-2. It comprises of a hydraulic power pack for the hydraulic cylinder actuator, an electro-pneumatic valve, test injector elements, a pressurisation chamber, a storage tank, a data acquisition system, and a high-speed digital camera.

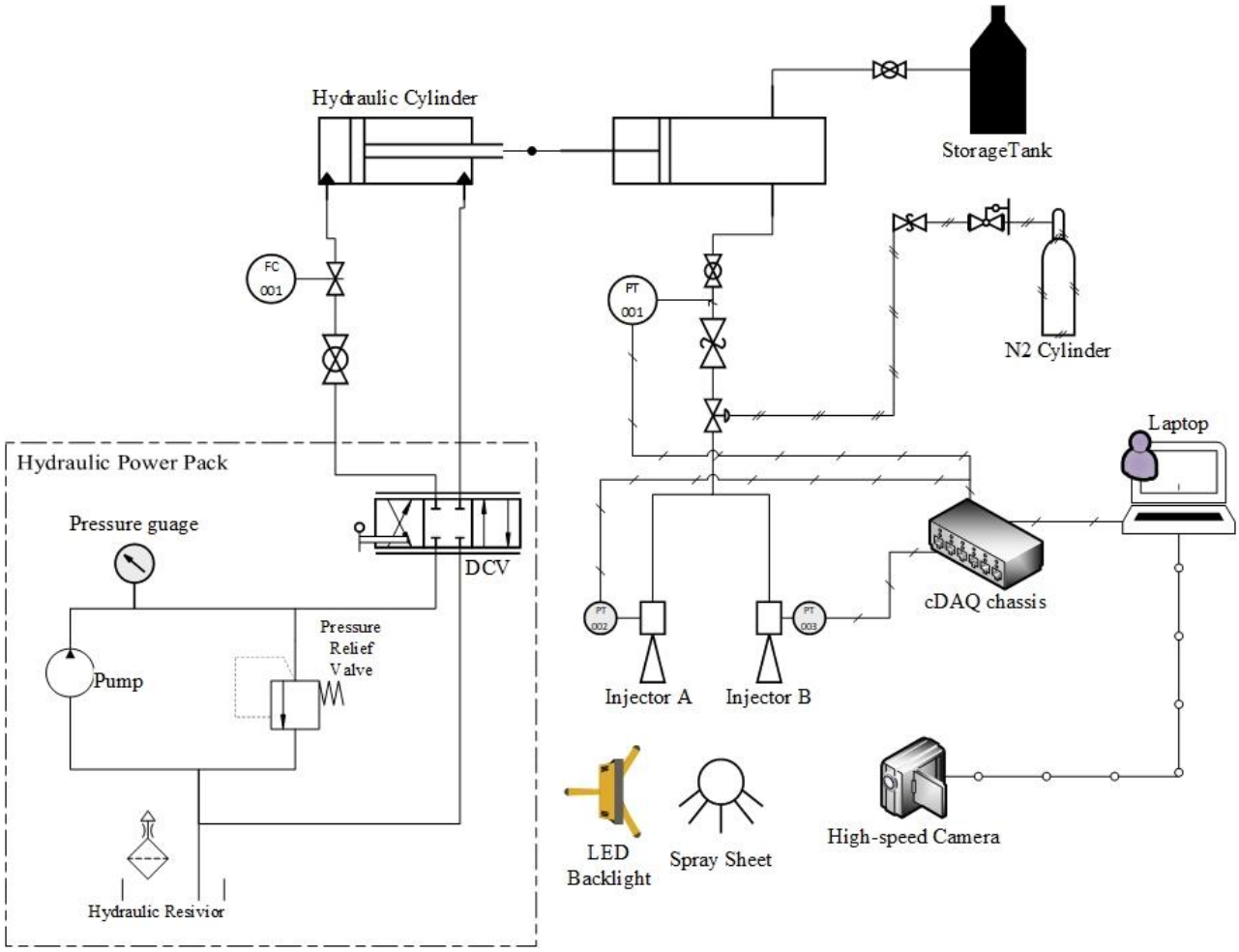

Figure 5-2: Schematic of the test rig.

The gel simulant is introduced into the pressurisation chamber by a negative pressure created by retracting the piston once the storage tank is filled with simulant. Alternatively, a high-pressure gas in the tank's ullage pushes the simulant into the pressurisation chamber when the closed storage tank is used. The pressure in the storage tank is regulated from the compressed gas source (compressor/N_2 gas bottle) through a regulator valve and monitored on a pressure gauge. The simulant is forced into the injector element manifold by the piston actuated by the hydraulic cylinder using a directional control valve on the power pack. There is a ball valve on the feedlines between the chamber and the manifold. This valve is either in the fully open or fully closed position, and the actuation of this valve is done using an electro-pneumatic valve actuator which is controlled by a LabVIEW™ program. A nitrogen gas cylinder supplied the gas to actuate the valve. The pressures inside the pressurisation chamber, injector element A manifold, and injector element B manifold are monitored by pressure transmitters (WIKA A-10) labelled PT001, PT002, and PT003 on the schematic diagram. The mass flow rate is calculated analytically by recording the time and distance the piston has moved in the pressurisation chamber. The injector element insert is shown in Figure 5-3. The insert has a 5 mm entrance diameter that converges to 1 mm diameter.

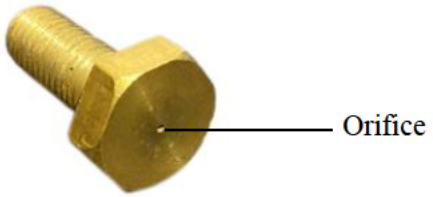

Figure 5-3: M10 bolt injector insert.

The modular injector frame configuration allows easy assembly of the manifolds and change of injector element inserts. It allows for adjustments of impinging angles and distance between the orifices. A Chronos 1.4 high-speed camera was used to visualise the generated liquid sheet. The camera provides a 1.4 gigapixel per second throughput for capturing high-speed monochrome videos from a 320 x 96 resolution (minimum) at frame rates above 40 000. Figure 5-4 shows a sprayed sheet captured with the Chronos 1.4 camera. Backlighting was used to separate the subject and the background. The backlit images were captured at 6340 frames per second with the camera fitted with a Computar 12.5-75 mm f/1.2 zoom lens. The spray sheet was illuminated with a 30 W light emitting diode with a softbox and diffuser. The highspeed footage was captured using parameters summarised in Table 5-1 . Using these imaging parameters, the subject was captured 60 times before it went outside the field of view and gave the least number of pixels created by blur. The blur in pixels with these parameters was 0.53 and 1 pixel for the vertical and horizontal resolutions, respectively.

Table 5-1: Imaging parameters for spray sheet visualisation in backlit mode.

Parameter	**Specification**
Frame rate (fps)	6340
Resolution	320 x 640
Exposure (µs)	152.16
Field of view (FOV) (m)	0.331
Sheet to lens distance (m)	1.4

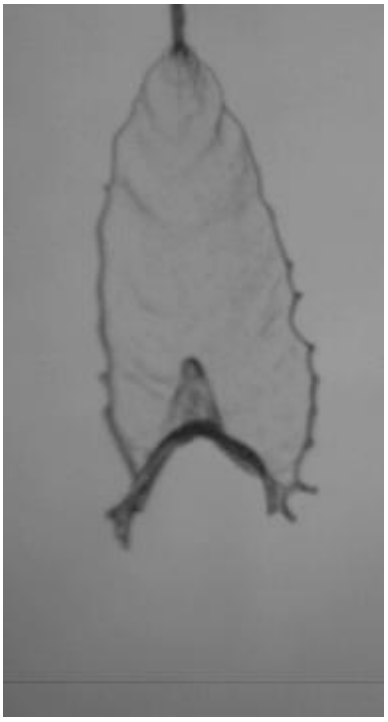

Figure 5-4: Sprayed liquid sheet.

The high-speed camera uses a ring buffer in its internal high-speed random access memory (RAM) to save recorded video footage. The ring buffer is a data structure that holds frames of recorded video. When the ring buffer is full, old frames are overwritten as new frames are captured. This data structure allows the camera to record for an unlimited time, but only the most recent frames in the buffer are retained. An external trigger was used to stop recording, and the camera used the ring buffer to save the last few seconds of video footage. The duration of the video depends on the recording settings before starting the recording. A BNC connector (external trigger) was configured in this setup to stop recording with the 'record end' trigger feature, which terminates recording. The BNC line was connected to a relay module line on the cDAQ system which pulled the input/output port (IO1) on the camera to low, triggering the 'record end' on the camera. This configuration is used on the camera with the following IO settings:

- Pullup (20 mA).
- The signal conditioning was set to debounce.
- The trigger type was set to record end trigger.

These settings trigger the line from HIGH to LOW when the relay module on the cDAQ activates. A low signal to the port terminates recording.

5.2 Test Rig Operation

The piston reciprocates inside the pressurisation chamber actuated by a hydraulic cylinder. The power pack can actuate the piston back and forth in the cylinder with a maximum load of 250 MPa. The extension and retraction motions of the cylinder are controlled by a 4-way 3-position DCV. The valve controls the extension and retraction of the cylinder. A flow control valve is connected in between the power pack and the actuator to control the speed of the piston in the chamber. This is called a meter-in configuration in hydraulic circuits, and it is chosen because the load on the hydraulic cylinder needs to be constant. An electro-pneumatic valve on the feedline between the chamber and the injector element manifold is used to control simulant flow to the injector elements for the test duration and close once the test is complete.

The impinging angle is set by aligning the zero-reference mark on the manifold brackets with markings scribed on the backplate. The backplate has angle reference lines scribed at 22.5º, 30º and 45º from the zero degrees reference. Therefore, if a 60º impinging angle 2θ is required both, manifolds would be positioned on the 30º angle on the backplate. The manifolds move inside a cavity on the brackets to get the two jet streams in the same plane and to correct misalignment.

5.3 Control System

A compactDAQ™ unit was used for control and measurement instruments on the test rig. CompactDAQ™ is a portable data acquisition platform that consists of a controller and C series input/output (I/O) modules. This conforms with the modular design philosophy of the test rig as it is a modular system that allows adding more measurement types and channels by adding modules to the chassis. Therefore, more control functionality can be exercised upon this system. The control system hardware consisted of a four slot cDAQ-9174 chassis and two C series I/O modules. The cDAQ-9174 can be reconfigured and moved from the development lab to the test field. The cDAQ-9174 has two input modules for test operations, the NI-9203 and NI-9481. The NI-9203 is a C series eight channel current input module that acquires samples at 200KS/s. The module can measure current from -20 mA to 20 mA. The second module on the chassis is the NI-9481, which has four channels with single-pole, single-throw (SPST) relay switches. Each channel on the module offers access to an electromechanical relay for switching signals. The module has two interchangeable terminals, CHa and CHb to link instruments. The NI-9481 module is used to actuate the ball valve.

Three WIKA A-10 pressure transmitters are used with the NI-9203 analogue current input module to measure the pressure at various points on the test rig. PT 001 is used to measure the pressure in the chamber. PT002 and PT003 are used to measure the injection pressures at the manifolds for each injection element. The pressure transmitters have a pressure measuring range of 0 to 40 bar and an output signal of 4 to 20 mA. Figure 5-5 shows the wiring diagram of the system described. In the diagram, the blue lines represent a physical connection of the C series modules to the cDAQ.

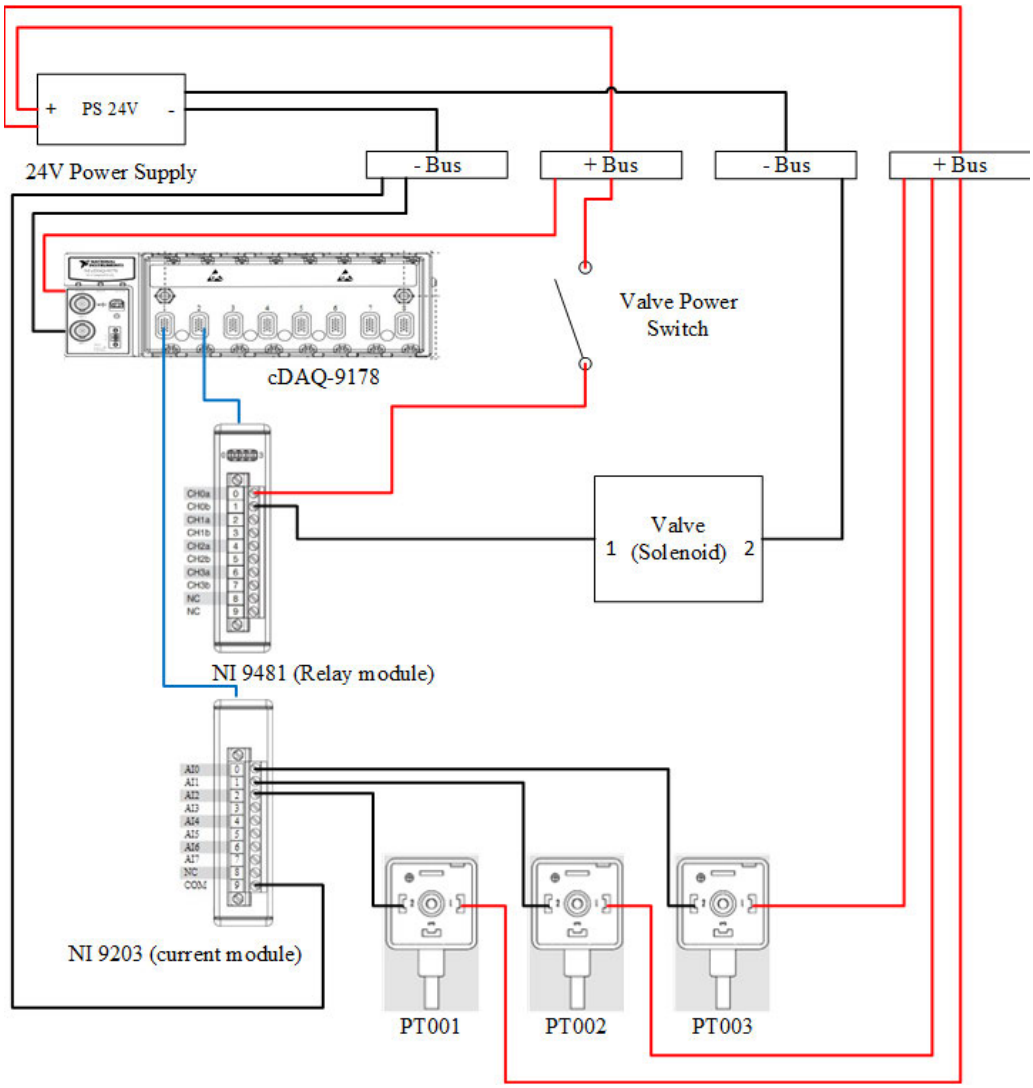

Figure 5-5: Control system wiring diagram.

5.4 LabVIEW Application

The control and monitoring application for the test stand was developed on LabVIEW™. The developed application uses a state machine design pattern to implement decision-making algorithms. It consists of a case structure contained in a while loop, and each case can lead to another case or end the flow process.

Two applications were developed for the system. The first application was used to manually control the valve for filling and priming the system. Figure 5-6 and Figure 5-7 show this application's block diagram and front panel, respectively The second application was used to automate the test procedure which consisted of a while loop containing two DAQ assistants; a filter, a write-to-measurement file, and a valve actuator control button.

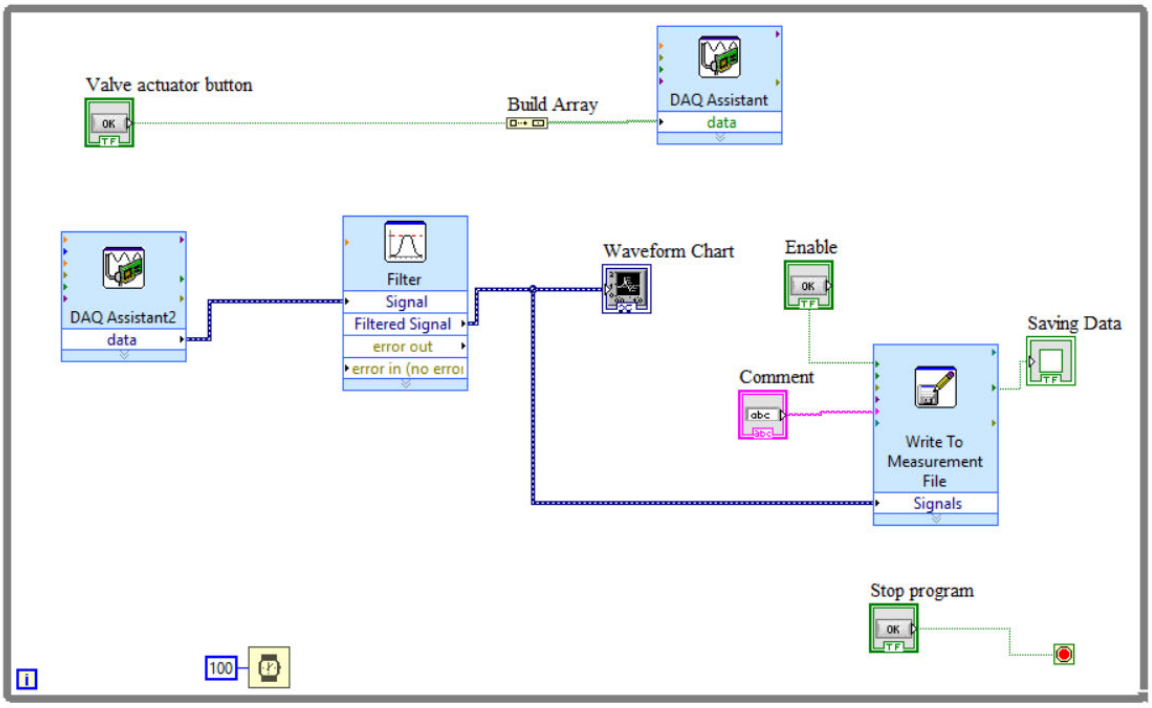

Figure 5-6: Manual control block diagram.

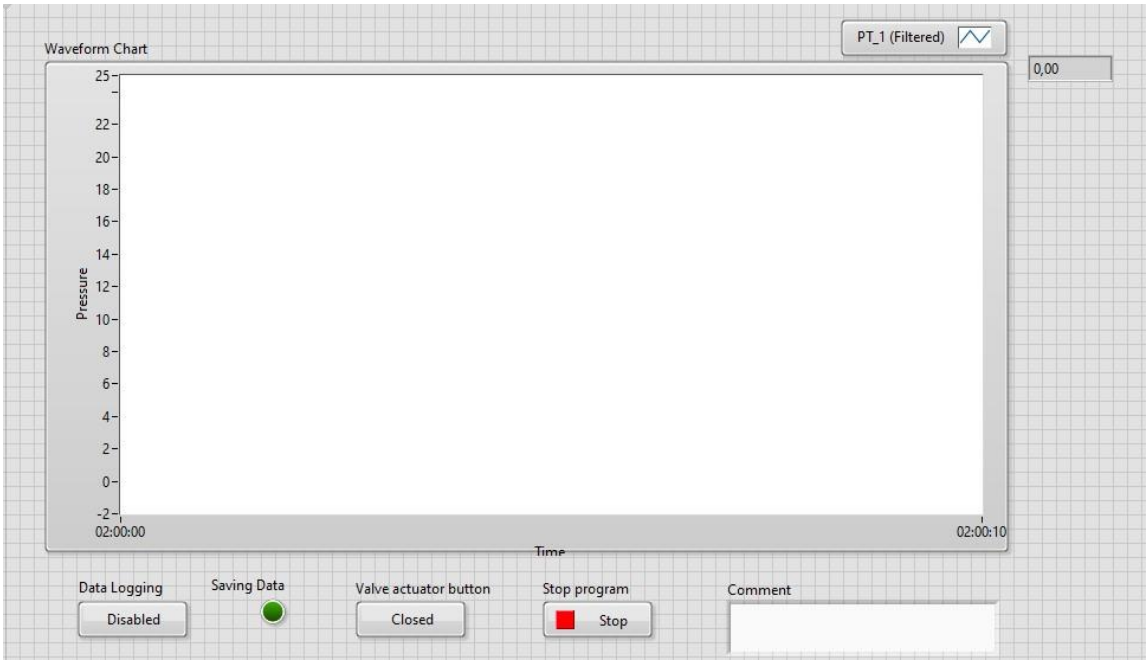

Figure 5-7: Manual control front panel.

One of the DAQ assistants also linearly scales the current measurements from the pressure transmitters to get an output signal in units of pressure. The linear scale used is given by Equation (5-1). The scaled pressure measurements are graphed on a waveform chart for visualisation on the front panel of the application.

$$y = 2500x - 10 \quad (5\text{-}1)$$

In the linear scale equation, x is the current measurement from the pressure transmitter in milliamperes and the resultant y-value is the pressure in bar. Figure 5-8 shows the front panel of the test application.

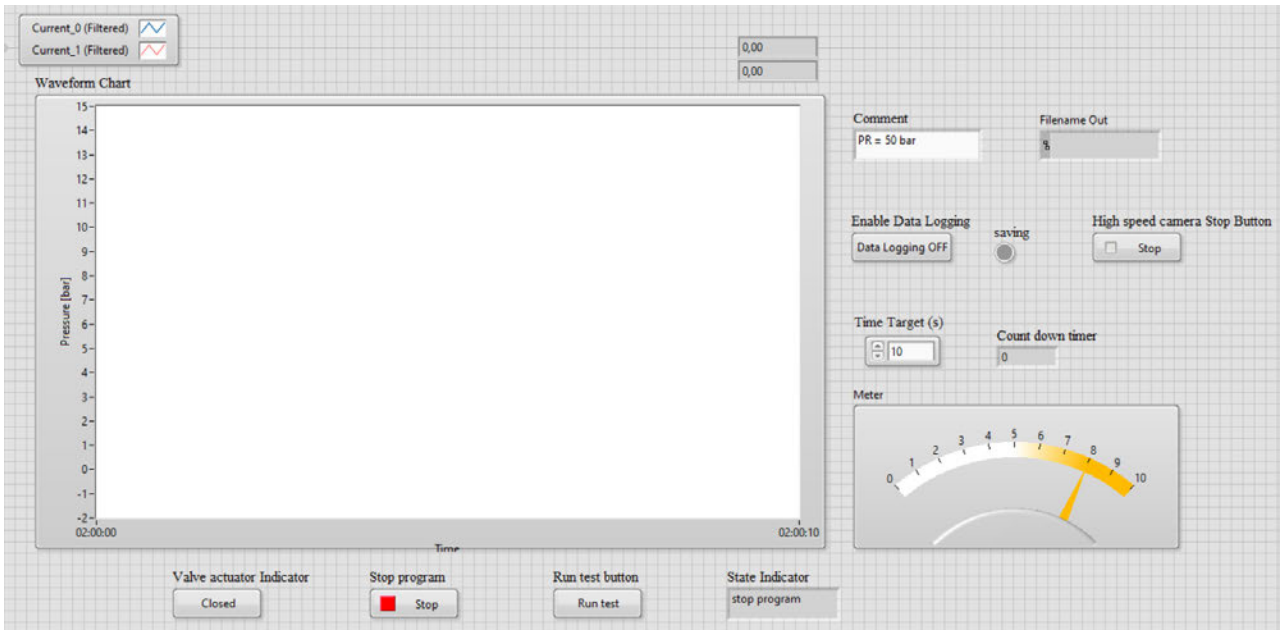

Figure 5-8: Test Application front panel.

This applications block diagram consists of two while loops that run in parallel. The first loop shown in Figure 5-9 takes measurement readings from the pressure transmitters, logs the data, and displays it on a waveform chart on the front panel.

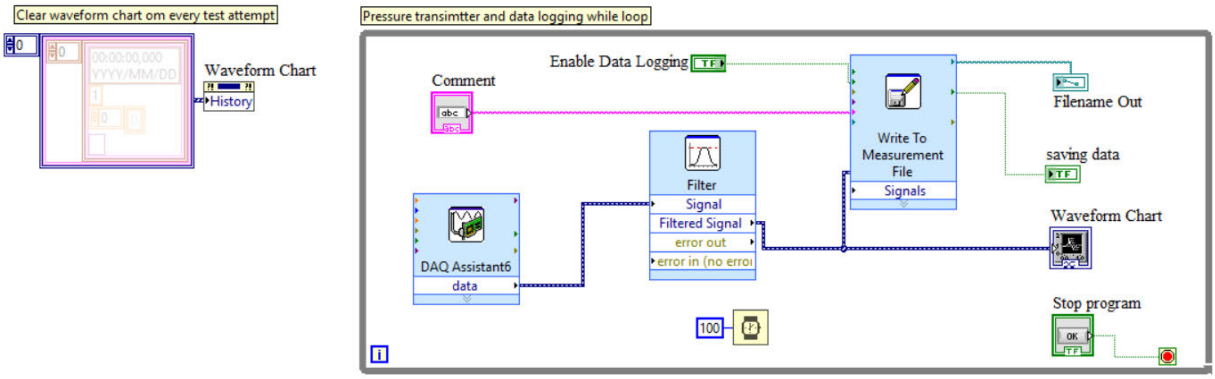

Figure 5-9: Test application while loop one.

The second while loop shown in Figure 5-10 implements the decision algorithm to automate the test procedure.

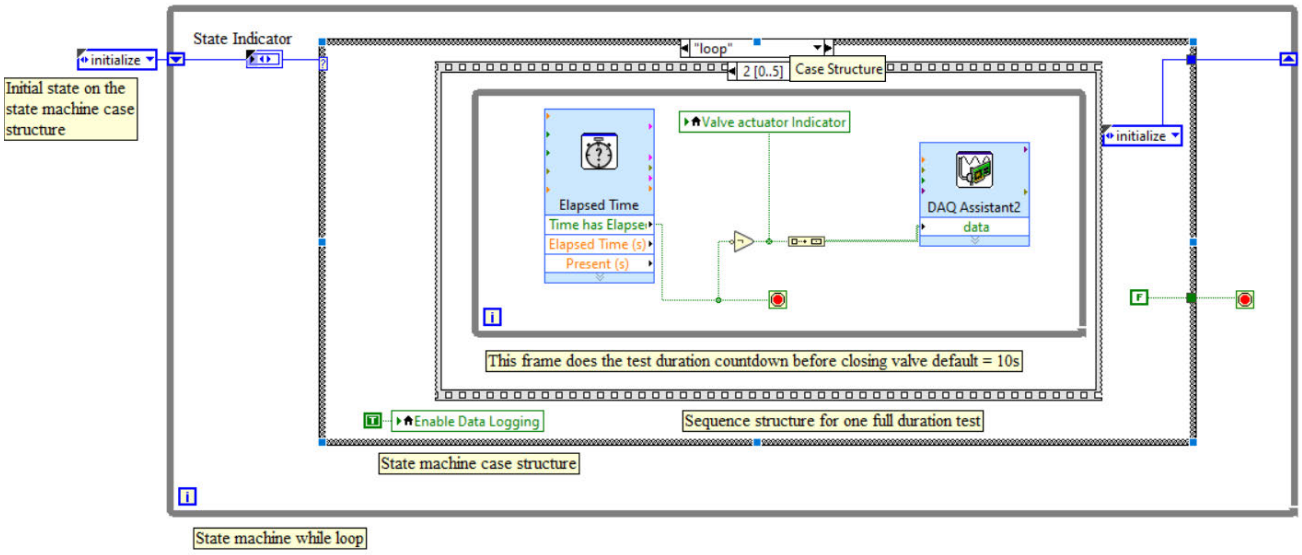

Figure 5-10: Test application while loop two.

5.5 State Machine Program Explanation

The state machine described in Section 5.4 contains a case structure in a while loop. A state machine diagram for the test rig is illustrated in Figure 5-11. The 'initialise' state is the first state executed, which is determined by the numerical control case selector outside of the while loop. On start-up, the case selector executes the initialise state where the valve is closed. Data logging is also switched off to ensure no data are logged before a test. Once actions in the initialise state are completed, the program moves to state 2: the idle state. The idle state in the diagram shows a state block with sub-states within the block. That is because an event structure controls the state executions once initialisation is completed. The machine can move to the loop that implements the test procedure or end the program from the idle state.

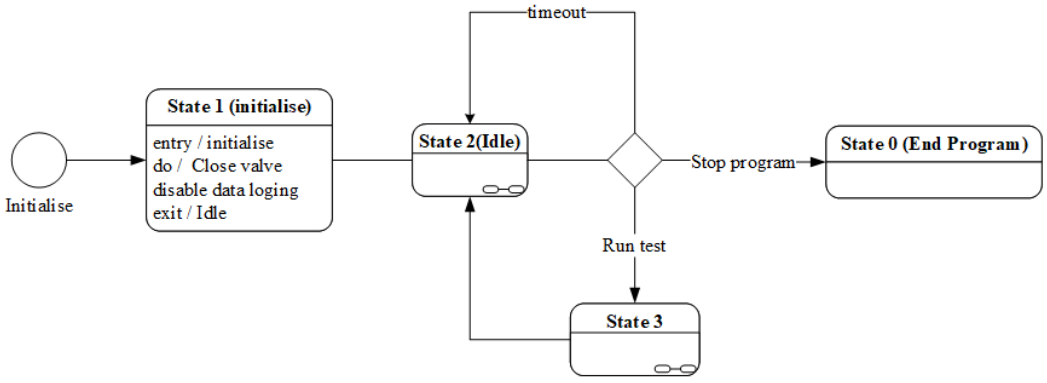

Figure 5-11: State machine diagram.

Figure 5-12 shows the decision-driven flow diagram of the event structure in the idle state. The program only goes into the idle state if the states of the stop and run buttons are false. Once in the idle state, one of three possible actions can occur.

1. The event structure times out (if set to timeout), returns to the initialise, and then returns to the idle state.
2. The stop program button is pressed, and the application is terminated.
3. The run test button is pressed and the application runs through the test process sequence.

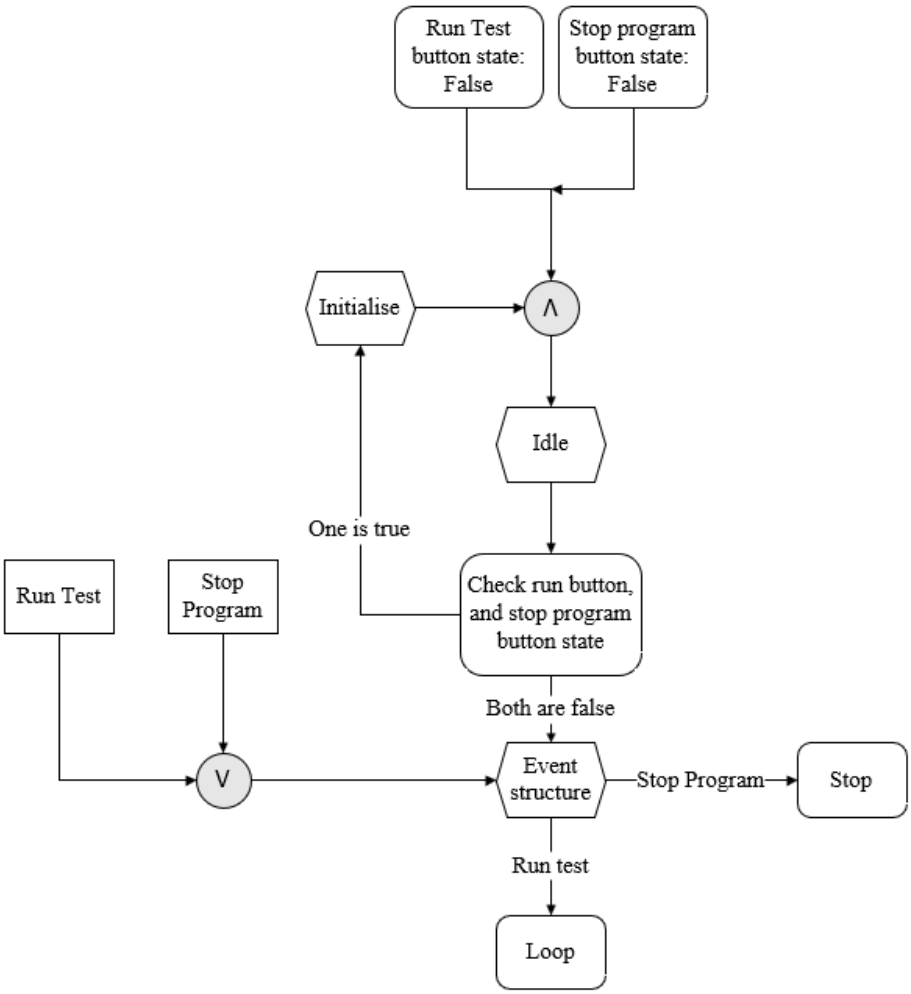

Figure 5-12: Event structure decision diagram.

The event structure registers the second action as a state change on the stop program button. This action changes the state machine from state 1 (idle) to state 0 (end program). When a button state change occurs, the stop condition in the first while loop becomes true. The true constant can only be read when

the state machine enters state 0 (end program). Action two terminates both while loops running in parallel, shutting down the application.

The third action commences a sequence of actions in the loop state (state 3). When the ‘run test’ button is pressed, the event structure reads and registers the buttons state change. When this happens, the program switches from the idle state to the loop state. The sequence of events that happen in the loop state are shown in Figure 5-13. The stacked sequence structure has five frames running in sequence, each performing a specific task. The state blocks in the diagram represent each frame and the actions that take place.

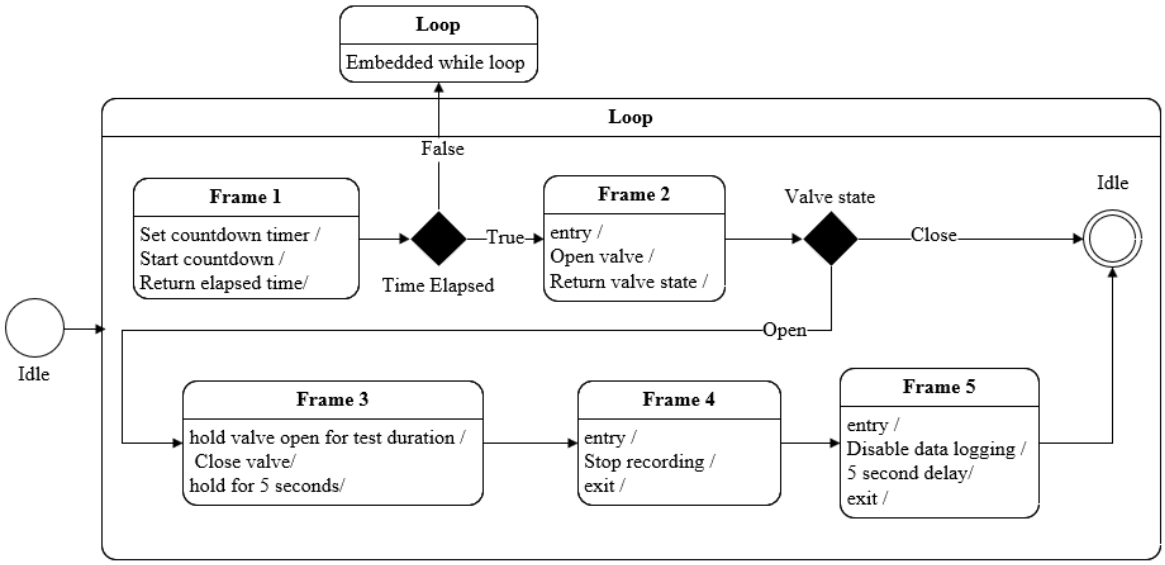

Figure 5-13: Loop state events diagram.

Frame 1: This frame embeds a while loop containing a timer. The timer is controlled with a numeric control where the user can set a countdown time target. When the specified time elapses, the frame returns a Boolean control on its output lines to move onto the second frame.

Frame 2: If a true Boolean control signal is received the valve is opened and the sequence then moves to the next frame when the valve actuation is completed.

Frame 3: This frame contains a while loop which keeps the valve in the open position for the test duration. When the specified test duration elapses a Boolean control signal closes the valve and moves onto the fourth frame.

Frame 4: This frame is used to trigger the stop record button on the high-speed camera. A “true” Boolean constant control signal is sent to the camera to stop recording.

Frame 5: This frame disables data logging and delays for 5 seconds before proceeding to the idle state to ensure no data is lost from the buffer after the test.

6. GEL FORMULATION AND CHARACTERISATION

This section describes the formulation and characterisation of the gel simulants used in the study.

6.1 Gel Simulant Formulation

For the gelled simulant, water was used as the base liquid and mixed with xanthan gum and guar gum. A two-blade, 6-speed mechanical mixer shown in Figure 6-1 was used to mix the water and gelling agents uniformly. All mixing was carried out at room temperature, which was between 25 and 26 ºC on the days of mixing. The selected gelling agents are plant-derived hydrocolloids with cold water solubility. These substances are soluble in cold water, but it dissolves and mixes more effectively when heated (Fallourd and Viscione, 2009). These water-based gel simulants were tested in the monopropellant mode (like-on-like) with varying gelling agent concentrations ranging from 0.5 to 1.5 wt% (weight percentage). This concentration range was chosen because higher concentrations increase the stability from strong networks via hydrogen bonding. These bonds resist the liquid breakup and subsequent spray formation resulting in poor atomisation.

Figure 6-1: Two-blade mechanical mixer.

Five litres of xanthan gum and guar gum simulants were prepared for testing. The quantity was too large to prepare in a single batch obtain a uniform, homogenous mixture for this mentioned volume. Therefore, formulations were done in batches of one litre. The weight percent formula was used to describe the concentration of the simulant in terms of the relative percent concentration of solute in a solution. Equation (6-1) was used to determine the weight percent of the solution.

$$\%w = \frac{g\ of\ solute}{g\ of\ solute + g\ of\ solvent} \times 100 \tag{6-1}$$

This equation was rearranged to calculate how much solute was required to make a 1000 g (1 litre) solution. Table 6-1 shows the results of the calculated mass of solute required to be dissolved in 1000 g of water to yield a weight percent of 0.5, 1, and 1.5%.

Table 6-1: Solute mass calculation results.

	Weight percent [%]	**Mass of solvent [g]**	**Mass of solute [g]**
1	0.5	1000	5.03
2	1	1000	10.1
3	1.5	1000	15.23

The solute and solvent were measured to quantities described in Table 6-1. The solvent is first poured into the mixing bowl. Then the solute is added in small quantities so that the mixing blades do not deposit the gelling agent (powder) onto the bowl walls on initial contact. When the initial mixing speed is too high, the powder gets deposited onto the bowl walls, this is illustrated in Figure 6-2 . Therefore, to prevent this from happening, small amounts of the gelling agent were added in 5-minute intervals at low speed.

Figure 6-2: Mixing at high initial speed.

Once a significant amount of powder was added to the mixture it began to thicken. As the mixture thickened the mixing speed was increased. The mixing time for one batch took about 35 minutes. This mixing time ensured that the resulting mixture was homogenous and that little to no gelling agent was lost to the bowl wall during mixing. A loss of gelling agent to the walls would have resulted in an incorrect concentration. Figure 6-3 shows a batch mixture following the described mixing method.

Figure 6-3: Mixing at low initial speed.

6.2 Rheological Characterisation

Gel characterisation was done to verify that the prepared gel simulants show shearing thinning behaviour. Selected gels were characterised using an AR 1500ex rotational rheometer with a 40 mm parallel plate geometry. All rheology studies were done using the parallel plate configuration, as illustrated in Figure 6-4. The rheometer was used in the controlled rate mode to detect the rheological behaviour of the gelled simulants. The rheometer imposes a shear stress ranging from 1 to 1000 Pa on the samples, and the shear rate and viscosity are measured. A parallel plate geometry was used because it offers advantages like easy preparation and the strain is distributed uniformly in the gelled sample. The Peltier plate was used to control the temperature. A temperature of 25 º C was used during testing.

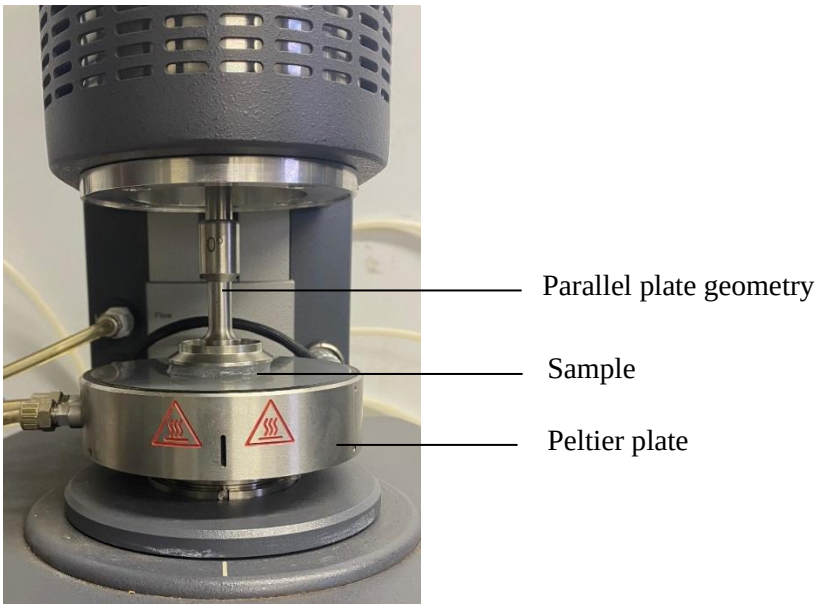

Figure 6-4: Rheometer parallel plate configuration.

The Rheology Advantage Software was used to design a test procedure for rheology studies of the samples. The test procedure was executed in a sequence of steps as follows:

1. Conditioning step
2. Continuous ramp step
3. Post-experiment step

The conditioning step is used to ensure that the test sample is at the correct temperature, and a pre-shear is applied to the sample. The pre-shear is performed to remove any history from the test sample from preparation and loading. The second step is the continuous ramp step in which the shear stress is increased and data are sampled at defined time intervals. The post-experiment step is used to automatically save the data generated. This procedure generates curves of viscosity versus shear rate. The curves are plotted on logarithmic axes to identify the different flow regions of the simulant and to confirm that they follow the generalized flow curve shown in Figure 6-5 .

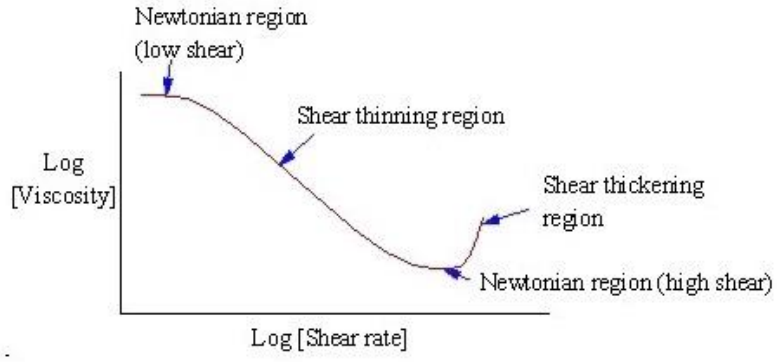

Figure 6-5: Generalized flow curve.

The nature of the curves were used to ascertain that the samples are within the shear-thinning region and can be described by the power law.

6.3 Gel Viscosity

The following section focuses on the rheological behaviour of the gel simulants. Six samples with compositions summarised in Table 6-2 were tested using the procedure described in section 6.2. The tests were done for two water-gelling agent mixtures at different concentrations (0.5, 1, and 1.5 wt%). Henceforth, a gel simulant is identified by the type and concentration of the gelling agent in weight percent. That is, x0.5 refers to gelled water with 0.5% xanthan gum by weight, and g0.5 referred to gelled water with 0.5% guar gum by weight.

Table 6-2: Composition of tested gel water simulants.

Sample no:	Gel simulant	Composition (wt%)		
		Water	Xanthan gum	Guar gum
1	x0.5	99.5	0.5	-
2	x1.0	99	1.0	-
3	x1.5	98.5	1.5	-
4	g0.5	99.5	-	0.5
5	g1.0	99	-	1.0
6	g1.5	98.5	-	1.5

Figure 6-6 and Figure 6-7 show the comparison of gel viscosities of water gels for shear rates ranging from 0 to 100 s^{-1}. From the curves, the water gel simulants can be described as pseudoplastic, shear-thinning material.

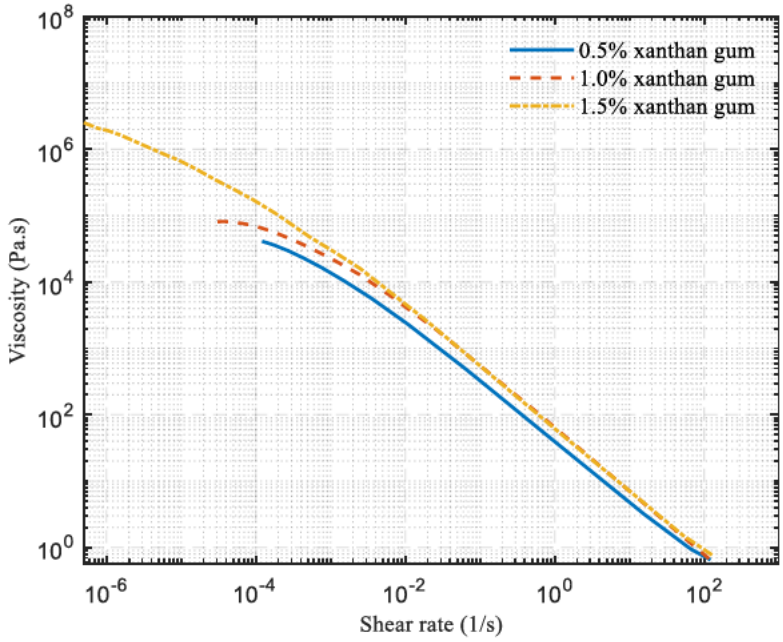

Figure 6-6: Shear rate versus viscosity for xanthan gum samples no: 1 – 3.

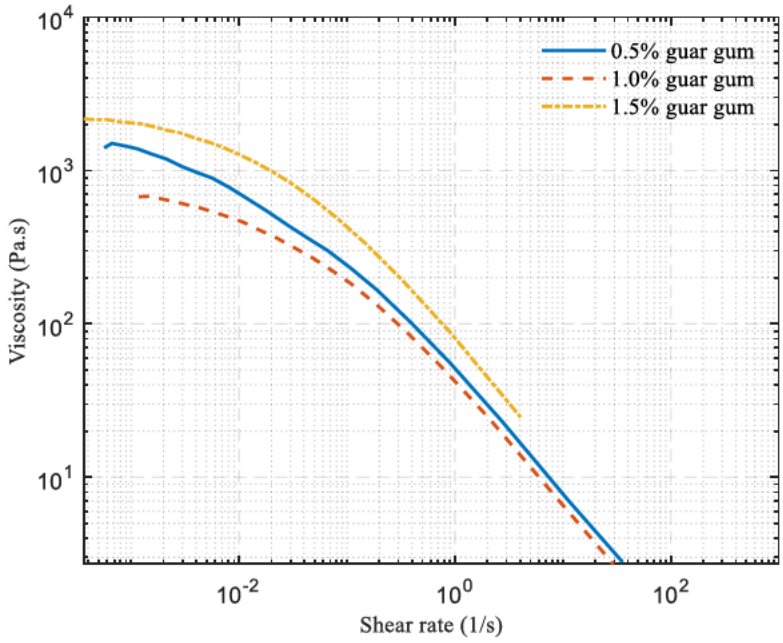

Figure 6-7: Shear rate versus viscosity for guar gum samples no: 4 – 6.

A best-fit mathematical model was fitted to the experimental data to determine the flow type of the samples. Since the gels are non-Newtonian, a non-linear model was used to describe the viscosity as a function of shear rate. The Williamson model was used in this study to characterise the gels. This model described in one-dimensional form by Equation (6-2), was fitted to the shear rate versus viscosity curves shown in Appendix D. The Williamson model was used because the experimental data was generated at low shear rates where the power law model fails to describe the material behaviour.

$$\eta = \frac{\eta_0}{(1 + K\dot{\gamma}^n)} \tag{6-2}$$

In the above η is the apparent viscosity and η_0 is the zero-shear viscosity. The rheological parameters obtained from the Williamson best-fit model are given in Table 6-3. The parameters were obtained for a range of shear rates described in the range column of Table 6-3. The gelling agent concentration does not significantly affect the rate index n for the gel simulants used. From the rheological results, it can be concluded that the simulants used are shear-thinning. They have a rate index value of less than 1 ($n < 1$). The influence of concentration on the consistency of the gel is also not significant as the concentration increases. However, it is notable that it is dependent on the shear rate range.

Table 6-3: Rheological parameters obtained from Williamson best-fit model.

Gel simulant	**Zero-rate viscosity(a) [Pa·s]**	**Consistency (b) [s]**	**Rate index [n]**	**Standard error**	**Range [1/s]**	**Flow type**
x0.5	16040	15.78	0.8976	5.553	[0.0100-120]	Shear thinning
x1.0	28660	14.96	0.9379	8.414	[0.0100-120]	Shear thinning
x1.5	3.45E+05	14.1	0.909	6.209	[0.0001-140]	Shear thinning
g0.5	535.6	13.09	0.8422	4.662	[0.1000-50]	Shear thinning
g1.0	587	15.44	0.8484	5.158	[0.1000-50]	Shear thinning
g1.5	908.8	14.1	0.8916	3.624	[0.1000-10]	Shear thinning

The estimated values of *n* increased as the concentration of gelling agent increased which shows a decrease in non-Newtonian behaviour of the fluid. The rate index of each simulant type does not vary significantly, however, the consistency of the gel increases with increasing concentration. The increase may be due to the non-uniform distribution of gelling agent during mixing and the flow of gelled simulant during testing.

7. SPRAY SHEET RESULTS AND DISCUSSION

This section presents data obtained from spray sheets of gelled propellant simulants generated by like-on-like doublet impinging jets. The spray sheets at the impinging point of the jets were observed using a high-speed camera. The photographic images were obtained at different injection pressures and represent the primary outcome of this study.

The injection pressure of the simulants was regulated between 1.4 and 14.0 bar and injected into an ambient field. The injection pressure versus time graphs of the simulants with different concentrations are given in Appendix E.

Flow visualisation was carried out for three different cases given in Table 7-1 namely low injection pressure range, medium injection pressure range, and high injection pressure range. The left, middle, and right part of Figures 7-2 to 7-13 correspond to case 1, 2, and 3, respectively. In these cases, two simulant types were investigated at three impinging angles. To characterise the flow, dimensionless numbers were used. Here the Reynolds number was calculated using the values of *K* and *n* obtained from the rheological characterisation results. The generalised Reynolds number for HBE was used with the assumption that $\tau_0 = 0$ and $\eta_\infty = 0$.

Table 7-1: Experiment conditions for the cases investigated.

Case	**Injection Pressure**	**Fluid velocity [m/s]**	**$Re_{gen,\ PL}$**
1	[1.4 - 5]	[10.4 - 19.0]	[2.02 - 8.52]
2	[6 - 10]	[20.8 - 26.8]	[4.30 -12.70]
3	[11 - 14]	[28.1 - 31.7]	[5.99 - 15.42]

Parameters were measured from the images using MATLAB®. The procedure for measurements by image processing is presented in Figure 7-1. Initially, an image was extracted from the highspeed video footage, and then converted into a 8-bit grayscale image with one channel (mxnx1). The grayscale image was then binarised using Ostu's method (Kothawala, 2023). Ostu's method is a MATLAB® built-in function that automatically chooses a threshold to minimise the variance of the black and white pixels. Lastly, multiple regions of interest containing ligaments and droplets were created and analysed.

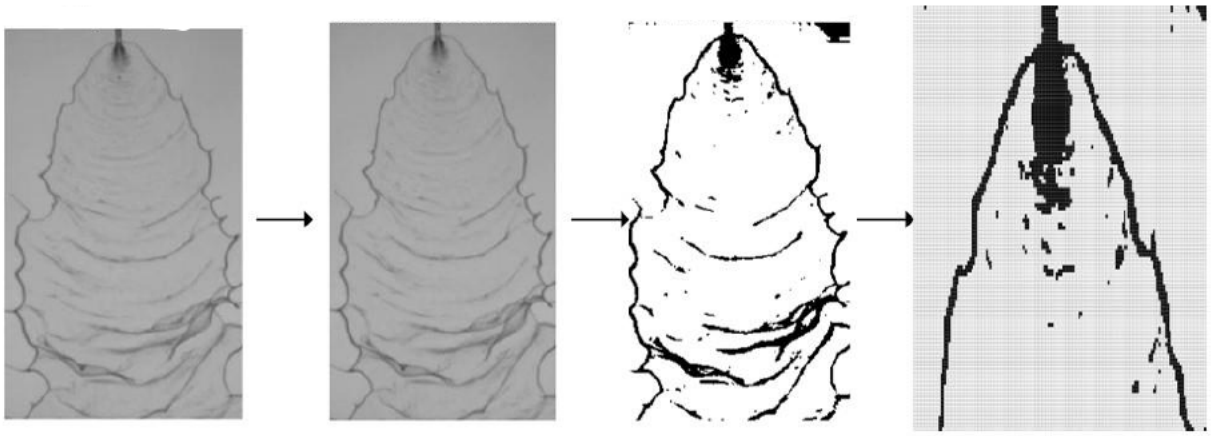

Figure 7-1: Procedure for measurement by image processing

7.1 Spray Sheet

The breakup of spray sheets for simulants used in this study using the injection element described in Section 3.2.2 and the experimental setup described in Chapter 5 led to various morphologies of breakup structures. The description of features observed on the spray sheet were named after studies done by Manisha et al. (2021) to validate the impinging device. The morphologies of breakup structures observed were used to classify the breakup regime at the specified operating conditions.

7.1.1 Morphology of 0.5 wt% xanthan gum simulant

Images of the spray sheets of a 0.5 wt% xanthan gum simulant are presented in this section. Observed features are indicated in the figures. Spray sheets generated at an impinging angle of 45° are presented in Figure 7-2. Morphology label descriptions for the spray sheets presented are as follows:

1. Surface wave
2. Unstable wavy rim
3. Fishbone structure
4. Ligaments generated from impact waves
5. Tangled web

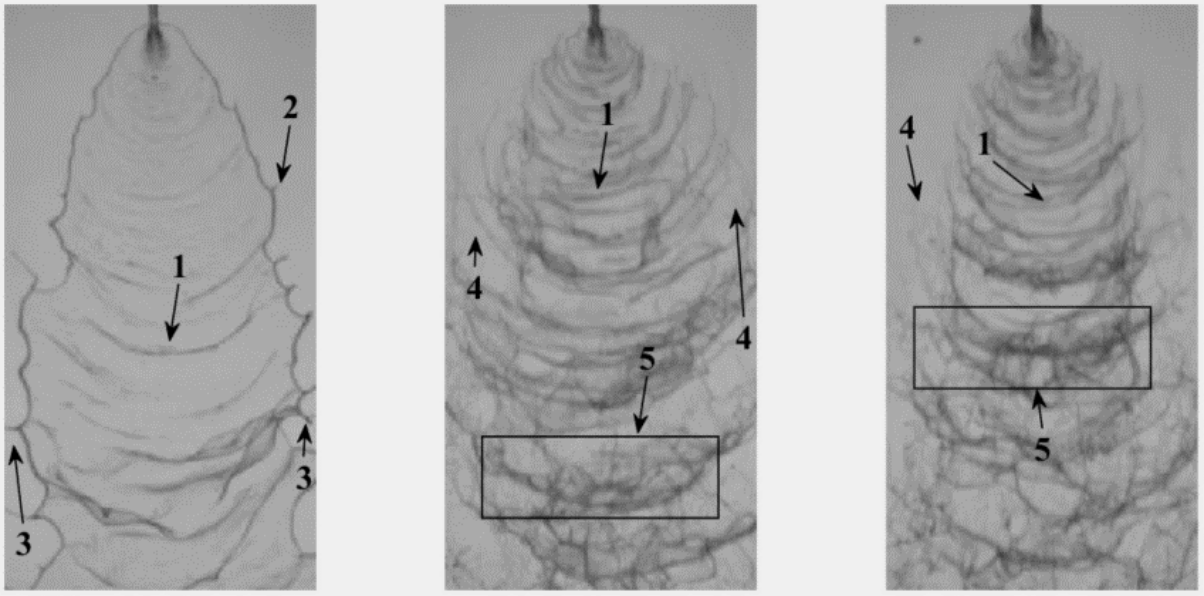

Figure 7-2: Spray sheets of 0.5 wt% xanthan gum simulant injected at 45º.

Spray sheets generated at an impinging angle of 60º are presented in Figure 7-3. Morphology label descriptions for the spray sheets are as follows:

1. Impact waves
2. Ligaments generated from impact wave
3. Irregular breakup structures
4. Web of ligaments

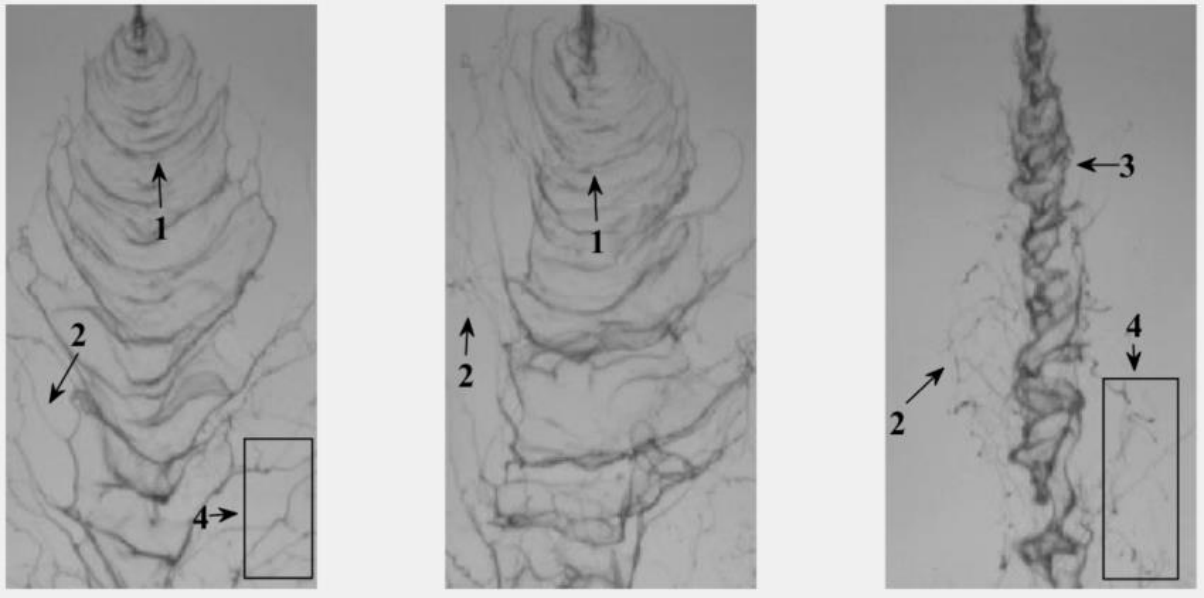

Figure 7-3: Spray sheets of 0.5 wt% xanthan gum simulant injected at 60º.

Spray sheets generated at an impinging angle of 90º are presented in Figure 7-4. Morphology label descriptions for the spray sheets are as follows:

1. Impact surface waves
2. Ligaments generated from impact waves
3. Web of ligaments
4. Tangled web

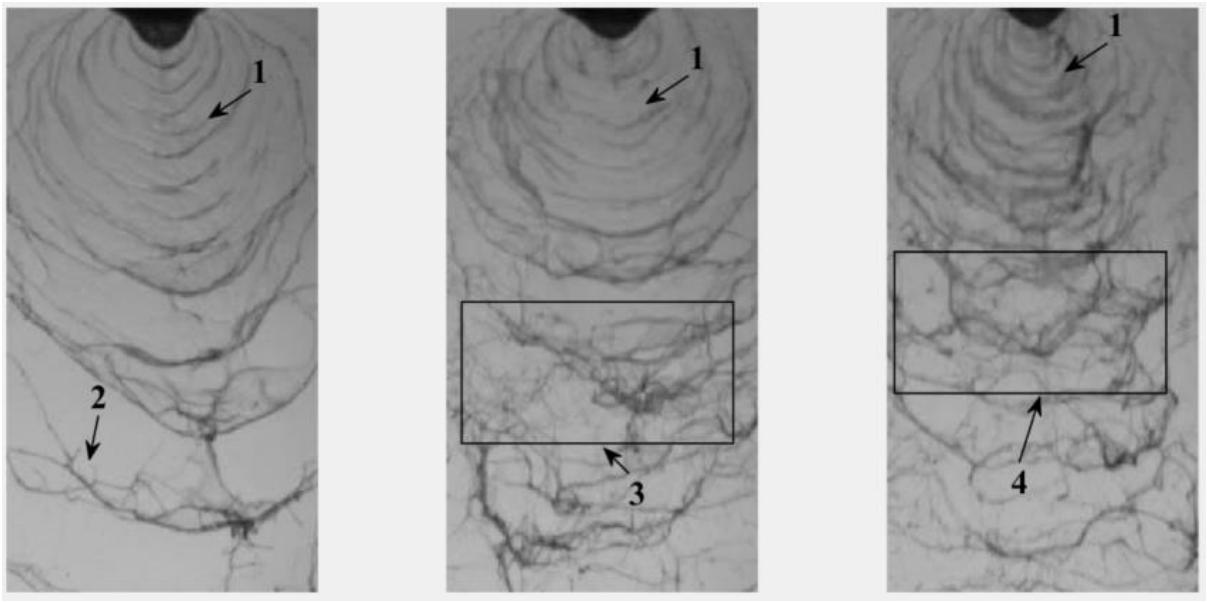

Figure 7-4: Spray sheets of 0.5 wt% xanthan gum simulant injected at 90º.

7.1.2 Morphology of 1.5 wt% xanthan gum simulant

This section provides visual representations of the spray sheets produced by a simulant containing xanthan gum at a concentration of 1.5 wt%. As in the previous section observed features are indicated in the figures with a description of each indicator. Spray sheets generated at an impinging angle of 45º are presented in Figure 7-5. Morphology label descriptions for the spray sheets are as follows:

1. Impact surface wave
2. Unstable wavy rim
3. Fishbone structure
4. Fishbone pattern
5. Long fishbone pattern
6. Web of ligaments

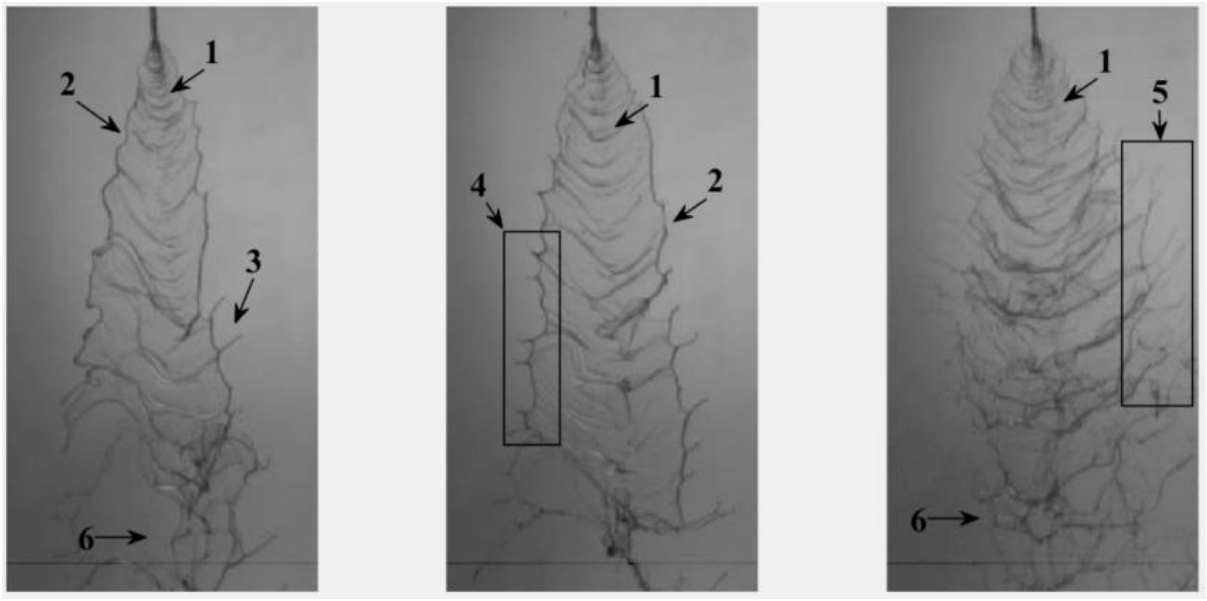

Figure 7-5: Spray sheets of 1.5 wt% xanthan gum simulant injected at 45º.

Spray sheets generated at an impinging angle of 60º are presented in Figure 7-6. Morphology label descriptions for the spray sheets are as follows:

1. Impact surface wave
2. Unstable rim
3. Tangled web of ligaments
4. Web of ligaments generated from impact waves

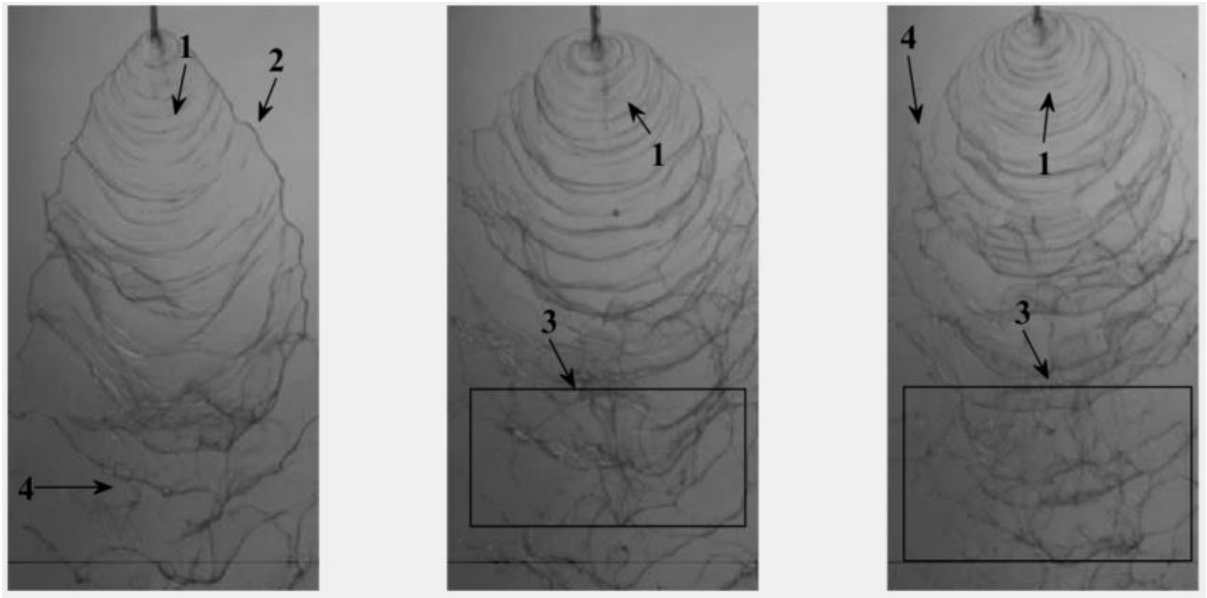

Figure 7-6: Spray sheets of 1.5 wt% xanthan gum simulant injected at 60º.

Spray sheets generated at an impinging angle of 90º are presented in Figure 7-7. Morphology label descriptions for the spray sheets are as follows:

1. Impact surface wave
2. Web of ligaments

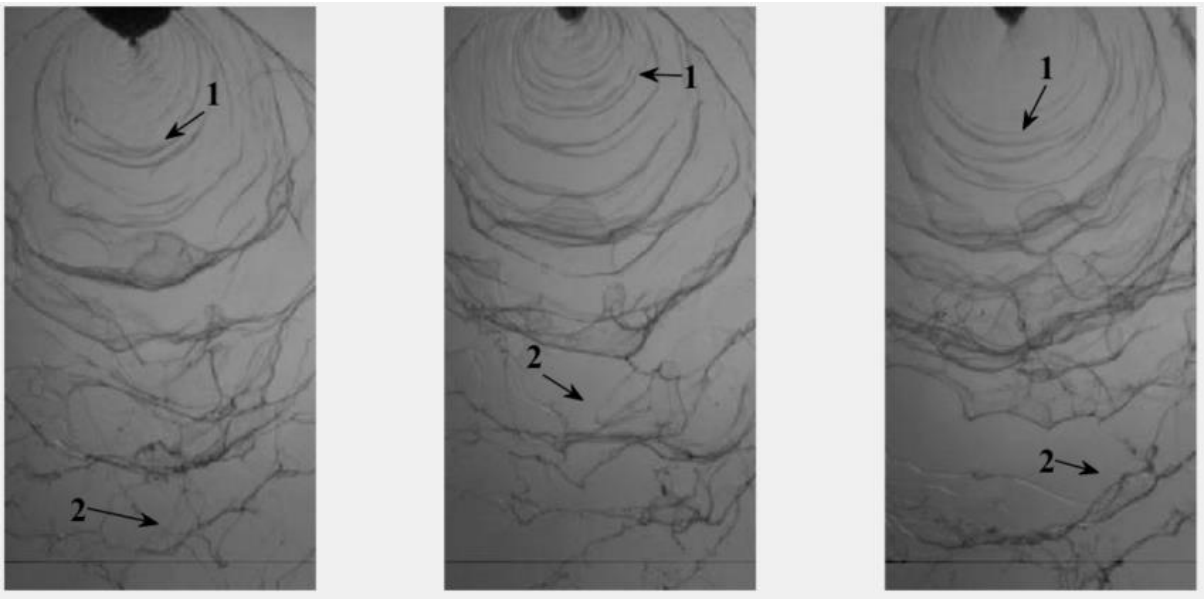

Figure 7-7: Spray sheets of 1.5 wt% xanthan gum simulant injected at 90º.

7.1.3 Morphology of 0.5 wt% guar gum simulant

This section displays visuals capturing the spray sheet of a simulant containing 0.5 wt% guar gum. Within the figures, the features observed are highlighted, accompanied by a description of each identified feature. Figure 7-8 showcases the spray sheets generated at an impinging angle of 45º. The morphology label descriptions assigned to these spray sheets are as follows:

1. Impact surface wave
2. Unstable wavy rim
3. Tangled ligaments
4. Web of ligaments
5. Ligaments generated from impact wave

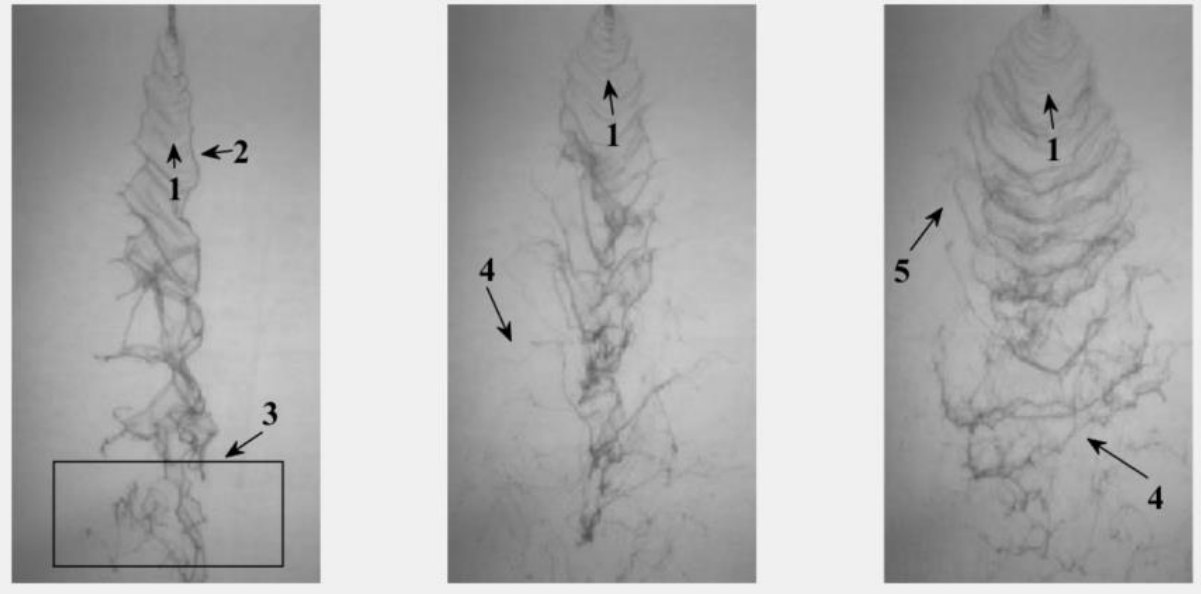

Figure 7-8: Spray sheets of 0.5 wt% guar gum simulant injected at 45º.

Spray sheets generated at an impinging angle of 60º are presented in Figure 7-9. Morphology label descriptions for the spray sheets are as follows:

1. Impact surface wave
2. Unstable wavy rim
3. Fishbone structure
4. Fishbone pattern
5. Web of ligaments
6. Unstable converged jet

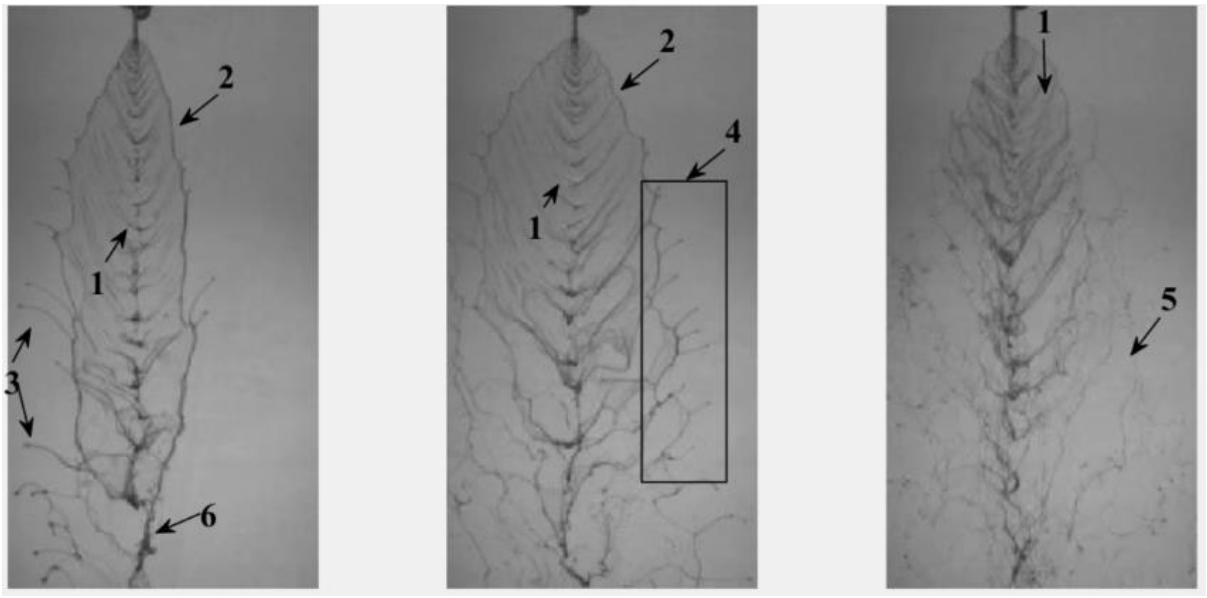

Figure 7-9: Spray sheets of 0.5 wt% guar gum simulant injected at 60º.

Spray sheets generated at an impinging angle of 90º are presented in Figure 7-10. Morphology label descriptions for the spray sheets are as follows:

1. Impact surface waves
2. Web of ligaments
3. Tangled ligaments

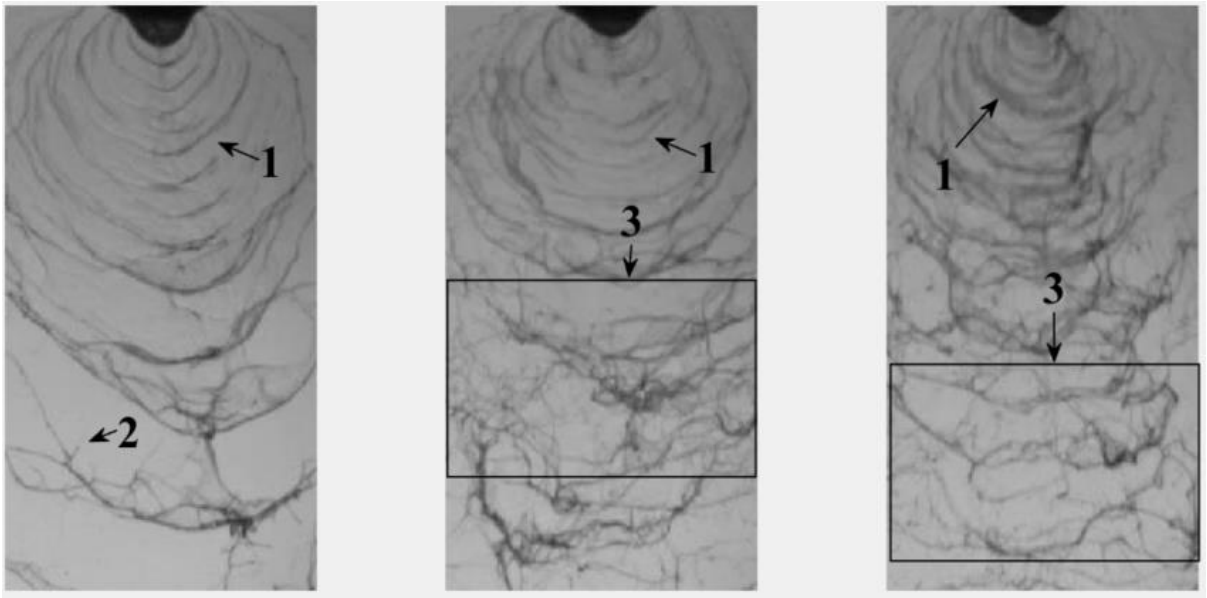

Figure 7-10: Spray sheets of 0.5 wt% guar gum simulant injected at 90º.

7.1.4 Morphology of 1.5 wt% guar gum simulant

In this section, visual illustrations of spray sheets generated by xanthan gum with a concentration of 1.5 wt% are depicted. Identified features are marked within the figures with a description. Figure 7-11

displays the spray sheets produced at an impinging angle of 45º. Morphology label descriptions for the spray sheets are as follows:

1. Smooth interior surface
2. Stable rim
3. Wavy rim
4. Surface wave

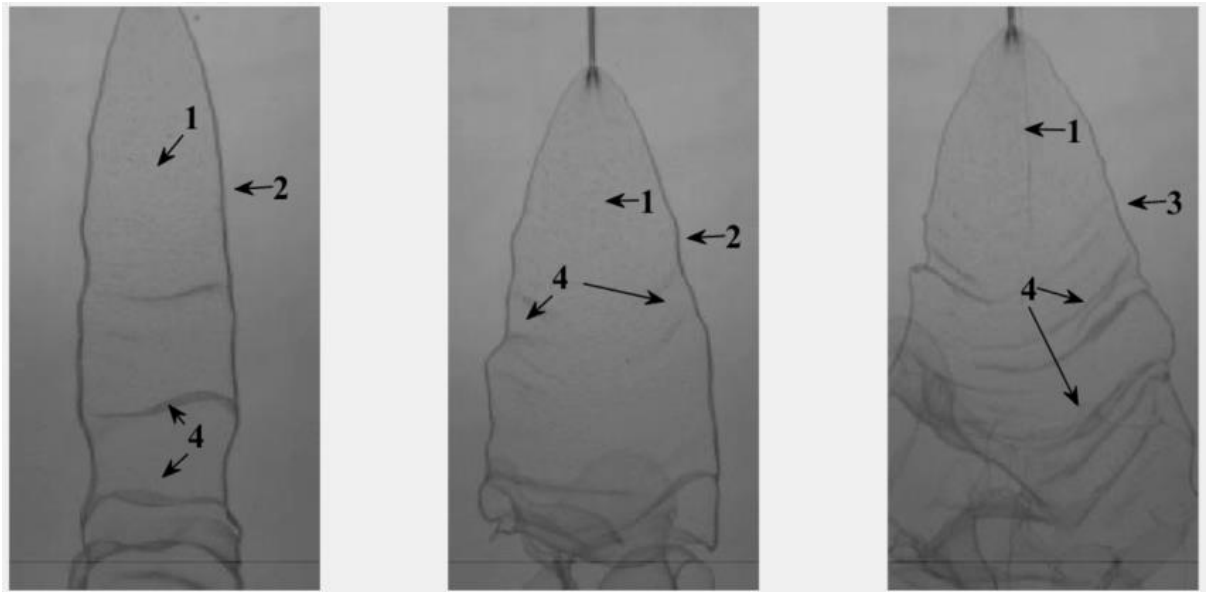

Figure 7-11: Spray sheets of 1.5 wt% guar gum simulant injected at 45º.

Spray sheets generated at an impinging angle of 60º are presented in Figure 7-12. Morphology label descriptions for the spray sheets are as follows:

1. Surface wave
2. Stable wavy rim
3. Impact surface waves
4. Tangled ligaments

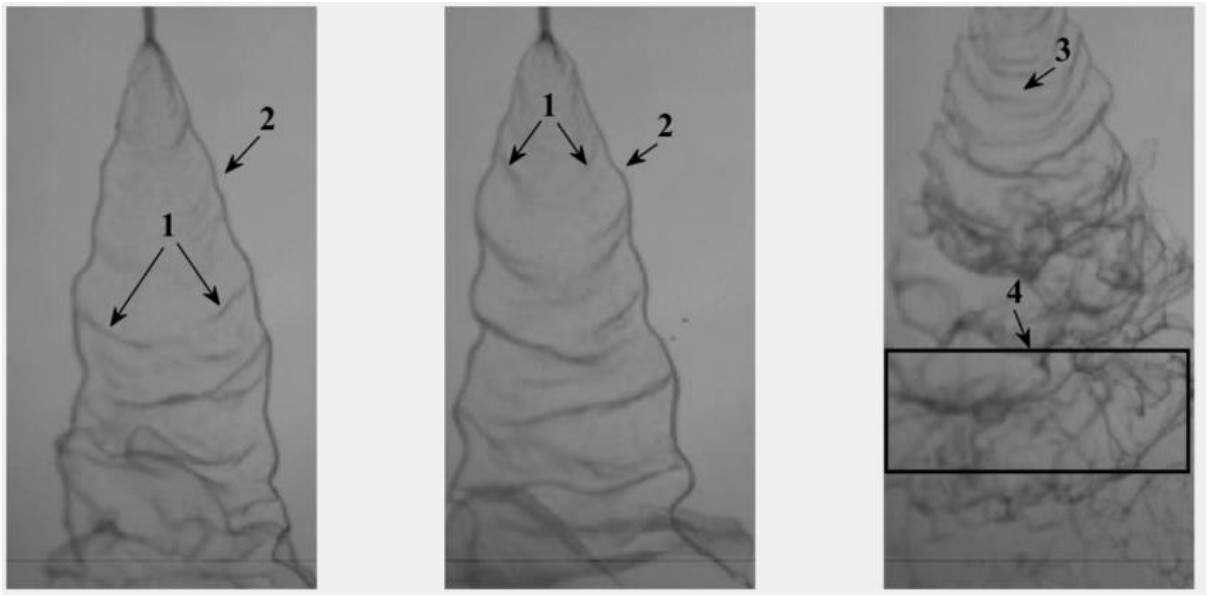

Figure 7-12: Spray sheets of 1.5 wt% guar gum simulant injected at 60º.

Spray sheets generated at an impinging angle of 90º are presented in Figure 7-13. Morphology label descriptions for the spray sheets are as follows:

1. Impact surface wave
2. Ligaments generated from impact waves
3. Droplets
4. A cluster of ligaments and droplets

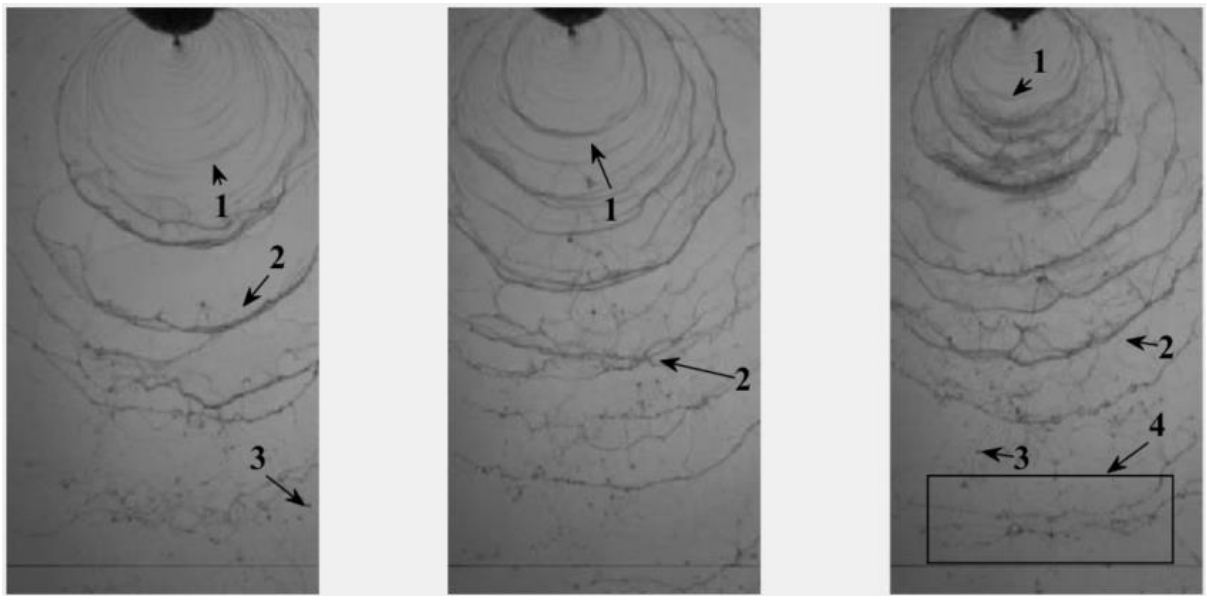

Figure 7-13: Spray sheets of 1.5 wt% guar gum simulant injected at 90º.

7.2 Breakup Regime

Breakup characteristics of the gels are named after the physical structure observed in visualisation. Similarly, to the work done by Manisha et al. (2021) and Jejurkar et al. (2018), breakup classifications were based on the presence of a rim at the periphery of the spray sheet.

7.2.1 Rimmed Sheets

Spray sheets involving rims were observed on simulants with low concentrations (0.5 wt%), for xanthan gum an unstable wavy rim was observed at low range injection pressures (4 – 6 bar) and impinging angle of 45º. This pattern is suggested by Ramasubramanian et al. (2015) at low jet velocities. For the same impinging angle of 45º, when the injection fluid velocity increases the rim becomes more unstable and fishbone structures were observed (Ramasubramanian, et al., 2015). These structures eventually developed into fishbone patterns of more or less symmetric distribution. This is the same pattern observed by Bremond and Villermaux (2006). The same unstable rimmed spray sheets were observed for guar gum simulants with a concentration of 0.5 wt%. For guar gum at an impinging angle of 45º, an unstable rim on the spray sheets was observed with an appearance of finger-like structures. Such structures and fishbone patterns were observed for an injection pressure of 7.5 bar. It was also observed that the spray sheets with unstable rims have holes that nucleate on the sheet and produce ligaments (Jejurkar, et al., 2018). This behaviour was shown in Figures 7-2 and 7-9 as the injection pressure increased.

Stable-rimmed spray sheets were observed for guar gum simulants with a concentration of 1.5 wt%. Figure 7-11 presents an illustration of these spray sheets. The sheets observed at low-range injection pressure have stable rims, and their surface is smooth near the impinging point. This pattern was observed by Ramasubramanian et al. (2015). However, it is noted that many other morphologies were observed depending on composition and other properties of the gel. At high jet momentum, relatively smooth interior surfaces were observed. The same features were observed for 1.5 wt% guar gum at a 60 degrees impinging angle. The only difference was that the rim in this case was wavy, and the sheet's interior was not smooth. In some cases, surface waves were induced, for example, in Figures 7-2 and 7-11 at 6 and 11 bar injection pressure, respectively, when the rim becomes unstable. Spray sheets of 1.5 wt% xanthan gum and 0.5 wt% guar gum in Figures 7-5 and 7-9 suggest that fishbone instability is a mechanism of atomisation when there is a rim at the periphery of the sheet (Padwal, et al., 2021).

7.2.2 Rimless Sheets

Spray sheet breakup involving rimless sheets were observed and are shown in Figures 7-3, 7-4, 7-7, 7-10, and 7-13. They were observed at all three pressure ranges at 90 degrees for a given gel simulant. At 90 degrees impinging angle, bow-shaped impact waves were observed. These waves were the main observed feature in these rimless sheets. Bow-shaped ligaments were generated and observed in these sheets when the liquid connecting two impact waves receded. The ligaments gradually break up into

smaller fragments, and in some cases, large droplets, while traveling downstream in the same bow shape configuration (Baek, et al., 2011). Figure 7-13 depicts this behaviour at an injection pressure of 11 bar with a cluster of fragmented ligaments and droplets observed downstream. It was also observed that for xanthan gum simulants, the resulting ligaments were continuous and created a web. In some cases, the webs were tangled. Most ligaments of the simulants did not breakup into droplets. The ligaments intermix with the droplets this pattern was also observed by Yang et al. (2013). Spray sheets at an impinging angle of 90 degrees have a larger spray cone. Large spray angles can cause a wide flame within a combustion chamber resulting in hotspots that could lead to material degradation. A wider spray angle could also increase thermal loads on the combustion chamber, which in turn, may require additional cooling to the combustion chamber walls.

7.3 Breakup Length

Grayscale images were sampled for each operating condition to determine the breakup length of the spray sheets generated. Figure 7-14 shows a sample of the grayscale image for a guar gum simulant injected at 5 bar of pressure at an impinging angle of 90 degrees. Grayscale scale images to determine the breakup length of other operating conditions are presented in Section 7.2 . From the sampled image, a vertical line shown in red in Figure 7-14 passing through the impinging point and extending downstream the spray sheet was drawn and measured to calculate the breakup length (Yang, et al., 2012). The pixel intensity value corresponds to the light intensity value (0-255) received by the camera lens from the backlit light source. These values were used to determine the spray sheet breakup length. An intensity value less than 255 downstream of the impinging point indicates the presence of a gel. An intensity value close to 255 corresponds to the background light. The distance from the impinging point to the region where the intensity values of the pixels correspond to the background was noted to be the breakup length of the spray sheet.

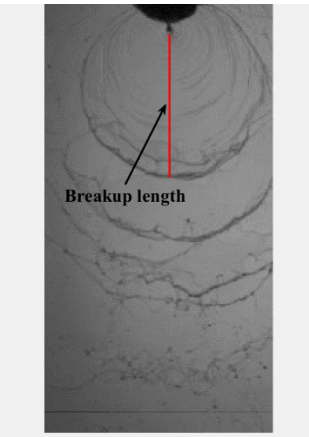

Figure 7-14: Breakup length of a guar gum simulant injected at 5 bar at an impinging angle of 90º.

Breakup lengths and uncertain estimates in Table 7-2 and Table 7-3 were obtained from the sampled images for the different operating conditions. In the case of xanthan gum, at an impinging angle of 60º there was no breakup. Similar observations were found for guar gum simulant of 1.5 wt% concentration at 45º and 60º impinging angles. In the case of xanthan gum, ligaments were observed from the periphery of the spray sheet.

Variations of breakup length with injection pressure are shown in Figures 7-15 to 7-18 for the investigated gelling agent concentrations. The results indicate that the breakup length decreases with increasing pressure drop for a given concentration. In some cases, for example for x0.5 at 45 degrees and g1.5 at 60 degrees there was no spray sheet breakup in the low and medium injection pressure ranges. This trend agrees with breakup length observations of water and Carbopol gel done by Baek et al. (2011). Trends with respect to concentration for xanthan gum show that the breakup length generally increases with increasing gelling agent concentration. Thus, the breakup is delayed suggesting that gels or injectors producing high concentration rimmed spray sheets are not ideal for rocket engine applications because highly effective atomisation is needed to improve propulsion performance. The opposite was observed for guar gum. Given that both gelling agents are similar, their different intermolecular interaction with the base liquid (water) is clearly different and leads to dissimilar breakup. This trend was also observed Mallory and Sojaka (2012) where they noted dissimilar breakup of the same gelling agents. The results show that the breakup lengths do not vary significantly for high injection pressures for different impinging angles. The atomisation performance of the gels is greatly influenced by viscosity meaning that the type of gelling agent used has a significant impact on the size of droplets in the spray. In this study, the spray sheets feature mainly ligaments which must still undergo breakup into droplets. This delayed breakup is because of the gel's viscosity and the process of ligament breakup into large droplets.

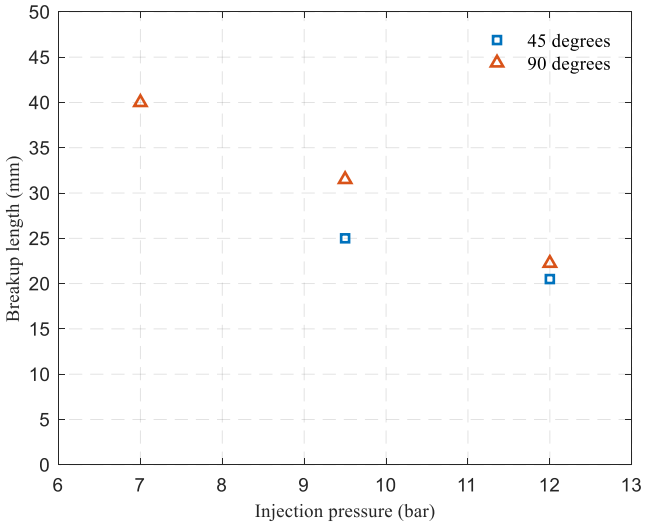

Figure 7-15: Graph of injection pressure versus breakup length for a 0.5 wt% xanthan gum simulant.

Table 7-2: Sheet breakup length extracted from grayscale images.

Simulant	Impinging angle [º]	Injection Pressure [bar]	Breakup length [mm]
x0.5	45	7	-
		9.5	25
		12	20.5
	60	6	-
		9	-
		12	-
	90	5	40
		7	31.5
		10.5	22.25
x1.5	45	5	55.5
		7	52.5
		10.5	29
	60	4.5	63.75
		7	41.5
		10.5	27.25
	90	5	38.5
		7	34
		10.5	33
g0.5	45	5	39.5
		7.5	34.5
		10.5	20.5
	60	5	46
		7.5	43.5
		11.5	27.75
	90	5	37.25
		8	23.25
		11	24.25
g1.5	45	4	-
		6.5	-
		11	-
	60	3.5	-
		7	-

Table 7-3: Sheet breakup length extracted from grayscale images continued.

Simulant	Impinging angle [°]	Injection Pressure [bar]	Breakup length [mm]
		11.5	17.5
	90	5	30.25
		7	39.25
		11	20

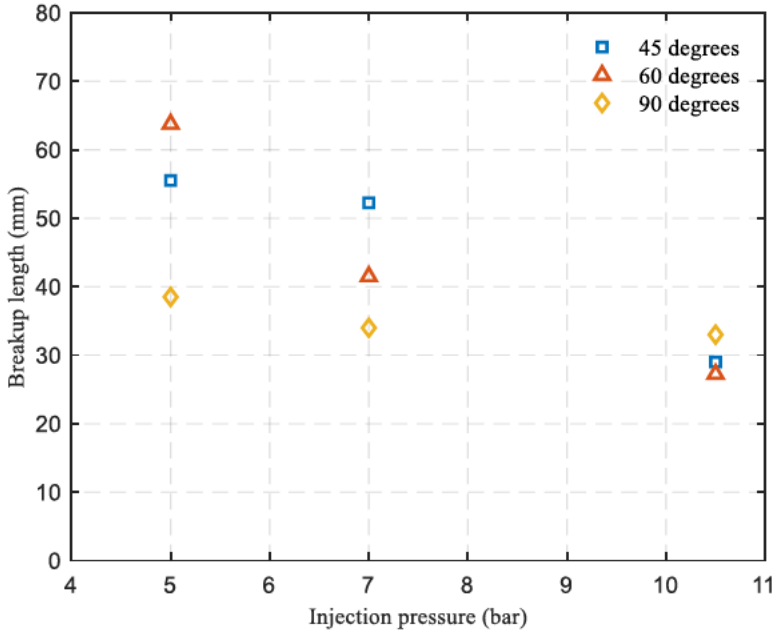

Figure 7-16: Graph of injection pressure versus breakup length for a 1.5 wt% xanthan gum simulant.

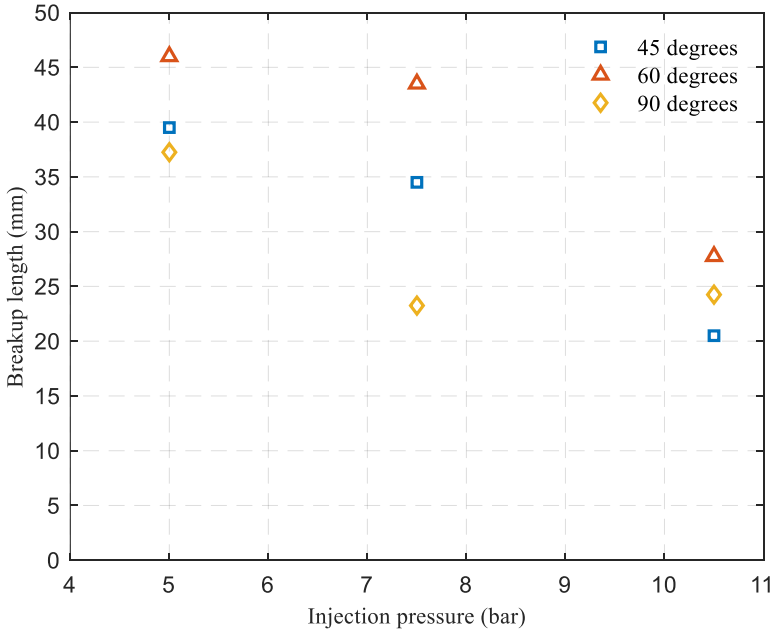

Figure 7-17: Graph of injection pressure versus breakup length for a 0.5 wt% guar gum simulant.

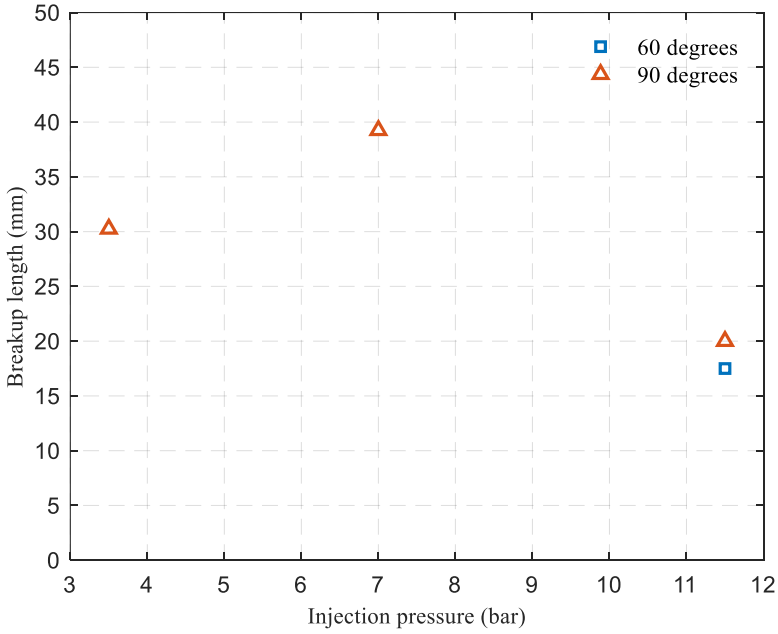

Figure 7-18: Graph of injection pressure versus breakup length for a 1.5 wt% guar gum simulant.

The experimental setup created a controlled environment to investigate the spray characteristics and behaviour of gel propellants. Examining the spray sheets allowed for the assessment of important parameters like spray angle, breakup length, and sheet breakup. Gaining insights into the behaviour of gel propellants during the spraying process facilitates the optimization of their formulation, combustion efficiency, and combustion stability. The outcomes of this work represents a stride forward in advancing the understanding and development of gel propellants.

8. CONCLUSION

The primary objective of this work was to design and build an injector test rig for characterising shear-thinning gel propellants. The data from the test rig will be used to develop rocket injectors utilising gel propellants.

The purpose of the test rig is to deliver gelled propellants from a pressurisation chamber to single injection elements for visualisation of the spray sheet generated. The designed test rig demonstrated effectiveness in generating spray sheets of gel simulants. This study described the developmental process of the test rig, capable of visualising the spray sheet generated by like-on-like doublet injection elements using a high-speed camera, including a predictive computational model to evaluate system performance under different set input parameters. The objectives of the study, as outlined in Chapter 1 were met as follows:

1. The injector test rig was designed and built.
2. A MATLAB® physical system model was developed to predict input parameters to achieve the required specific injection pressures.
3. Using two gel simulants, a high-speed camera visualised the spray sheets generated by the elements. Additionally, a qualitative and quantitative analysis of the spray sheet was done using image processing tools on MATLAB®.

The design phase of the test rig required a thorough understanding of the system requirements, test objectives, and anticipated operating conditions. A literature review of gelled propellants was performed to gain knowledge about gelled propellants and to form the foundation for developing a robust and adaptable test rig capable of generating spray sheets and capturing data. Through this process, water-based simulants were selected for utilisation on the test rig. Simulants were selected to demonstrate the test rig's capabilities and effectiveness. Additionally, they were selected because they are less costly, readily available, and minimise the risks associated with real propellants. This makes them safer to handle and work with in a lab test environment. Xanthan gum and guar gum were chosen as gelling agents to make the water-based simulants for testing on the rig. The formulation of these gel simulants involved careful blending of ingredients using a mechanical mixer to achieve a homogenous mixture. The gelling agents were combined with water in concentrations of 0.5% and 1.5% by weight to create gels with shear-thinning behaviour.

Rheological characterisation of these gels was done using an AR1500ex rotational rheometer. Shear stress and viscosity determination tests were done on the rheometer to quantify the formulated simulants' flow behaviour, power index, and consistency. By formulating these gel simulants and performing characterisation, it was possible to fit the Williamson model to the experimental data to verify that the gels showed shear-thinning flow behaviour. From characterising these gels, insights were

gained for studying gel behaviour which can play a vital role in the development of gel propulsion technology. In summary, the formulation and characterisation allowed the testing of a shear-thinning gel on the test rig and the spray sheet visualisation.

During the build phase, attention was given to the assembly and integration of various components. The construction adhered to the modular design philosophy used. The injector frame comprising manifold backplates, manifolds, manifold bracket, and injection elements were constructed separately. The same was also done for the simulant feed system. All components were then integrated onto the test rig's table frame, resulting in a test rig meeting all specifications. A modular design approach was followed to ensure ease of operation, maintenance, and changes of components. Furthermore, the injector frame module allowed for tests to be conducted at different impinging angles and the capability to change injector elements for studying elements with different sizes or geometries.

The test rig was able to maintain consistent operating pressures as shown from the injection pressure results in Appendix E. It allowed for comprehensive testing, including sprays sheet visualisation. The test rig employed a LabVIEW™ application to facilitate its operations. The test rig's flexible control system allowed for customisation to accommodate future testing requirements. Overall, the design and build of the test rig provided a solid foundation for testing gel propellants and spray sheet visualisation. The test rig will be an important platform for developing gel propulsion technology within ASRI.

The use of highspeed image acquisition allowed for analysis of the spray sheets generated by like-on-like doublet injection elements. Video footage was captured using a Chronos 1.4 highspeed camera. The images were examined using MATLAB® and the morphologies of the spray sheets were described. Impact waves and ligaments were the main observed features on the spray sheets under many operating conditions. The waves led to different instabilities that facilitated the breakup of sheets into ligaments and/or droplets. The breakup lengths at different impinging angles and injection pressures were characterised by observing the spray sheet. The spray sheet visualisation technique used in this study provided valuable data that can potentially be used to validate and calibrate CFD models. Overall, the test rig and spray sheet visualisation techniques provided a valuable platform for understanding the behaviour of gels and various spray systems in gel propellant rocket injectors.

Future work on the test rig is required for the injector elements frame. During testing, it was discovered that a lot of time was spent on adjusting the impinging angle. Further to this, difficulties were encountered with jet alignment once the elements were in place. Future work can focus on developing a system for changing impingement angles in a robust and repeatable way using stepper motors to rotate the manifold brackets on the backplates. This can help minimize setup time and get more precise adjustments by making angle changes using the motor's micro-stepping capabilities. This will potentially also mitigate jet misalignment issues to ensure accurate and repeatable results. This kind of system could also be used to store position history information and be used on the LabVIEW™

application to change between angles quickly. The present actuator, controlled by a hydraulic power pack can be fitted with a solenoid directional control valve to automate the controls, reducing human interaction with equipment. Further development on the frame rails is required to control the distance between injection elements. An additional inlet on the feedlines can be added for running water to the injection elements to verify jet alignment as well as aid in focusing the camera on the spray sheet.

Finally, the present image processing method of using MATLAB® image processing toolbox functions can be extended to work with functions to detect different features on the spray sheets.

REFERENCES

Arnold, R., Paulo, H., Santos. P. H. S., Kuba, T., Campanella, O. H., Anderson. W. E., 2009. *Investigation of Gelled JP-8 and RP-1 Fuels.* San Francisco, WCECS.

Arnold, R., Santos, P. H. S., Campanella, O. H., and Anderson, W.E., 2011. Rhelogical and Thermal Behavior of Gelled Hydrocarbon Fuels. *Journal of Propulsion and Power,* Volume 27, pp. 151-160.

Baek, C., and Kim, C., 2011. Rheological Properties of Carbopol Containing Nanoparticles. *Journal of Rheology,* Issue 55, pp. 313-329.

Baek, G., Kim, S., Han, J., and Kim, C., 2011. Atomization Characteristics of Impinging Jets of Gel Material Containing Nanoparticles. *Journal of non-Newtonian Fluid Mechanics,* pp. 1272-1285.

Barnes, H. A., and Walters, K., 1985. *SpringerLink.* [Online] Available at: https://doi.org/10.1007/BF01333960 [Accessed 24 October 2022].

Bremond, N., and Villermaux, E., 2006. Atomization by Jet Impact. *Journal of Fluid Mechanics,* Volume 549, pp. 273-306.

Bush, J., and Hasha, A., 2004. On Collision of Laminar Jets: Fluid Chains and Fishbones. *Journal of Fluid Mechanics,* Volume 511, pp. 285-310.

Calabro, M., 2011. Overview on Hybrid Propulsion. *Progress in Propulsion Physics,* pp. 354-374.

Chojnacki, K., and Feikema, D., 1994. *Atomization Studies of Gelled Liquids.* [Online] Available at: https://doi.org/10.2514/6.1994-2773 [Accessed 15 September 2022].

Chowdury, M. R., and Fester, V. G., 2012. Modeling Pressure Losses for Newtonian and Non-Newtonian Laminar and Turbulent Flow in Long Square Edged Orifices. *Chemical engineering Research and Design,* 90(7), pp. 863-869.

Ciezki, H. K., Kirchberger, C., Stiefel, A., Kröger, P., Caldas Pinto, P., Ramsel, J., Naumann, K. W., Hürttlen, J., Schaller, U., Imiolek, A., and Weiser, V., 2017. Overview on the German Gel Propulsion Technology Activities: Status 2017 and Outlook. Milan, *7th European Conference for Aeronautics and Space Sciences (EUCASS),* DOI: 10.13009/EUCASS2017-253

Ciezki, H., Robers, A., and Schneider, G., 2002. Investigation of the Spray of Gelled JET A-1 Fuels Using an Airblast and an Impinging Jet Atomizer. Indiana, *38th AIAA/ASME/SAE/ASEE joint Propulsion conference and Exhibit*.

Ciezki, H., Zhukov, V., Werling, L., Kirchberger, C., Naumann, C., Friess, M., Riedel U., 2019. Advanced Propellants for Space Propulsion – A Task within the DLR Interdisciplinary Project "Future Fuels". Madrid, *8th European Conference for Aeronautics and Space Science (EUCASS).*

Suslov, D., Hardi, J., and Oschwald, M., 2019., Full-Length Visualisation of Liquid Oxygen Disintegration in a Single Injector Sub-Scale Rocket Combuster. *Aerospace Science and Technology,* Issue 86, pp. 444-454. Elsevier. doi: 10.1016/j.ast.2018.12.027. ISSN 1270-9638.

Dombroski, N., and Johns, W. R., 1963. *ScienceDirect.* [Online] Available at: https://www.sciencedirect.com/science/article/pii/0009250963850058 [Accessed 14 October 2022].

Dzuy, N. Q., and Boger, D. V., 2000. *Journal of Rheology.* [Online] Available at: https://doi.org/10.1122/1.549709 [Accessed 24 October 2022].

Fallourd, M., and Viscione, L., 2009. *ScienceDirect.* [Online] Available at: https://doi.org/10.1533/9781845695569.1.3. [Accessed 11 April 2023].

Fu, Q.-f., and Yang, L.-j., 2015. Visualisation Studies of the Spray From Swirl Injectors Under Elevated Ambient Pressure. *Aerospace Science and Technology,* Issue 47, pp. 154-163.

Fu, Q.-f., Duan, R.-z., Cui, K.-d., and Yang, L.-j., 2014. Spray of Gelled Propellants From an Impinging-Jet Injector Under Different Temperatures. *Aerospace Science and technology,* Volume 39, pp. 552-558.

Fu, Q.-f., Yang, L.-j., Cui, K.-d., and Zhuang, F.-c., 2014. Effects of Orifice Geometry on Gelled Propellants Sprayed From Impinging-Jet Injectors. *Journal of Propulsion and Power,* 30(4), pp. 1113-1117.

Ghafourian, A., Mahalingam, S., Dindi, H., and Daily, J. W., 1991. *A Review of Atomisation in Liquid Rocket Engines.* Nevada, *American Institute of Aeronautics and Astronautics*.

Glushkov, D., Paushkina, K., and Pleshko, A., 2022. Gel Fuels: Preparing, Rheology, Atomization, Combustion. *Energies*,16(1). [Online] Available at: https://doi.org/10.3390/en16010298

Green, J., Rapp, D., and Roncace, J., 1991. Flow Visualisation of Rocket Injector Spray Using Gelled Propellant Simulants. Sacramento, CA, *American Institute of Aeronautics and Astronautics*.

Guan, H.-s., Li, G.-X., and Zhang, N.-y., 2018. Experimental Investigation of Atomisation Characteristics of Swirling Spray by ADN Gelled Propellant. *Acta Astronautica,* Issue 144, pp. 119-125.

Gupta, H., and Roy, S., 2007. Chapter 6 - Assessment And Exploitation. *Geothermal Energy,* pp. 121-164.

Haddad, A., Natan, B., and Arieli, R., 2012. *The European Conference for Aerospace Sciences.* [Online] Available at: https://doi.org/10.1051/eucass/201102499 [Accessed 17 October 2022].

Hodge, K., Crofoot, T., and Nelson, S., 1999. Gelled Propellants for Tactical Missile Applications. Los Angeles, California, *American Institute of Aeronautics and Astronautics*.

Huzel, D. K., and Huang, D. H., 1992. Modern Engineering for Design of Liquid Propellant Rocket Engines. s.l.:*American Institute of Aeronautics and Astronautics*.

Jejurkar, S., Yadav, G., and Mishra, 2018. Visualization of Sheet Breakup of Non-Newtonian Gels Loaded With Nanoparticles. *International Journal of Multiphase Flow*, pp. 57-76.

Jung, K., Khil, T., and Yoon, Y., 2006. Effects of Orifice Internal Flow on Breakup Characteristics of Like-Doublet Injectors. *Journal of Propulsion and Power*, 22(3), pp. 653-660.

Kampen, J. V., Alberio, F., and Ciezki, H., 2006. *ScienceDirect.* [Online] Available at: http://www.elsvier.com/locate/aescte [Accessed 15 June 2022].

Kar, M., Chaourasiya, Y., Maheshwari, R., and Tekade, R., 2019. *Science Direct.* [Online] Available at: https://doi.org/10.1016/B978-0-12-817909-3.00002-9. [Accessed 30 May 2022].

Khahledi, M., Haldenwang, R., Chhabra, R., and Fester, V., 2020. Non-Newtonian Fluid Flow From Bottom of Tank Using Orificies of Different Shapes. *Chemical Engineering Research and Design*, I(57), pp. 34-35.

Kull, H.J., 1991. *Science Direct* .[Online] Available at: https://www.sciencedirect.com/science/article/pii/037015739190153D [Accessed 8 October 2022].

Leask, S.B., and MacDonell, V.G., 2017. *Academia.* [Online] Available at: https://www.academia.edu/78997089/The_Effect_of_Doublet_Injector_Orifice_Geometry_on_Spray_Characteristics [Accessed 18 October 2022].

Long, C.G., 1962. Reinforced Gelled Propellants. United States of America, Patent No. 796.169.

Lozano, A., Barreras, F., Hauke, G., and Dopazo, C., 2001. Longitudinal Instabilites in An Air-blasted Liquid Sheet. *Journal of Fluid Mechanics*, Issue 437, pp. 143-173.

Ma, D.-J., Chen, X.-D., Khare, P., and Yang, V., 2011. Atomization Patterns and Breakup characteristics of Liquid Sheets Formed by two Impinging Jets. Florida, *American Institute of Aeronautics and Astronautics*.

Mallory, J. A., and Sojaka, P. E., 2012. A Study of Gelled Propellant Simulants Using Impinging Jet Injectors. Heidelberg, *12th Triennial International Conference on Liquid Atomization and Spray Systems (ICLASS)*.

Mallory, J., Defini, S., and Sojak, P., 2010. Formulation of Gelled Propellant Simulants. Nashville, *American Institute of Aeronautics and Astronautics*.

Natan, B., and Rahimi, S., 2000. Thixotropic Effect of Inorganic Gel Fuels. *Journal of Propulsion and Power*, 16(6), pp. 1182-1184.

Natan, B., and Rahimi, S., 2002. The Status of Gel Propellants In Year 2000. *Intermational Journal of Energeyic Materials and Chemical Propulsion.*

Natan, B., Perteghella, V., and Solomon, Y., 2010. *Scinapse.* [Online] Available at: https://doi.org/10.2514/6.2010-7144 [Accessed 15 September 2022].

Negeed, E.-S. R., Hidaka, S., Kohno, M., and Takata, Y., 2011. Experimental and Analytical Investigation of Liquid Sheet Breakup Characteristics. *International Journal of heat and fluid flow,* Issue 32, pp. 95-106.

Nikvash, K., and Nekoufar, K., 2015. Analysis of Differen Types of Liquid Fuel Injectors With Critical Approach, s.l.: *Visi journal Akademik*.

Notaro, V., Khare, P., and Lee, J., 2019. Mixing Characteristics of Non-Newtonian Impinging Jets at Elevated Pressures. *Flow Turbulence and Combustion,* 102(2), pp. 355-372.

Oberg, E., Jones, F. D., Horton, H. L., and Ryffel, H., 2012. *Machnery's Handbook.* 29th ed. New York: Industrial Press.

Padwal, M. B., and Mishra, D. P., 2013. Synthesis of Jet A-1 Gel Fuel and its Characterization for Propulsion Applications. *Fuel Processing Technology,* Issue 106, pp. 359-365.

Padwal, M. B., and Mishra, D. P., 2016. Interactions Among Synthesis, Rheology, and Atomization of a Gelled Propellant, *Berlin Heidelberg: Springer-Verlag.*

Padwal, M. B., Benveniste, N., and Mishra, D. P., 2021. Gel Propellants. *Progress in Energy and Comnustion Science*, Volume 83.

Park, J., Huh, k., and Li, X., 2004. Experimental Investigation on Cellular Breakup of a Planar Liquid Sheet From an Air-blast Nozzle. *Physics of Fluids,* March. Issue 16.

Priyesh, S., and Tiegang, F., 2014. *SpringerLink.* [Online] Available at: https://doi.org/10.1007/s00348-014-1666-z [Accessed 4 October 2022].

Rahimi, S. et al., 2001. Preparation and Characterization of Gel Propellants and Simulants. Salt Lake City, Utah, *American Institute of Aeronautics and Astronautics*.

Rahimi, S., and Natan, B., 1998. Atomization Characteristics of Gel Fuels, Haifa, Israel: *American Institute of Aeronautics and Astronautics*.

Rahimi, S., and Natan, B., 2000. Flow of Gel Fuels in Tapered Injectors. *Journal of Propulsion and Power,* 16(3), pp. 458-464.

Rahimi, S., Peretz, A., and Natan, B., 2007. On Shear Rheology of Gel Propellants. Haifa, Wiley-VCH.

Ramasubramanian, C., Notaro, V., and Lee, J. G., 2015. Characterization of Near-Field Spray of Nongelled- and Gelled-Impinging Doublets at High Pressure. *Journal of Propulsion and Power.*

Rapial, A. S., and Daney, D. E., 1969. Preparation and Characterization of Slush Hydrogen and Nitrogen Gels, Colorado: *National Bureau of Standards*.

Rapp, D., and Zurawski, R., 1988. Characterization of Aluminum/RP-1 Gel Propellant Properties. Boston, Massachusetts, *24th Joint Propulsion conference*.

Rietz, R. D., and Bracco, F. V., 1982. *Researchgate.* [Online] Available at: http://dx.doi.org/10.1063/1.863650 [Accessed 06 October 2022].

Santos, P. et al., 2010. *ResearchGate.* [Online] Available at: https://www.researchgate.net/publication/41668037_Characterization_of_JP-8SiO2_and_RP-1SiO2_Gels [Accessed 15 July 2022].

Song, W., Hwang, J., and Koo, J., 2021. Atomization of Gelled Kerosene by Multi-Hole Pintle Injector for Rocket Engines. *Fuel*, Issue 285, pp. 1-12.

Tarpely Jr, W. B., 1969. Thixotropic Liquid Propellant Composition With Solid Storage Charateristics. United States of America, Patent No. 3,470,040.

Teoman, B., Potanin, A., and Armenante, P., 2022. The Discharge of Complex Fluids Through an Orifice: A Review. *Chemical Engineering Research and Design*, Issue 179, pp. 346-364.

Terech, P., and Weiss, R., 1997. Low Molecular Mass Gelators of Organic Liquids and the Properties of Their Gels, Washington DC, *American Chemical Society*.

Varghese, T., Gaindhar, S. C., David, J., Jose, J., 1995. Development Studies on Metallised UDMH and Kerosene Gels. *Defence Science Journal*, Volume 45, pp. 25-30.

Wahono, S., Honnery, D., Soria, J., and Ghojel, J., 2007. High-speed Visualisation of Primary Break-up of an Annular Liquid Sheet. *Springer-Verlag*, Issue 44, pp. 451-459.

Wooseok, S., Juhyun, H., and Jaye, K., 2021. Atomisation of Gelled Kerosene by Mutli-hole Pintle Injector for Rocket Engines. *Fuel*, Volume 285, pp. 1-9.

Yang, L.-J., Fu, Q.-f., Qu, Y.-y., Gu, B., Zhang, M.-z., 2012. Breakup of a Power-law Liquid Sheet Formed by an Impinging Injector. *International Journal of Multiphase flow*, Issue 39, pp. 37-44.

Yang, L.-j., Fu, Q.-f., Zhang, W., Du, M.-l., Tong, M.-x., 2013. Spray Characteristics of Gelled Propellants in Novel Impinging Jet Injector. *Journal of Propulsion and Power*, pp. 104-113.

Yoon, C., Heister, S., Xia, G., and Merkle, C., 2010. Simulation of Injection of Shear-thinning Gel Propellants Through Plain-orifice Atomizer. Nashville, *American Institute of Aeronautics and Astronautics*.

Appendix A: Closed Tank Design Calculations

This section presents the design calculation for the closed tank given in the ASME boiler and pressure vessel design codes section VIII UG-27.

Equations (A-1) and (A-2) are pressure equations based on the circumferential and longitudinal stresses, respectively.

$$P = \frac{SEt}{R + 0.6t} \tag{A-1}$$

$$P = \frac{2SEt}{R - 0.4t} \tag{A-2}$$

In the equations above, *S*, is the maximum allowable stress, *E*, is the joint efficiency, *R*, is the inside radius of the shell, and, *t*, is the minimum required thickness of the shell.

The vessel's design pressure was 10 bar, incorporating a 25% margin above the operational pressure. The vessel's design pressure was decided on after considering the use case of the test stand and the vessel itself. The highest pressure level the vessel can be exposed to is 15 bar to ensure the system can safely operate under normal conditions. This design pressure was also selected because it aligns with the operational requirements of the system. The tank ends were designed following the ASME BPVC section VIII, division 1, UG-34(c) design codes. The minimum thickness required for the flat ends was calculated using Equation (A-3) .

$$t = d\sqrt{\frac{CP}{SE}} \tag{A-3}$$

In this equation, *C* is a factor depending upon the attachment method, *d* is the diameter, *E* is the joint efficiency, *P* is the design pressure, and, *S* is the maximum allowable stress in tension. Flat face weld on slip flanges and bolt-on blind flanges were chosen for the tank ends with a calculated minimum thickness of 7.74 mm. A thickness of 15 mm was chosen for the end blind flanges to have sufficient thread engagement with pipe fittings on both ends of the tank.

An analysis of a fillet weld in shear was done to determine the strength of the weld or how much load it can handle before it fails. The material thickness of the parts welded together was estimated to be between 12 mm and 20 mm. Therefore, a weld size of 6 mm was considered. The load in the vessel causes shear stress on the weld, so the load-carrying capacity of a weld of this specified size needed to be calculated. When a weld is in shear, the tensile strength of the filler material cannot be used to calculate the load-carrying capacity of the weld. Instead, the tensile strength is reduced by a factor to ensure safety. In this analysis, the welding wire (ER4043) properties used in calculations is the ultimate

tensile strength of 200 MPa. A reduction of 0.7 was used for welds in tensile stress. After applying this safety factor, the shear force the weld can carry was calculated to be 136171.567 N using Equation (A-4) . This shear force corresponds to a pressure of 75.74 bar in the vessel.

$$F_{shear} = 0.707hl\tau \quad \text{(A-4)}$$

Here h, is the size of the weld, l is the length of the weld, and τ is the allowable stress.The total force permitted on the end covers was calculated to be 26968.64 N at the maximum allowable working pressure of the vessel of 15 bar. This permitted end cover force meant that the weld beads load carrying capacity for the specified weld size was sufficient to hold the maximum pressure the tank could be subjected to.

The pressure system being analysed is fabricated from aluminium with stainless steel fittings. Galvanic corrosion was considered to evaluate the possibility of leakage between the end covers and fittings due to galvanic corrosion. In this case, galvanic corrosion was not of great concern because it was not likely for corrosion to take place in the environment of operation. The surface area of aluminium material is large compared to the surface area of stainless steel (fittings), which has a low risk of significant corrosion.

Although corrosion was ruled out as a failure path for the vessel, another failure path considered was bolt yielding. Bolt-on blind flanges were proposed and were bolted onto the slip-on flanges welded to the shell, and in the event of an over-pressurisation, the bolts will begin to elongate and eventually fail. Standard bolt calculations were done to determine an appropriate bolt size for the end covers. Bolt yielding was also deemed the acceptable failure path of the vessel as opposed to weld bead failure. This failure mode was decided on for the reason that if the weld fails, the blind and slip-on flange assembly will be ejected and this could cause serious injuries and damage. In the case of bolt yielding, the bolts elongate, and the clamping force between the blind flange and the slip-on flange welded to the cylindrical shell is zero, therefore, allowing the gas to escape the vessel and depressurising the system.

Standard bolt calculations were done to size an appropriate bolt and meet failure path requirements. The calculations were based on a typical through-bolted joint consisting of a bolt, two washers, two clamped members, and a nut. The maximum load on the bolts was calculated to be 26968.64 N based on the maximum allowable working pressure of the vessel. Each blind flange had 8 bolts to carry this load. This load is distributed to each bolt resulting in a force of 3371.08 N on each bolt. A bolted joint with a preload must meet the following three requirements.

1. The bolt must have adequate strength to withstand the external loads.
2. A separation factor of safety must be incorporated at the limit load.
3. The bolt must have adequate fracture and fatigue life.

A separation safety factor of 2 was applied to the external load, resulting in a load of 6742.06 N on each bolt. The flanged joint being considered involved a cylinder with an internal diameter of 151.3 mm, a bolt circle diameter of 198.5 mm, and an internal operating pressure of 8 bar. Eight conventional class 5.8 bolts were to be used. The two clamped members are made from aluminium (E = 68.9 GPa). To select an appropriate bolt size the fatigue strength for a class 5.8 bolt of 380 MPa was used as the fatigue limiting value. Equation (A-5) was used to find the stressed area of the bolt, and an appropriate bolt size larger than this stressed area was selected.

$$\sigma = \frac{F_e}{A_t} \tag{A-5}$$

In the stress equation, F_e is the external force and A_t is the stressed area of the bolt. The resultant stressed bolt area was calculated to be 17.7 mm^2. An M10 bolt with a stress area of 58.0 mm^2 was selected. To verify that bolt yielding would occur before the failure of the weld, the load on this size bolt was calculated to verify that its magnitude is lower than the load-carrying capacity of the weld bead. First, the member's stressed areas were calculated using Equation (A-6).

$$A_c \approx d^2 + 0.68dg + 0.065g^2 \tag{A-6}$$

Here A_c is the area of clamped members, d is the diameter of the bolt, and g is the grip length of the clamped members. The grip lengths for the slip-on and blind flanges were 10 and 15 mm, respectively. The stressed areas for the two members were calculated to be $A_{c-slip-on\,flange} = 1.745 \times 10^{-4}\ m^2$ and $A_{c\,blind\,flange} = 2.166 \times 10^{-4}\ m^2$. With the stressed areas evaluated, the stiffness k_c can be calculated. k_c is the resultant stiffness of the two members in series. Equation (A-7) was used to calculate each member's stiffness.

$$K_1 = \frac{AE}{g} \tag{A-7}$$

The calculated stiffness constant for the slip-on flange was 1.20 GN/m, and for the blind flange 0.995 GN/m. The bolt's stiffness constant was calculated to be 0.441 GN/m. Using Equation (A-8) the member's stiffness constant (k_c) was calculated to be 0.544 GN/m.

$$\frac{1}{k_c} = \frac{1}{k_1} + \frac{1}{k_2} \tag{A-8}$$

The stiffness ratio k_c/k_b of 1.23 was calculated with the bolt and member's stiffness. Using the member's and bolt stiffness the force acting on each bolt was calculated using Equation (A-9).

$$\Delta F_b = \frac{k_b}{k_b + k_c} F_e \tag{A-9}$$

The calculated bolt force, ΔF_b was 3023.34 N. The appropriate preload of the bolt and torque must be calculated to compare the two forces. A basic guideline in the Machinery's handbook is to use 75% of

the proof strength of the bolt material (Oberg, et al., 2012). The preload, F_i, and torque, T, were calculated using Equations (A-10) and(A-11). In equation (A-10), S_p is the proof strength.

$$F_i = 0.75 A_t S_p \tag{A-10}$$

$$T = 0.2 F_i d \tag{A-11}$$

A preload of 16530 N and a corresponding 33.06 Nm of torque were calculated. The clamping and bolt forces are equal to the preload force on initial tightening. The preload and external load effects were considered to validate that the bolts will yield before the weld fails. The bolt force was calculated with the effects of a preload using Equation (A-12).

$$F_b = F_i + \frac{k_b}{k_b + k_c} F_e \tag{A-12}$$

The new calculated bolt force with the preload effects was 19553.34 N. The force required to separate the members was calculated using Equation (A-13) to validate that the bolts yield before the weld bead fails. The calculated force is the external force that the bolts will carry.

$$F_c = F_i - \frac{k_c}{k_b + k_c} F_e \tag{A-13}$$

The force required to separate the clamped members was calculated to be 29930.24 N. This force corresponds to an internal pressure in the vessel of 133.2 bar. The bolts have a yield strength of 240 MPa. A force of 13920 N is required per bolt for the bolts to start yielding. Taking all 8 bolts into account, a force of 111360 N is required to yield the bolts. This load corresponds to an internal pressure of 61.9 bar. This pressure is less than the 75.74 bar internal vessel pressure required for the weld bead to fail. Therefore, the vessel's failure path is bolt-yielding, and a clamped member separation would occur at 133.2 bar.

Appendix B: Simulink® Model

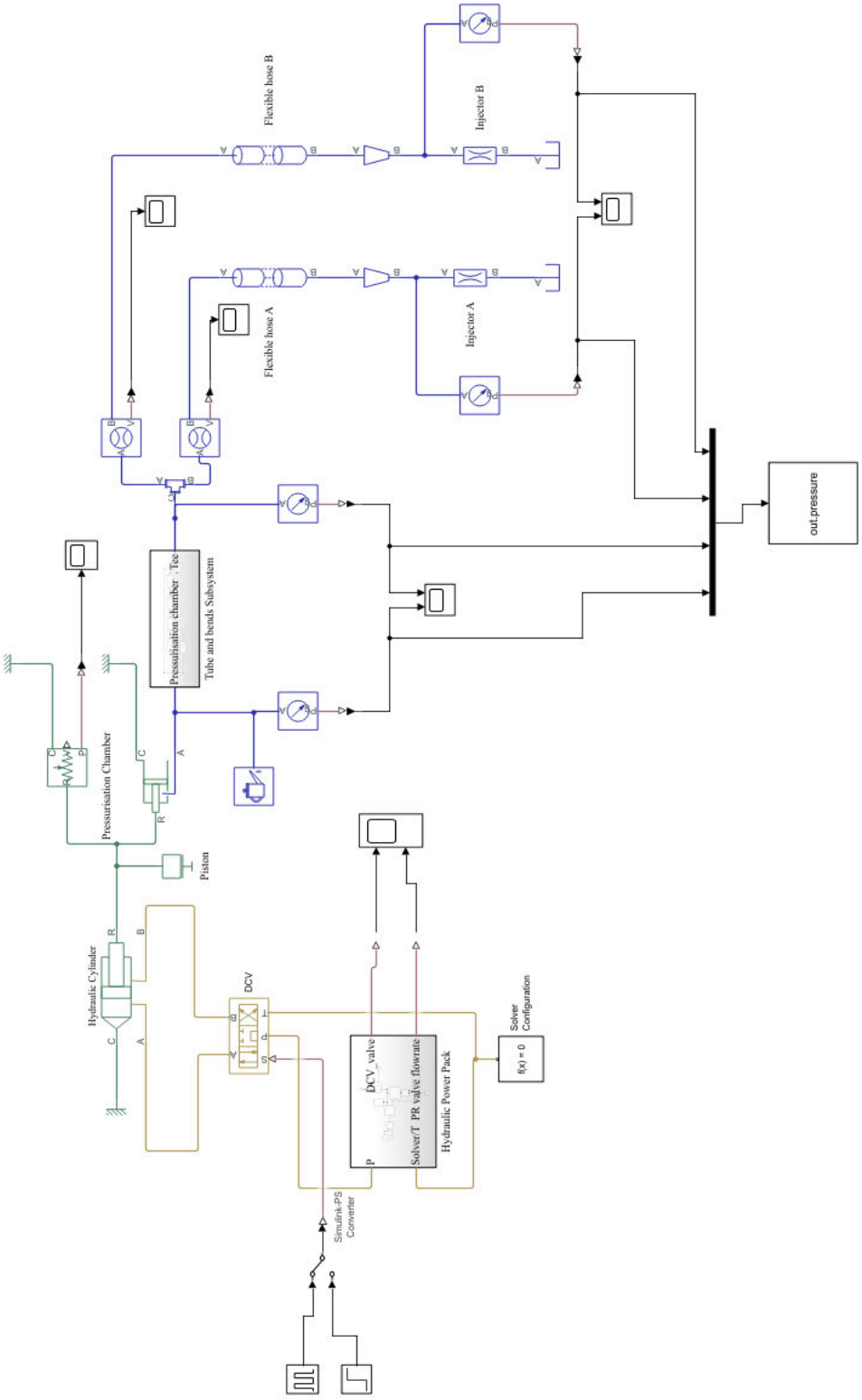

Figure B-1: MATLAB® Simulink® computational model.

Appendix C: MATLAB® Script


```
%Gel propellant test stand input variables
```

Input Parameters

```
P_R         = 35e05;        %Relief valve setting
sim_den     = 1000;         %Simulant density
D_o         = 1e-03;        %Orifice diameter
L_o         = 8.80e-03;     %Orifice Length
L_flex      = 60e-02;       %Length of flexible hose
L_pipe      = 2.4;          %Length of hardline SS pipe
G_ele       = 0.5;          % Elevation gain
m_p         = 1;            %piston mass
D_p         = 100e-03;      %piston diameter
L_c         = 0.7;          %Length of the pressurisatrion chamber
D_pipe      = 12.7e-03;     %SS Pipe diameter
D_hydr      = 50e-03;       %Hydraulic cylinder diameter
D_hydr_1    = 25e-03;
bend_radius = 38e-03;       %Pipe bender bend radius
```

Area Calculations

```
%Orifice Area
A_o         = (pi*D_o^2)/4;
%Piston Area
A_p         = (pi*D_p^2)/4;
%Pressurisation chamber dead volume
V_dead      = A_p*(1-L_c);
% SS pipe area
A_pipe      = (pi*D_pipe^2)/4;
%insert inlet
d_orifice_inlet = 5e-03;
A_orifice_inlet = (pi*d_orifice_inlet^2)/4;
%Hydraulic cylinder areas
A_hydr          = (pi*D_hydr^2)/4;
A_hydr_1        = (pi*D_hydr_1^2)/4;
```

Area change calculations

```
R               = A_o/A_orifice_inlet;    %Area ratio

%Loss coeficient for gradual contractions theta = 118 deg
K_contraction   = 0.29;
```

```
theta           = deg2rad(118);
%to calculate the contraction correction factor C_contraction
% K_contraction = C_contraction/2*sqrt(sin(theta/2))*(1-R)

C_contraction   = (K_contraction*2)/(sqrt(sin(theta/2)))*(1-R);
```

Plotting

```
%plotting data from simulation
t               = out.pressure.Time;        %simulation time
P_c             = out.pressure.Data(:,1);   %Pressurisation chamber pressure
P_1             = out.pressure.Data(:,2);   %Pressure after line losses
PT_01           = out.pressure.Data(:,3);   %Injection pressure Injector A
PT_02           = out.pressure.Data(:,4);   %Injection pressure Injector B

figure(1)
plot(t,P_c,'b','LineWidth',1.5)
title("Pressurisation chamber Pressure"), xlabel("time [s]"),ylabel("Pressure [bar]")
grid on
figure(2)
plot(t,PT_01,'r','LineWidth',1.5), title("Injection Pressure Injector A"),ylabel("pressure
[Pa]"),grid on, xlabel("time [s]")
figure(3)
plot(t,PT_02,'g','LineWidth',1.5), title("Injection pressure Injector B"),ylabel("Pressure
[Pa]")
xlabel("time [s]")
grid on
```

Appendix D: Rheological Characterisation Graphs

This section presents the shear rate versus viscosity curves of test samples described in Section 6.3.Graphs D-1 to D-6 show the Williamson model best fit line fitted to the experimental data.

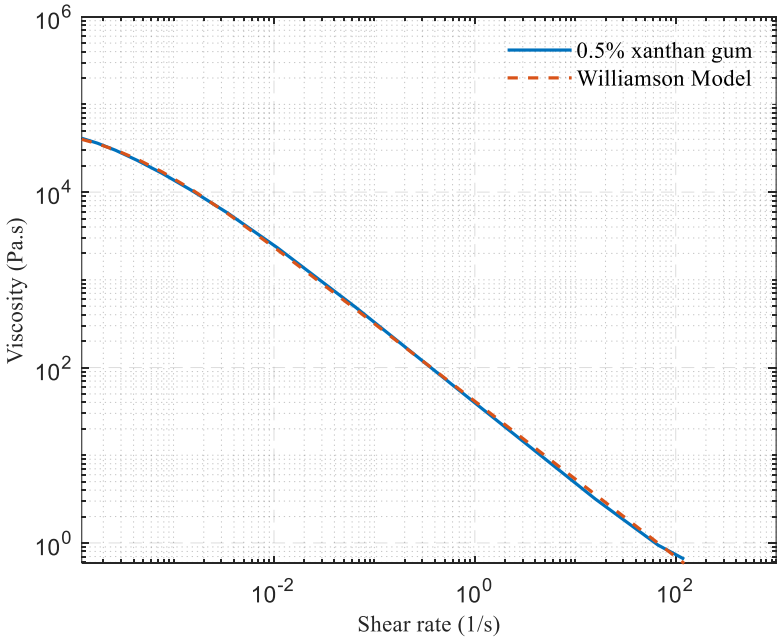

Figure D-1: Shear rate versus viscosity for x0.5 and Williamson best fit model.

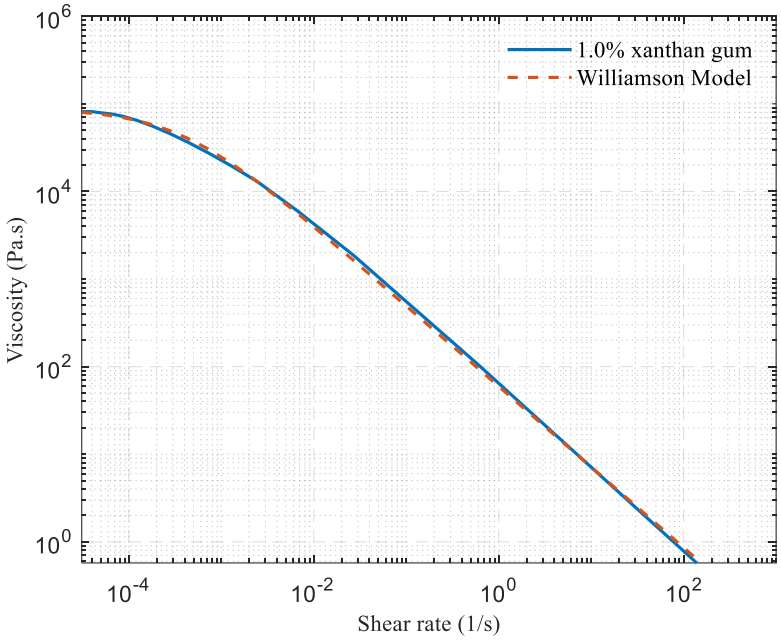

Figure D-2: Shear rate versus viscosity for x1.0 and Williamson best fit model.

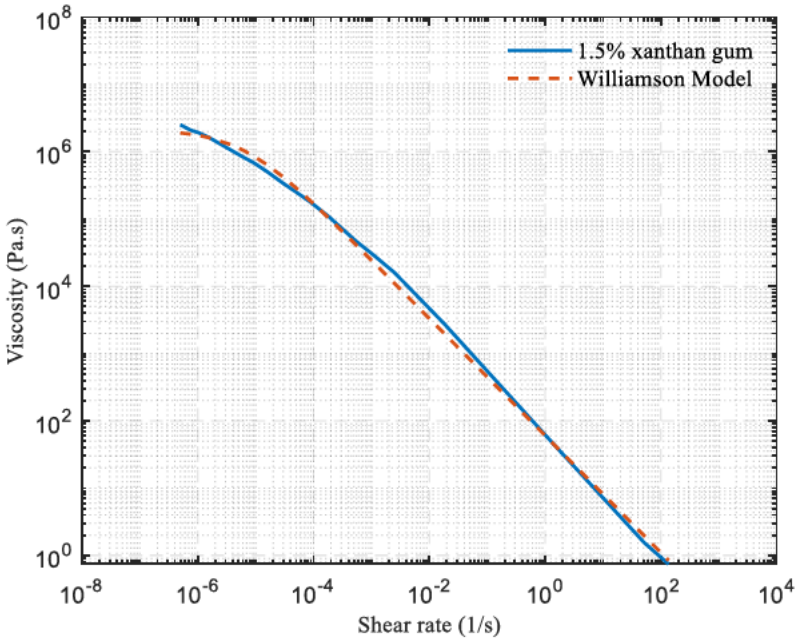

Figure D-3: Shear rate versus viscosity for x1.5 and Williamson best fit model.

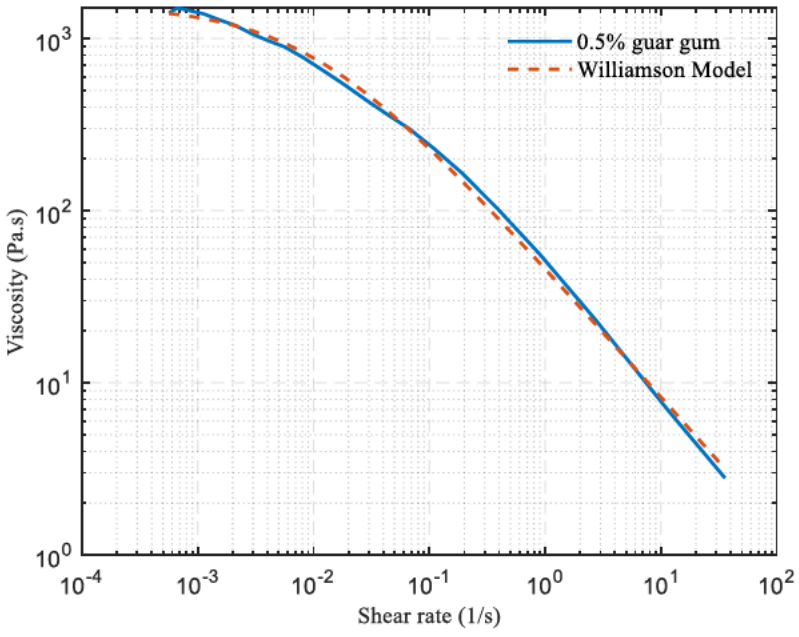

Figure D-4: Shear rate versus viscosity for g0.5 and Williamson best fit model.

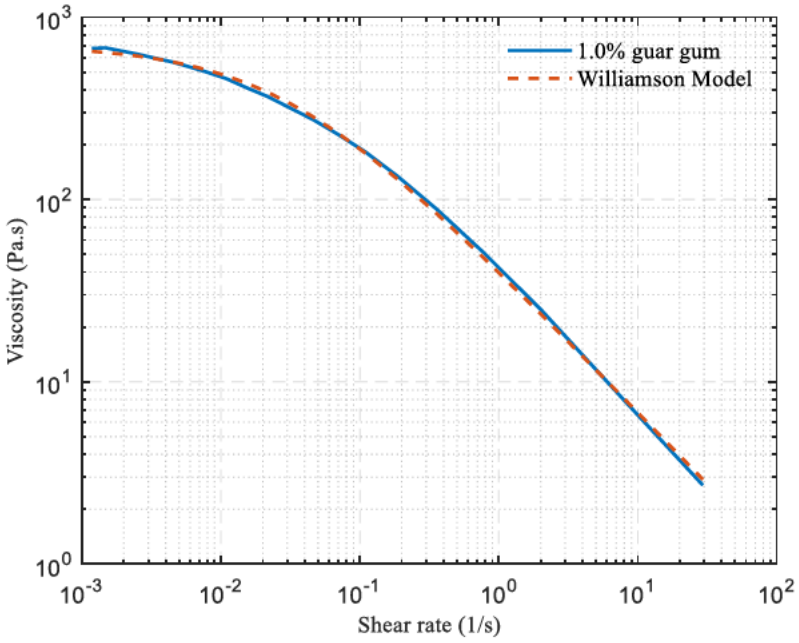

Figure D-5: Shear rate versus viscosity for g1.0 and Williamson best fit model.

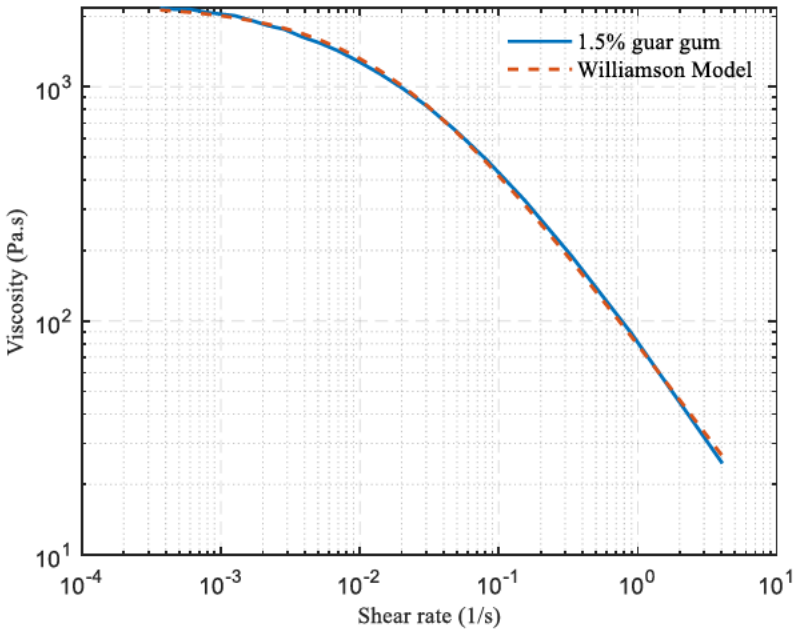

Figure D-6: Shear rate versus viscosity for g1.5 and Williamson best fit model.

Appendix E: Injection Pressure Results

This section provides the injection pressure versus time graphs of the tested simulants on the test rig. A total of 48 tests were conducted for two types of simulants with a 0.5% and 1.5% concentration of gelling agent. Each simulant was injected at three different pressures in the range of 1.4 to 14 bar. The tests were conducted at three different impinging angles (45º 60º and 90º). Graphs E-1 to E-9 show the injection of 0.5 wt% guar gum at 45º 60º and 90º impinging angles.

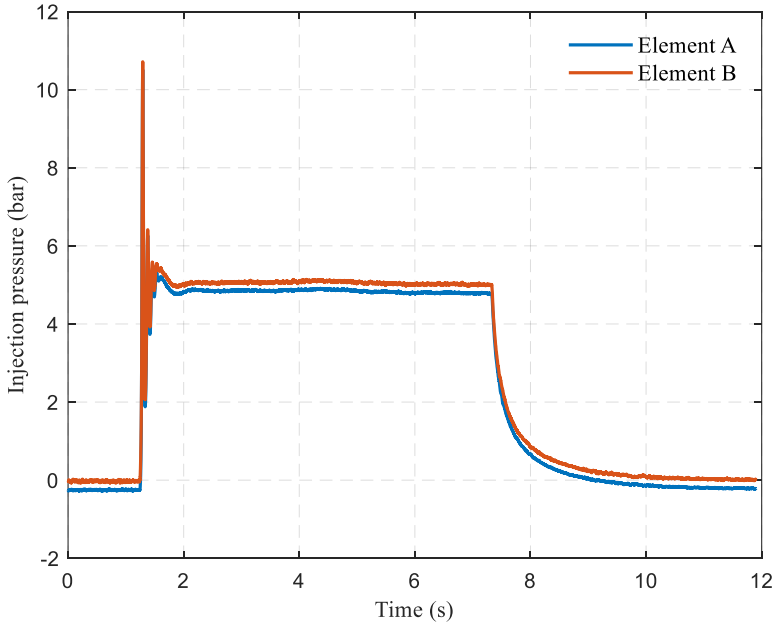

Figure E-1: Test 1 element A and B injection pressures of 0.5 wt% guar gum simulant injected at 45º.

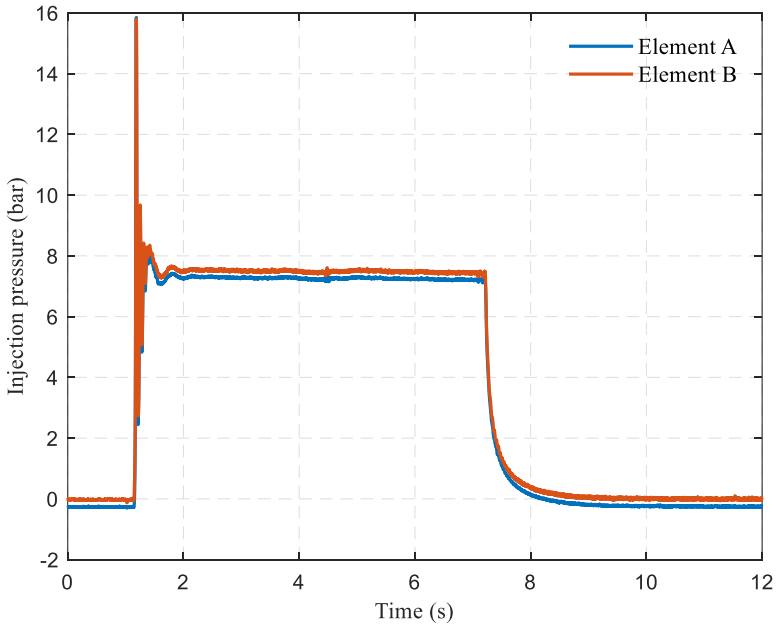

Figure E-2: Test 2 element A and B injection pressures of 0.5 wt% guar gum simulant injected at 45º.

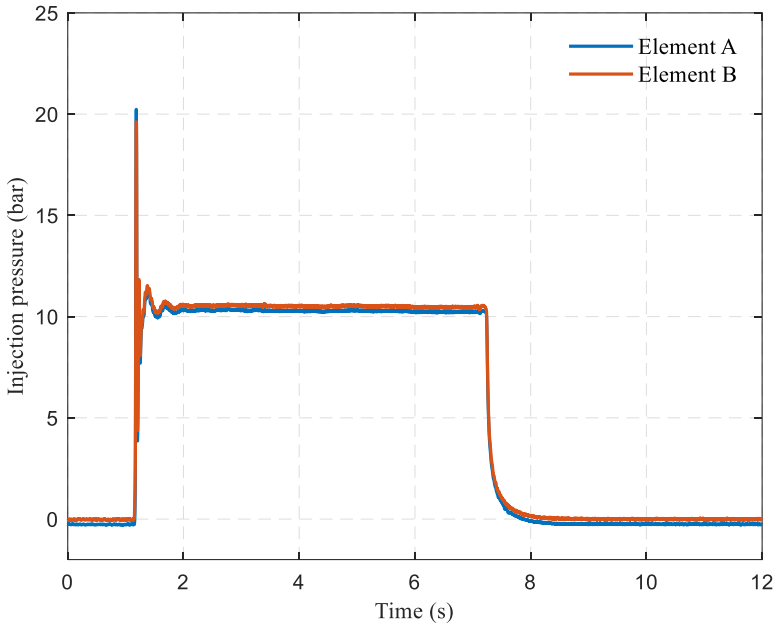

Figure E-3: Test 3 element A and B injection pressures of 0.5 wt% guar gum simulant injected at 45º.

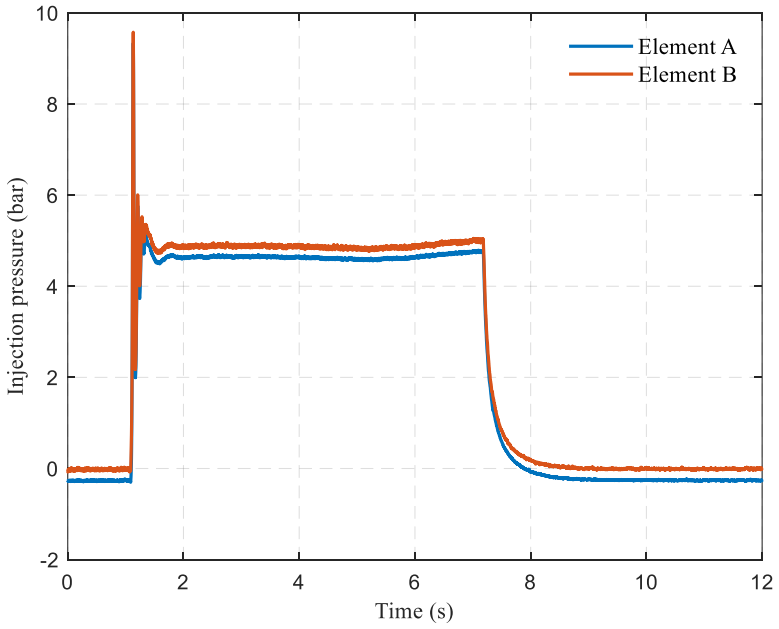

Figure E-4: Test 1 element A and B injection pressures of 0.5 wt% guar gum simulant injected at 60º.

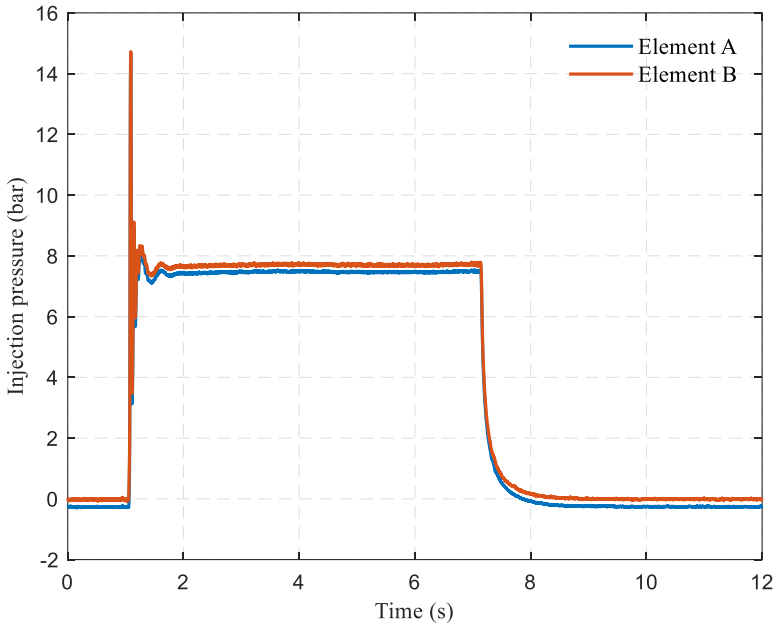

Figure E-5: Test 2 element A and B injection pressures of 0.5 wt% guar gum simulant injected at 60º.

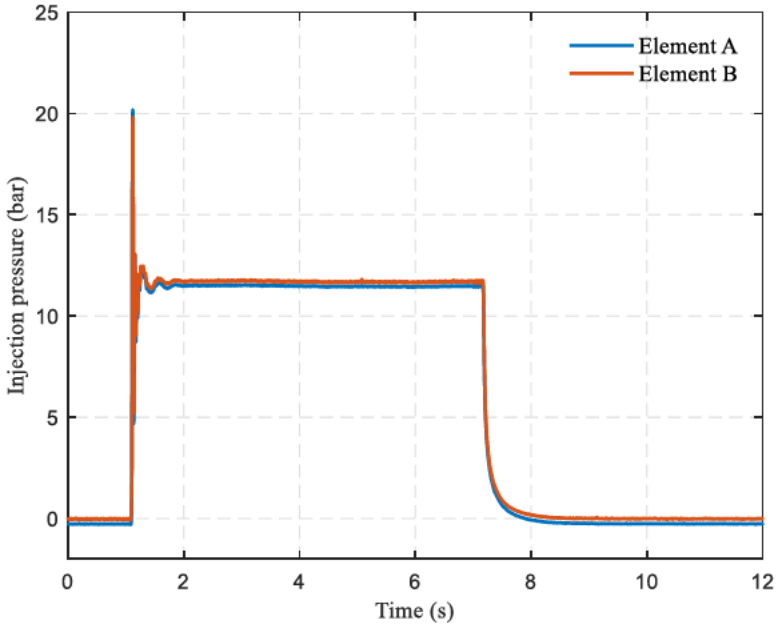

Figure E-6: Test 3 element A and B injection pressures of 0.5 wt% guar gum simulant injected at 60°.

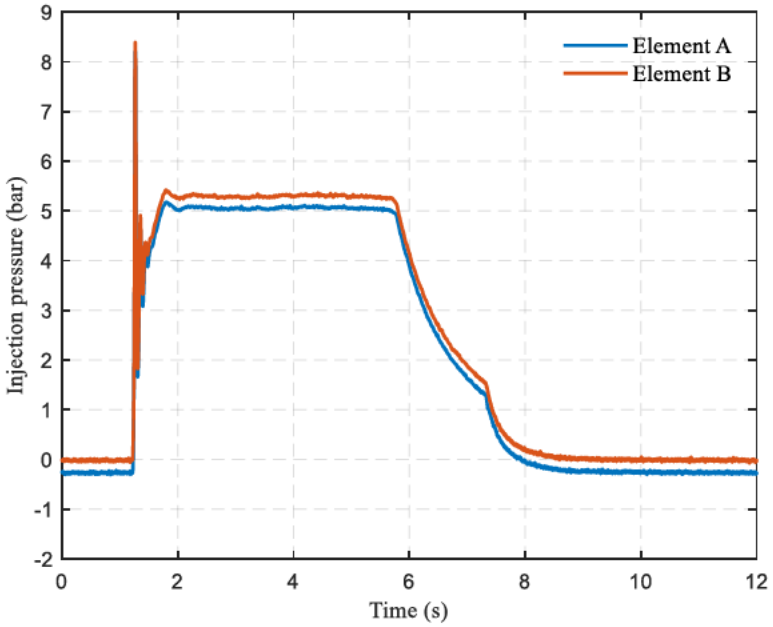

Figure E-7: Test 1 element A and B injection pressures of 0.5 wt% guar gum simulant injected at 90°.

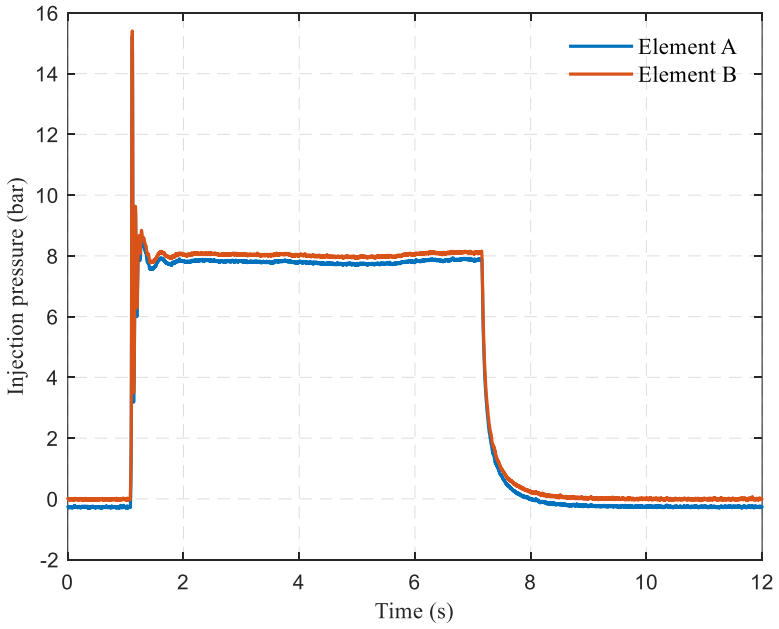

Figure E-8: Test 2 element A and B injection pressures of 0.5 wt% guar gum simulant injected at 90º.

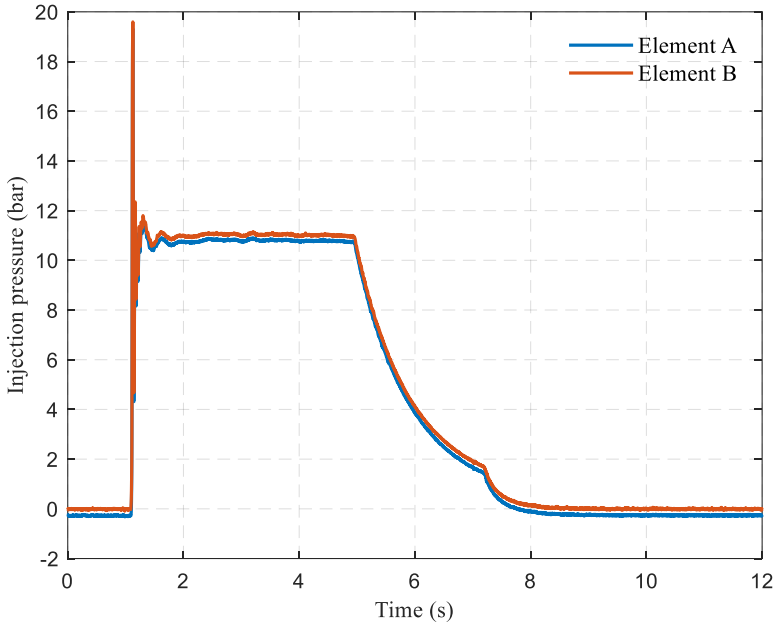

Figure E-9: Test 3 element A and B injection pressures of 0.5 wt% guar gum simulant injected at 90º.

Graphs E-10 to E-18 show the injection of 1.5 wt% guar gum at 45º 60º and 90º impinging angles.

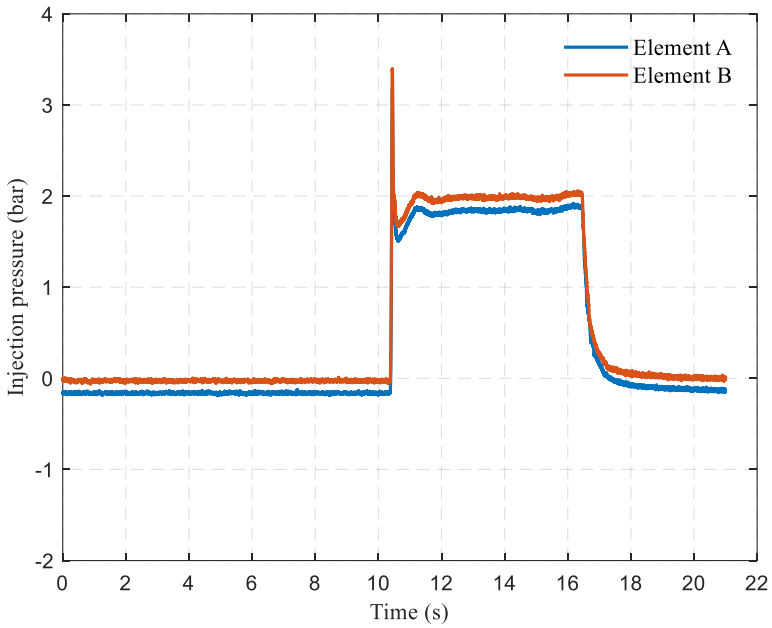

Figure E-10: Test 1 element A and B injection pressures of 1.5 wt% guar gum simulant injected at 45º.

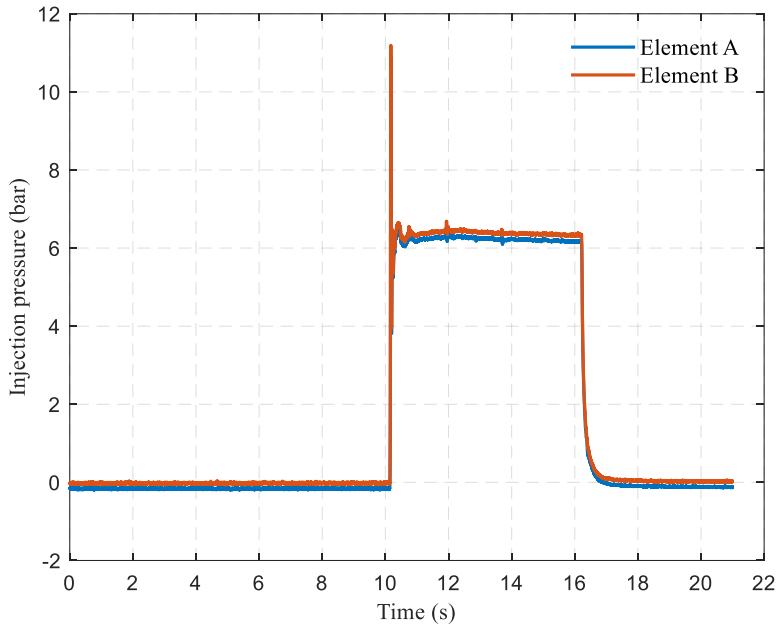

Figure E-11: Test 2 element A and B injection pressures of 1.5 wt% guar gum simulant injected at 45º.

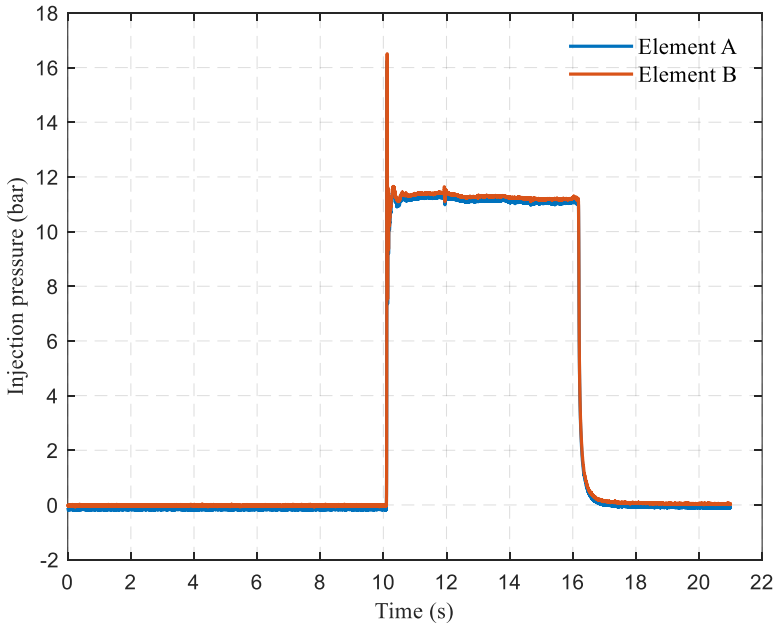

Figure E-12: Test 3 element A and B injection pressures of 1.5 wt% guar gum simulant injected at 45º.

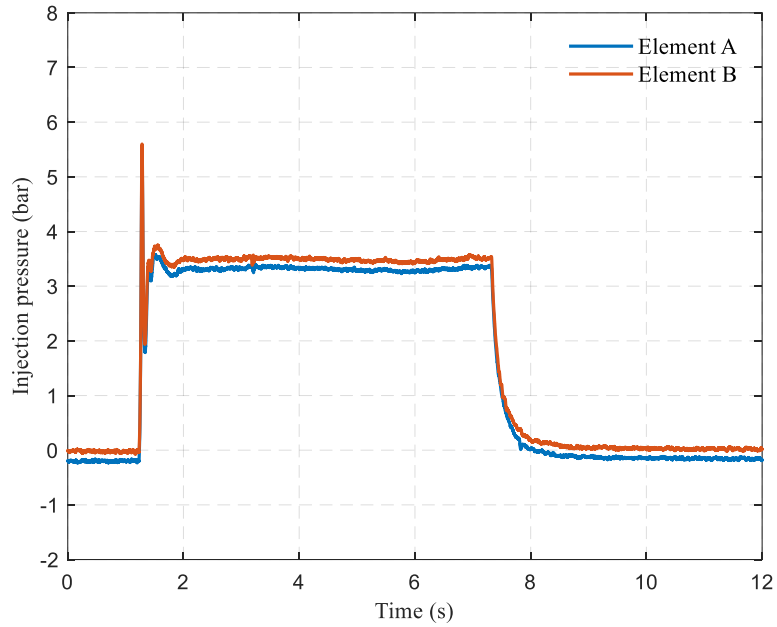

Figure E-13: Test 1 element A and B injection pressures of 1.5 wt% guar gum simulant injected at 60º.

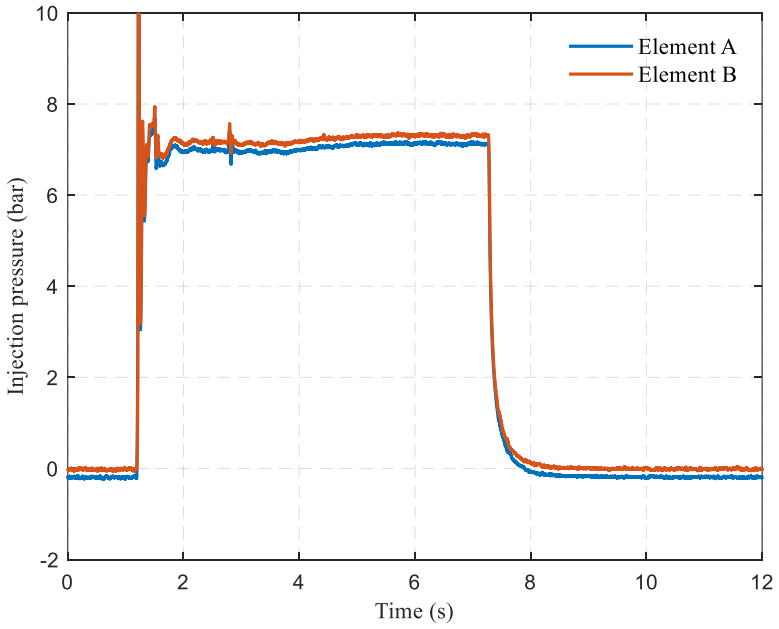

Figure E-14: Test 2 element A and B injection pressures of 1.5 wt% guar gum simulant injected at 60º.

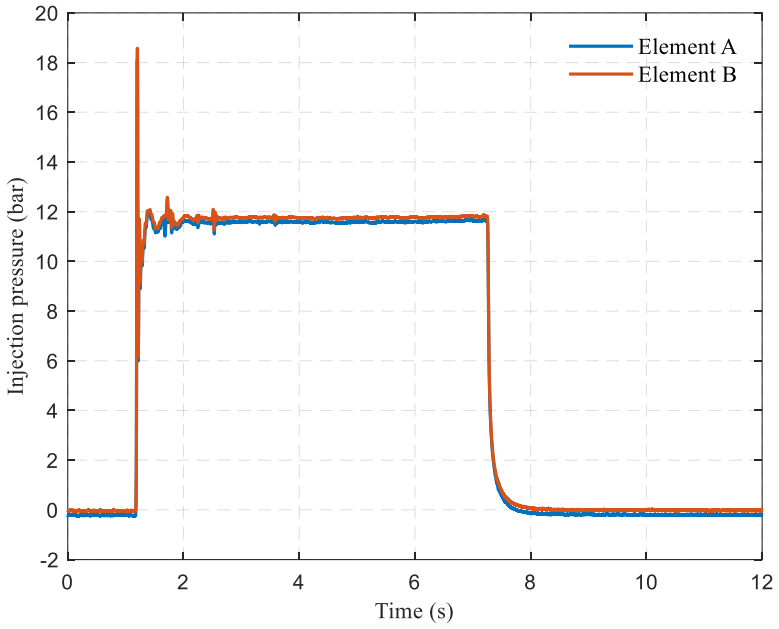

Figure E-15: Test 3 element A and B injection pressures of 1.5 wt% guar gum simulant injected at 60º.

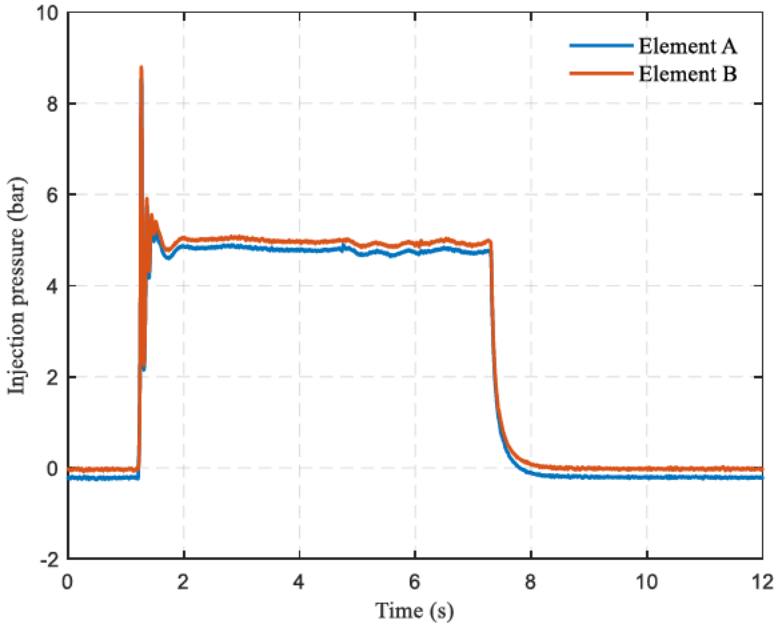

Figure E-16: Test 1 element A and B injection pressures of 1.5 wt% guar gum simulant injected at 90°.

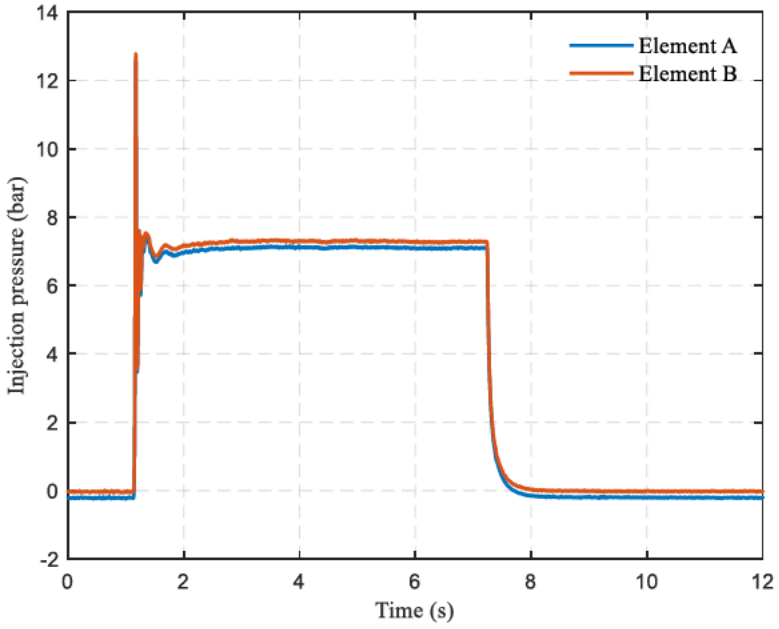

Figure E-17: Test 2 element A and B injection pressures of 1.5 wt% guar gum simulant injected at 90°.

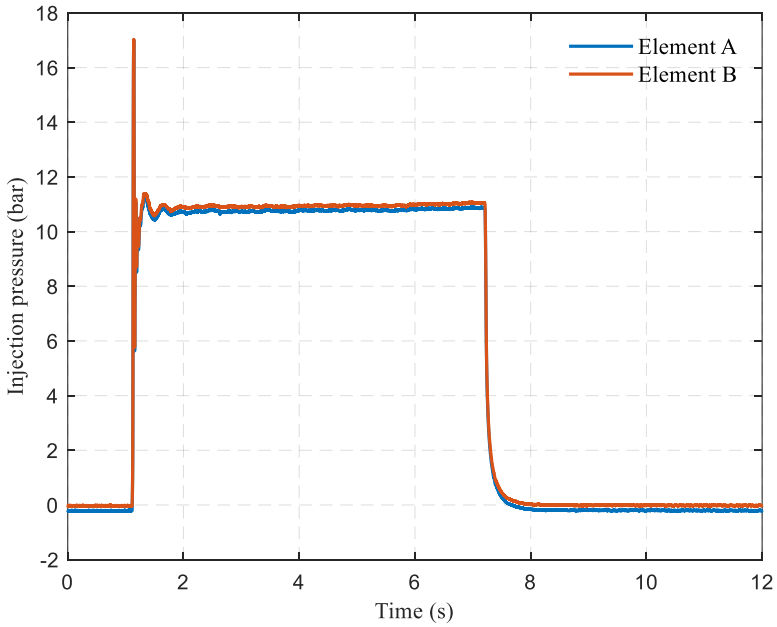

Figure E-18: Test 3 element A and B injection pressures of 1.5 wt% guar gum simulant injected at 90º.

Graphs E-19 to E-27 show the injection of 0.5 wt% Xanthan gum at 45º 60º and 90º impinging angles.

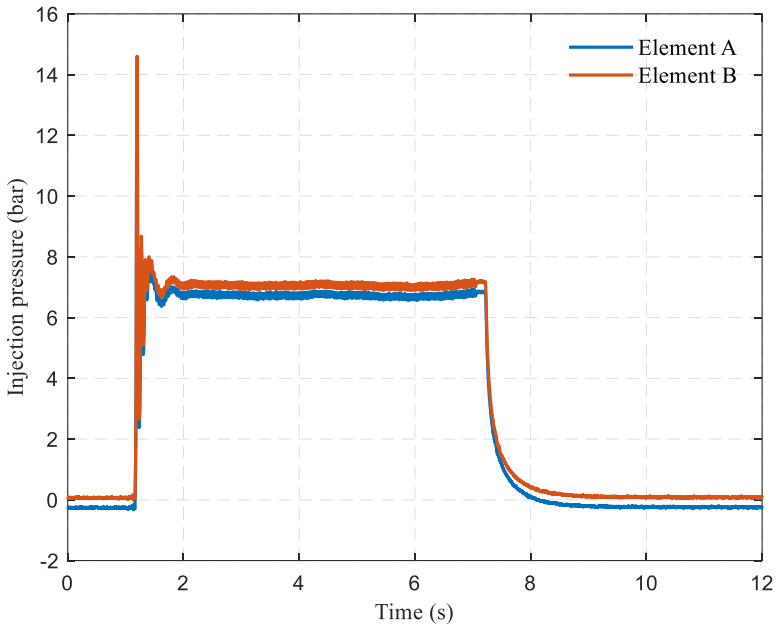

Figure E-19: Test 1 element A and B injection pressures of 0.5 wt% xanthan gum simulant injected at 45º.

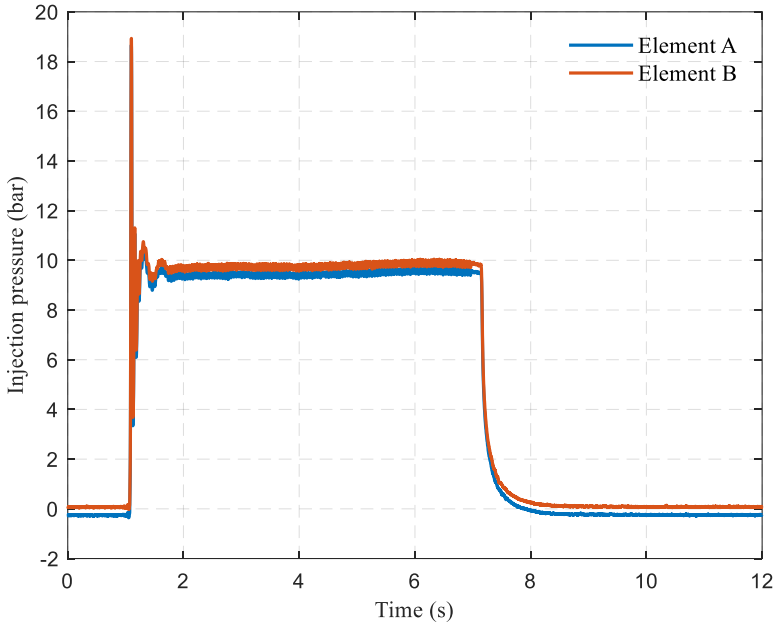

Figure E-20: Test 2 element A and B injection pressures of 0.5 wt% xanthan gum simulant injected at 45º.

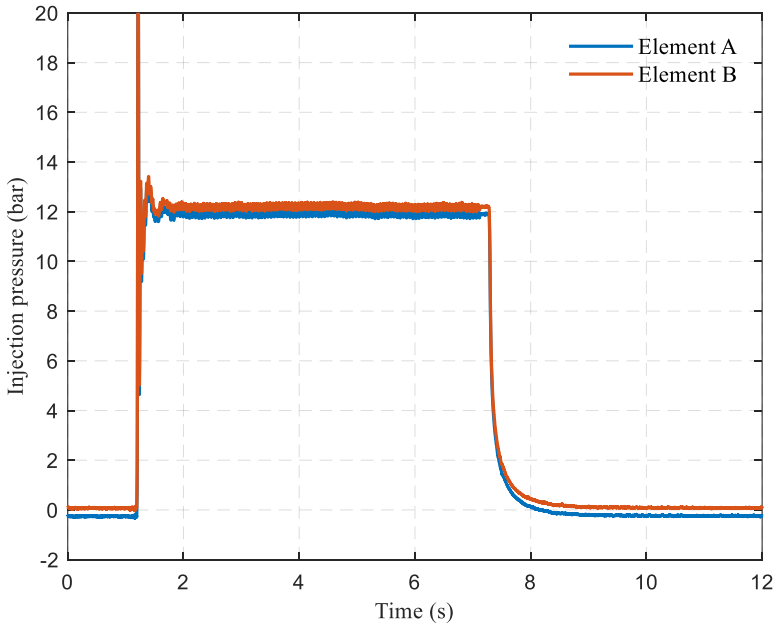

Figure E-21: Test 3 element A and B injection pressures of 0.5 wt% xanthan gum simulant injected at 45º.

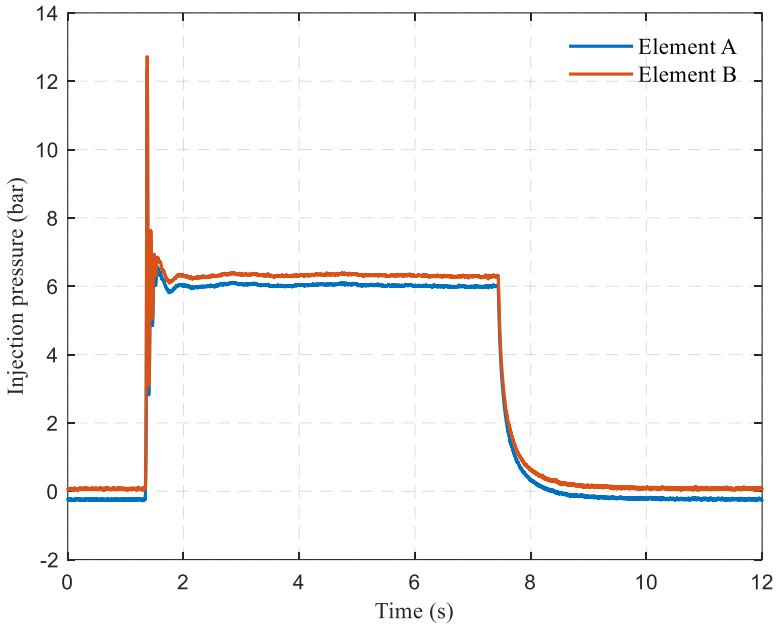

Figure E-22: Test 1 element A and B injection pressures of 0.5 wt% xanthan gum simulant injected at 60º.

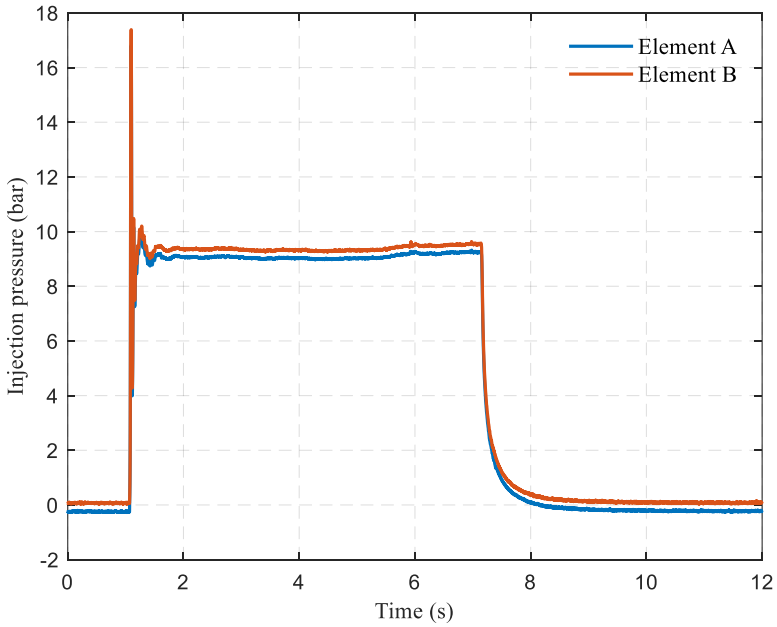

Figure E-23: Test 2 element A and B injection pressures of 0.5 wt% xanthan gum simulant injected at 60º.

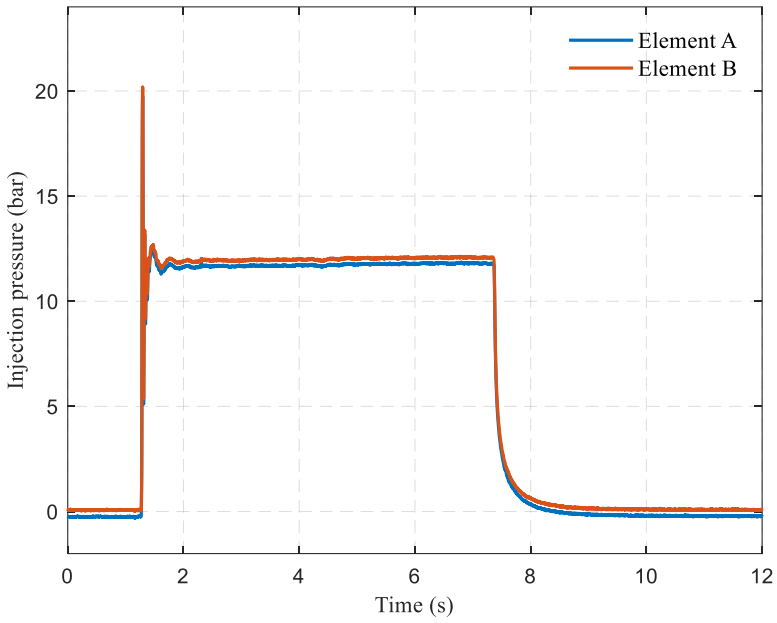

Figure E-24: Test 3 element A and B injection pressures of 0.5 wt% xanthan gum simulant injected at 60º.

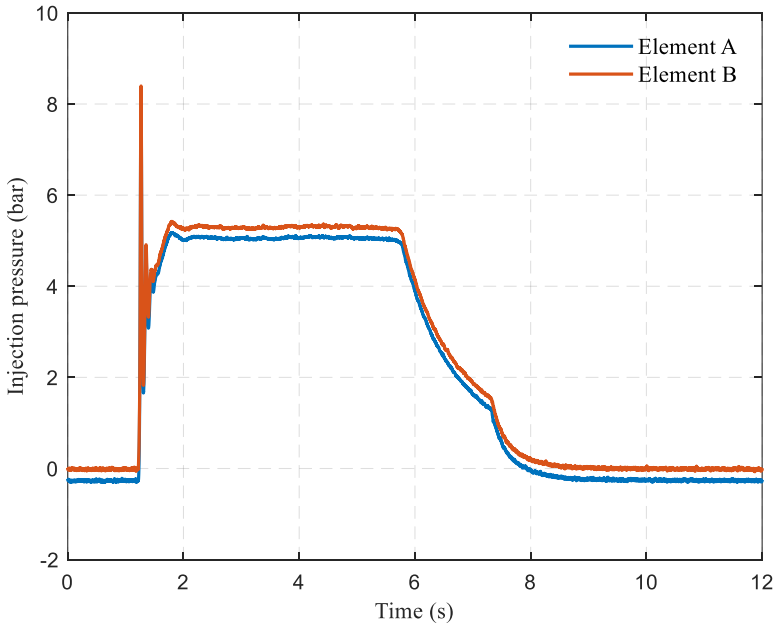

Figure E-25: Test 1 element A and B injection pressures of 0.5 wt% xanthan gum simulant injected at 90º.

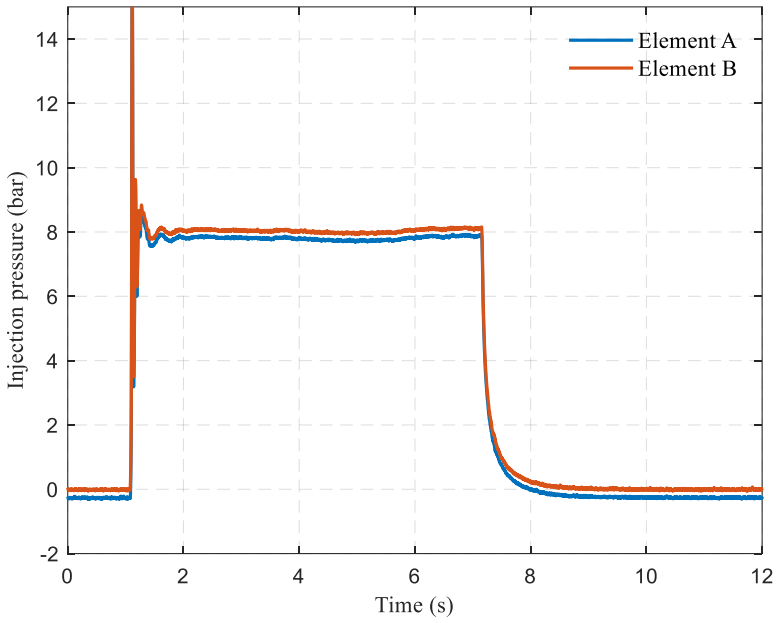

Figure E-26: Test 2 element A and B injection pressures of 0.5 wt% xanthan gum simulant injected at 90º.

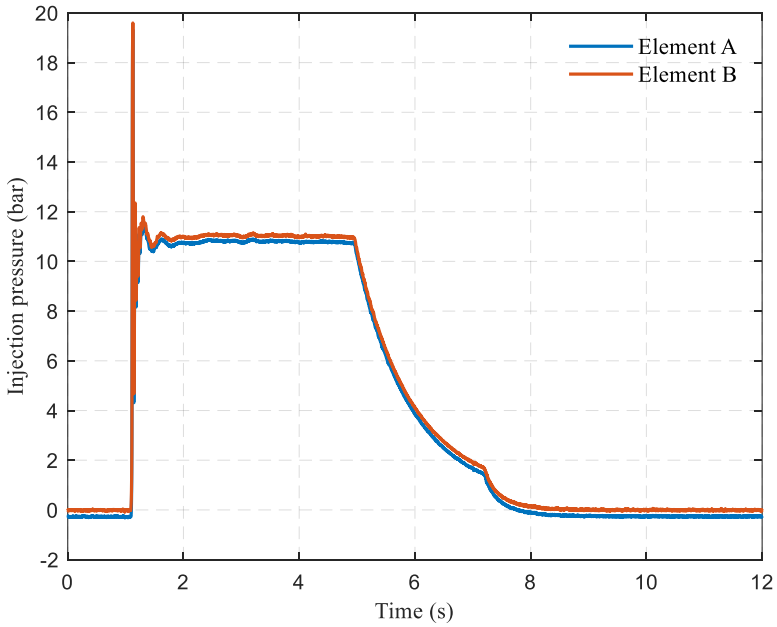

Figure E-27: Test 3 element A and B injection pressures of 0.5 wt% xanthan gum simulant injected at 90º.

Graphs E-28 to E-36 show the injection of 1.5 wt% Xanthan gum at 45º 60º and 90º impinging angles.

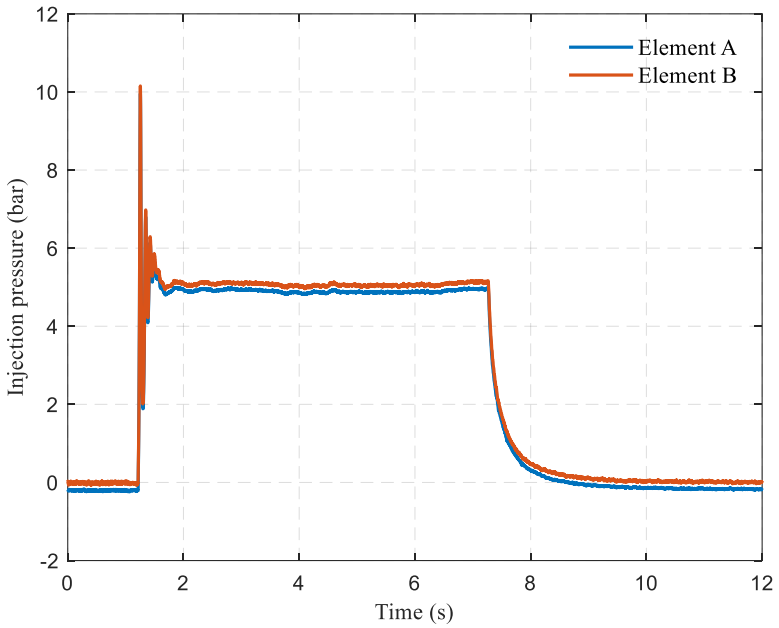

Figure E-28: Test 1 element A and B injection pressures of 1.5 wt% xanthan gum simulant injected at 45º.

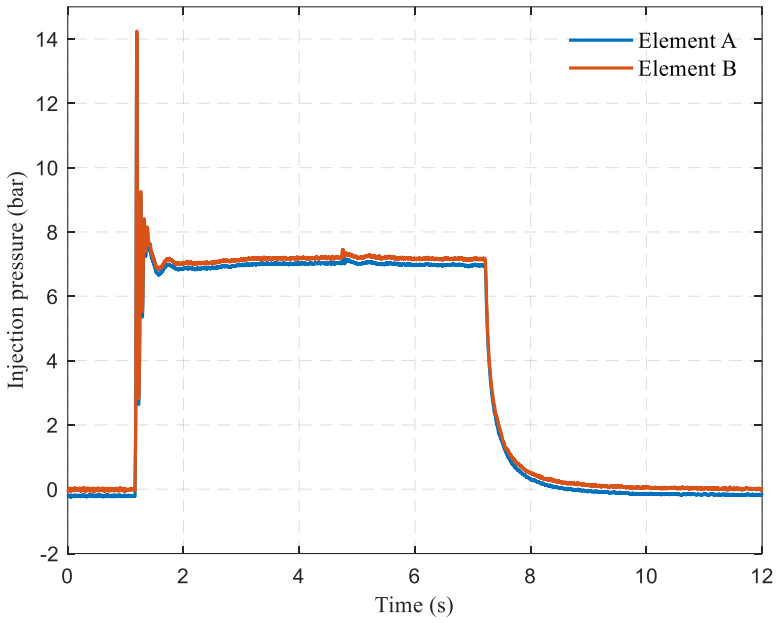

Figure E-29: Test 2 element A and B injection pressures of 1.5 wt% xanthan gum simulant injected at 45º.

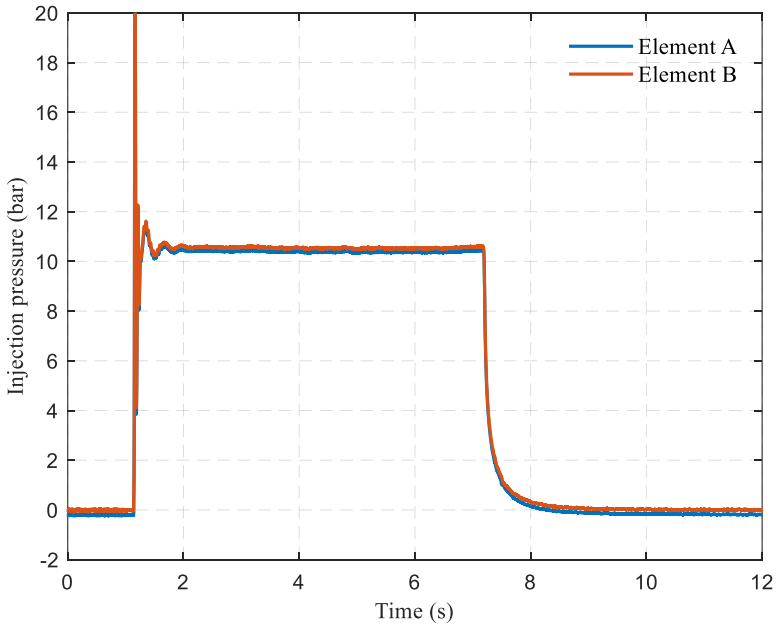

Figure E-30: Test 3 element A and B injection pressures of 1.5 wt% xanthan gum simulant injected at 45º.

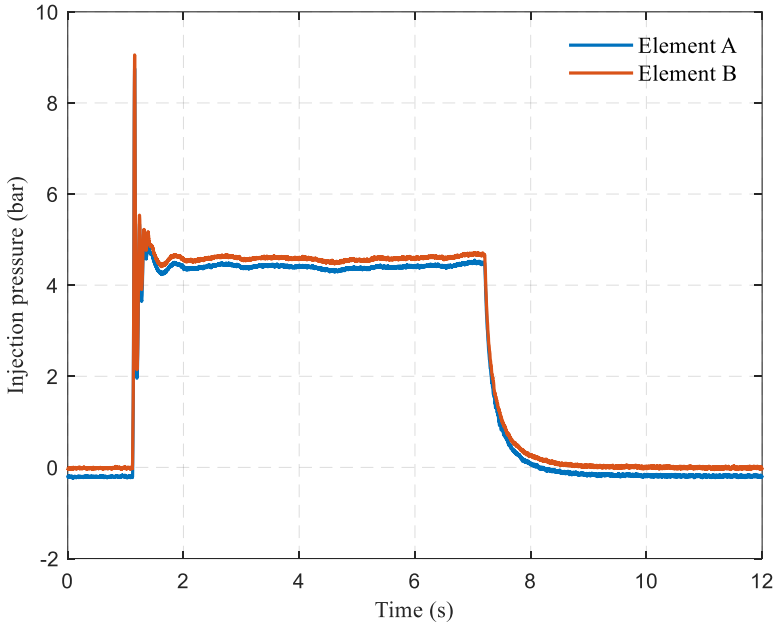

Figure E-31: Test 1 element A and B injection pressures of 1.5 wt% xanthan gum simulant injected at 60º.

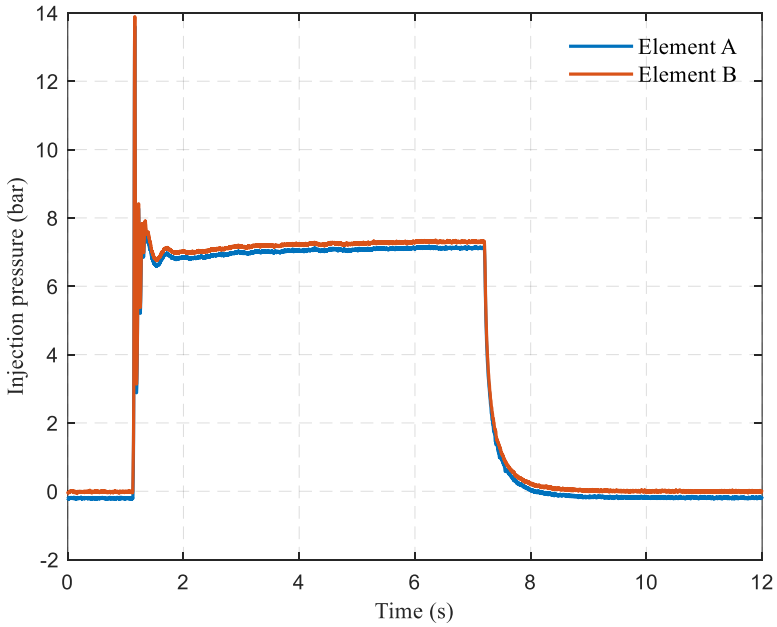

Figure E-32: Test 2 element A and B injection pressures of 1.5 wt% xanthan gum simulant injected at 60º.

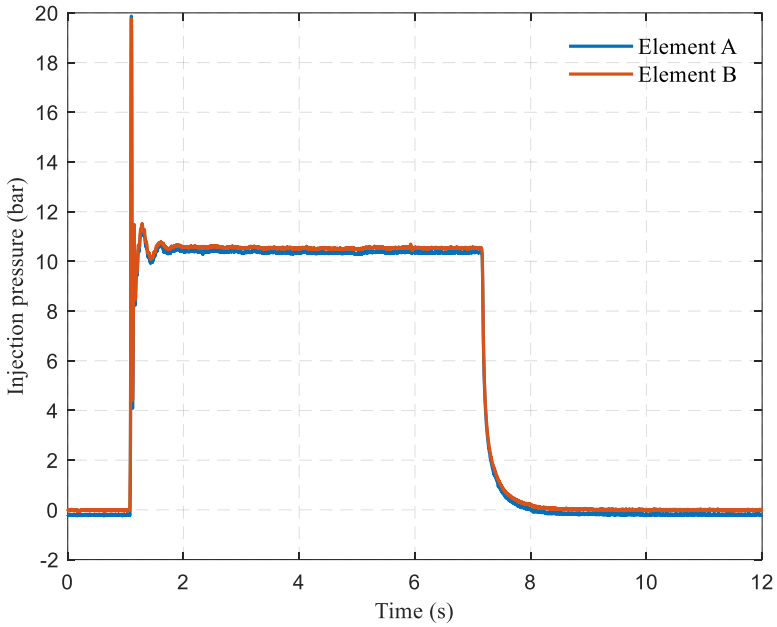

Figure E-33: Test 3 element A and B injection pressures of 1.5 wt% xanthan gum simulant injected at 60º.

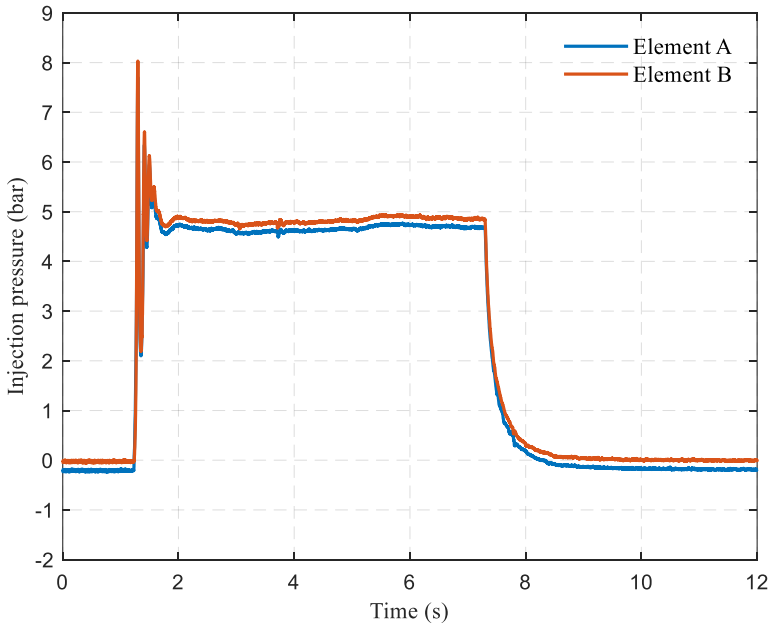

Figure E-34: Test 1 element A and B injection pressures of 1.5 wt% xanthan gum simulant injected at 90º.

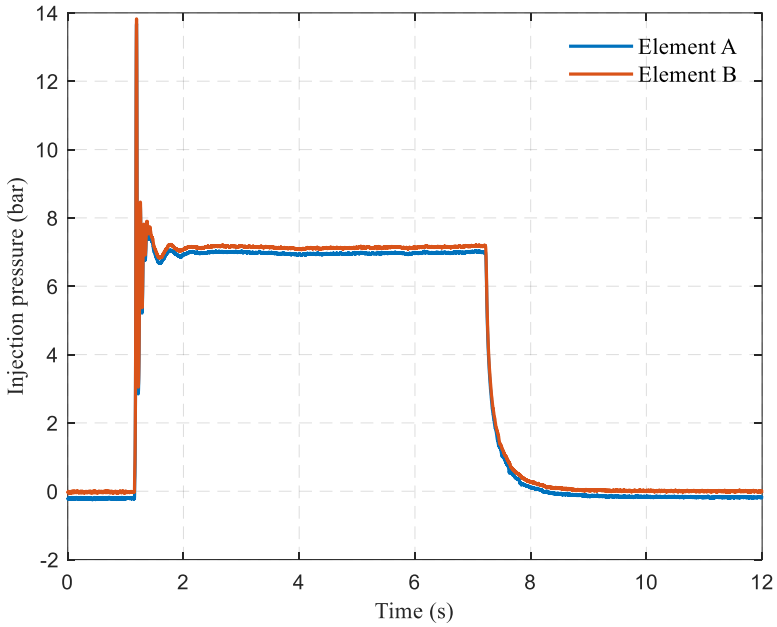

Figure E-35: Test 2 element A and B injection pressures of 1.5 wt% xanthan gum simulant injected at 90º.

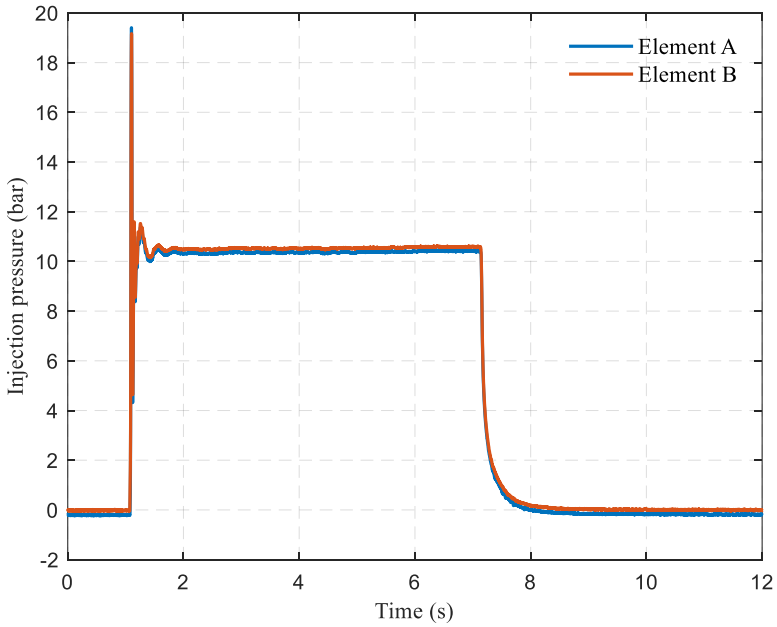

Figure E-36: Test 3 element A and B injection pressures of 1.5 wt% xanthan gum simulant injected at 90º.